Solid-State Joining of Molybdenum Based Materials via Pressure Resistance Welding

A Thesis
Presented in Partial Fulfillment of the Requirement for the
Degree of Master of Science
with a
Major in Material Science and Engineering
in the
College of Graduate Studies
University of Idaho
by
Sean M. Instasi

Major Professor: Indrajit Charit, Ph.D
Committee Members: Mark Roll, Ph.D.; Samrat Choudhury, Ph.D
Department Administrator: D. Eric Aston, Ph.D

May 2018

Authorization to Submit Thesis

This thesis of Sean M. Instasi, submitted for the degree of Master of Science with a major in Material Science and Engineering and titled “Solid-State Joining of Molybdenum Based Materials via Pressure Resistance Welding,” has been reviewed in final form. Permission, as indicated by the signatures and dates given below, is now granted to submit final copies to the College of Graduate Studies for approval.

Major Professor _____ Date _____
Indrajit Charit, Ph.D

Committee Members _____ Date _____
Samrat Choudhury, Ph.D

_____ Date _____
Mark Roll, Ph.D

Department Administrator _____ Date _____
D. Eric Aston, Ph.D

Abstract

Refractory metals and materials exhibiting high temperature stability have become more desired in various Generation-IV terrestrial nuclear reactors, space fission reactors, nuclear thermal propulsion reactors, and other high temperature industrial processes. For nuclear reactors, these materials must exhibit high temperature strength, excellent creep resistance, high temperature fatigue resistance, irradiation resistance, and coolant compatibility. Some of the potential high temperature materials include ferritic-martensitic (F/M) steel alloys, oxide dispersion strengthened (ODS) steels, and some refractory metals such as molybdenum and tungsten.

The use of refractory metals in various structural applications can often be limited by their poor weldability characteristics when traditional fusion welding methods are employed. The current research has been focused on exploring pressure resistance welding (PRW) for joining molybdenum-based materials. PRW is a solid-state joining technique (no melting) which combines uniaxial pressure and localized resistive heating to join specimens at their interface. Previous research on PRW has been effective in joining ODS alloys (MA 957, MA 956, and MA 754), F/M alloy HT9, and tungsten. Three molybdenum alloys, including pure molybdenum, TZM (precipitation strengthened by TiC and ZrC), and Mo-La (dispersed with lanthanum oxide particles), were examined in this work. The main objective of this research was to optimize the PRW technique applied to Mo-based materials by varying welding parameters (applied pressure, current, and time) and study the weld microstructure and mechanical properties.

Upon PRW, optical microscopy, Vickers microhardness, transmission electron microscopy, and scanning electron microscopy were used to characterize the quality of welds. Pure molybdenum welds exhibited dynamic recrystallization and grain growth throughout the weld zone. TZM welds exhibited dynamic recrystallization but did not have any significant grain growth. Mo-La welds exhibited limited dynamic recrystallization and grain growth and showed the best hardness profile throughout the weld. Both pure molybdenum and TZM welds showed decreases in hardness throughout the weld zones compared to the base materials, whereas Mo-La showed a slight increase in hardness throughout the weld zone. Overall, PRW appears to be an effective solid-state welding technique for joining molybdenum based materials although further studies will be needed to fully assess the promise of PRW as an enabling technology for key applications.

Acknowledgments

I would like to give my first acknowledgment to my academic advisor and major professor Dr. Indrajit Charit, I am extremely grateful for his guidance and encouragement throughout my time at the University of Idaho. I would also like to thank my committee members, Dr. Mark Roll and Dr. Samrat Choudhury, for their insight and dedication for teaching specialized topics in the field of material science and engineering.

I would also like to acknowledge my colleague, Nathan Jerred (Center for Advance Energy Studies, CAES) down in Idaho Falls, Idaho for his expertise and help with the pressure resistance welder (PRW) and other characterization techniques, without him, I would not have been able to do this research within the timeframe in which I did.

I would like to thank Dr. Gary A. Rozak from H.C. Starck Inc. for his contribution and for donating the molybdenum alloys which allowed for this research to happen as well as his expertise with molybdenum.

I would also like to thank Dr. Tom Williams, Arnab Kundu, Anumat Sittiho, and Martin Taylor, for their aid and help with learning how to use scanning electron microscope (SEM), transmission electron microscope (TEM), electron back scattering diffraction (EBSD), and various laboratory equipment.

Additionally, I would like to thank Charles Cornwall for his machining expertise and for teaching me and aiding in the machining of the molybdenum samples. I would like to extend that thank you to the Department of Chemical and Materials Engineering for having the machine shop and for helping me in every step of the way throughout my time as an undergraduate and as a graduate student.

Dedication

I want to dedicate this thesis to my wife Heather and my family for their support and encouragement throughout my education. I know that without their support, I would not be here today. Thank you!

Table of Contents

List of Figures

List of Tables

1.0 Background and Literature Review

1.1 Introduction

In the age of alternative and renewable energy, the desire to move away from fossil fuels has become abundantly clear. While renewable energy sources such as solar, wind, hydro, geothermal, etc. have become cheaper over the years and provide excellent greenhouse gas emission free energy, they can be intermittent. [1] In just the United States, different regions show predominantly favorable energy sources from wind, solar, hydro, etc. however, not every day is a sunny day or a windy day. Hydroelectric power has peak season and low seasons due to variability of rainfall throughout the year. [1] With climate change, a sustainable year-round energy (baseload electricity) source, will be needed and nuclear energy can potentially be the solution.

While nuclear energy has had issues, some notable nuclear meltdowns occurred at Three Mile Island (1979), Chernobyl (1986), and Fukushima (2011), which has increased fear of using nuclear energy as a viable energy source. These incidents happened because of a number of reasons including clear engineering flaws of the reactor systems and human error in operation, there is still tremendous upside to using nuclear energy. [2, 3, 5] Nuclear energy still provides a reliable energy source without the concern of outages or greenhouse gas emissions. There is still a push to improve future nuclear reactor performance with design and development of Generation-IV reactors, these reactor designs aim to promote safety, reliability, efficiency, sustainability, and nuclear non-proliferation. [4]

As these reactors will work at a higher temperature under extreme radiation exposure and corrosive environments, reactor designs would need more reliable materials with well-known irradiation effect behaviors, high strength and toughness, good corrosion resistance, and good fabricability (i.e. machinability and weldability), at an economically favorable price. [4, 5]

1.2 Objectives

Given the significance of weldability for molybdenum based materials in high demanding applications such as described above, this thesis research was focused on exploring feasibility

of using a solid-state welding technique known as pressure resistance welding for joining molybdenum based materials. The main objectives of this study are as following:

(a) To characterize microstructure and mechanical behavior of pressure resistance welds to understand the operative joining mechanism(s).

(b) To develop a set of operating parameters for joining molybdenum-based materials of three molybdenum based materials (commercially pure molybdenum, a precipitation-strengthened alloy TZM and a dispersion-strengthened alloy Mo-La) via pressure resistance welding (PRW).

This study may have major benefits in nuclear applications such as terrestrial fission reactors, space fission reactors, and other high temperature applications.

1.3 Limitations of Current Reactor Materials

Most of the current nuclear reactors in the United States of America (USA) are Generation-II reactors and are light water reactors (LWRs), e.g. boiling water reactor (BWR) or pressurized water reactor (PWR). These reactors have been around for decades and very few nuclear power plants have been built in the recent decade. Most of the Generation-II reactors were built prior to the 1990s and were designed to have a 40-year lifespan. In these LWRs, the cladding material used to house the nuclear fuel is mainly Zircaloys (either Zircaloy-2 or Zircaloy-4). [5] These zirconium based alloys have a melting temperature of around 1855 °C, have a low thermal neutron absorption characteristic, good corrosion resistance against water, and have good stability at the operating temperature. [6] However, zirconium does have an operating maximum of 800 °C due to a phase transformation; furthermore, it begins to oxidize at higher temperatures, and will produce hydrides due to poor hydrogen embrittlement behavior and/or release hydrogen by reducing steam. [5,6]

Generation-IV reactors will need different materials to handle the various coolant types and operating temperatures. These six designs are: [7]

1. Very high-temperature gas-cooled reactor (VHTR)
2. Gas-cooled fast reactor (GFR)
3. Sodium-cooled fast reactor (SFR)
4. Lead-cooled fast reactor (LFR)

5. Molten salt reactor (MSR)
6. Super-critical water-cooled reactor (SCWR)

Table 1.1: Potential of each system to meet the different Generation-IV goals.[a] [7]

Generation-IV goal	VHTR	GFR	SFR	LFR	SCWR	MSR
Efficient electricity generation	Very high	High	High	High	High	High
Flexibility: availability of high-temperature process heat	Very high	High	Low	Low	Low	Low
Sustainability: creation of fissile material	Medium/low	High	High	High	Low	Med/low
Sustainability: transmutation of waste	Medium	Very high	Very high	Very high	Low	High
Potential for 'passive' safety	High	Very low	Medium/low	Medium	Very low	Medium
Current technical feasibility	High	Medium/low	High	Medium	Medium/low	Low

[a] In the opinion of the authors; not necessarily the view of the GIF

The different reactors, as listed in Table 1.1, shows potential to meet the goals of Generation-IV reactors. All the reactor designs have high/very high efficient electricity generation, while almost all the other goals vary. These differences show the tradeoffs between different designs and whether higher safety is more important than minimal nuclear waste. Each reactor design for Generation-IV reactors will need different materials due to higher operating temperatures and coolant type, as shown in Table 1.2. New materials need to be further studied to qualify them for use in these reactors.

Table 1.2: Different Gen-IV nuclear reactor systems. [8]

Reactor system	Coolant	Neutron spectrum	Core outlet temperature (°C)
Gas-cooled fast reactor (GFR)	Gas (e.g. He)	Fast	~850
Lead-cooled reactor (LFR)	Liquid metal (e.g. Pb, Pb-Bi)	Fast	550-800
Molten salt reactor (MSR)	Molten salt (fluoride salts)	Thermal	700-800
Sodium-cooled fast reactor (SFR)	Liquid metal (Na)	Fast	~550
Very high temperature reactor (VHTR)	Gas (e.g. He)	Thermal	>900
Super critical water-cooled reactor (SCWR)	Water	Thermal/fast	350-620

1.4 Potential Generation-IV Cladding Materials

For most Generation-IV reactor designs, new materials will need to replace zirconium based alloys as the cladding material. The important physical properties include corrosion resistance to coolant, low neutron absorption, operation temperature compatibility, thermal conduction, irradiation stability, and great mechanical strength properties. This limits the choices of cladding materials in these reactors to the following groups of materials: [9]

- Ferritic/Martensitic steels (F/M steels)

- Austenitic stainless steels
- Oxide dispersion strengthened (ODS) steels
- Nickel based alloys
- Refractory metals

1.4.1 Ferritic/Martensitic Steels

F/M steels have chromium compositions of 9-12 wt% and are designed to have a balance between ferritic and austenitic stabilizing alloying elements (Si, Cr, Mo, Al, Ti, Nb for ferrite, and C, N, Mn, Ni, Cu for austenite). These alloying elements are added to produce 100% austenite upon austenitization, and 100% martensite upon quenching or normalizing following austenitization. Tempering the martensitic steel transforms most of it into ferrite resulting in tempered martensite structure. Tempered martensite has much better corrosion resistant properties than 100% martensite. [10] The main advantage of some F/M steels is the reduced-activation property for less irradiation induced activity. Additionally, F/M steels have good void swelling resistance and good creep resistance (below 500 ^{o}C). Irradiation embrittlement occur at or less than 400 °C. Some F/M steels which are being considered are HT-9, T-91, NF12, etc. [10]

1.4.2 Austenitic Stainless Steels

Austenitic stainless steels show excellent corrosion/oxidation resistance as well as good creep resistance at higher temperatures (up to 600 ^{o}C), because of alloying with chromium and molybdenum respectively. [10] However, void swelling at moderate neutron doses becomes a major performance-limiting issue. The void swelling in austenitic stainless steel is much higher than F/M steels. [10] Additionally, another limiting factor for austenitic stainless steels are their low thermal conductivity which would affect the efficiency of heat transfer from reactor core to the coolant medium used to generate electricity. Another limiting factor with austenitic stainless steels is the radiation-assisted depletion of chromium, the depletion of Cr and increase in Ni, resulting in increased corrosion. [62] The segregation occurs from the grain boundaries, which leads to susceptibility of corrosion in water or lead based cooling systems. Examples of austenitic steels used are variants of 316 stainless steel. [10]

1.4.3 Oxide Dispersion Strengthened (ODS) Steels

The difference between ODS steels and other steels is the presence of nano-clustered oxide particles which hinder dislocation motion. [10] These nano-clustered oxides also act as sinks for radiation induced defects, which promotes 'healing' in the material. ODS steels are primarily made via a mechanical alloying (MA) process, which leads some steel alloys to have a 'MA' prefix name. These ODS steel alloys have good high temperature properties, radiation resistance from swelling and radiation embrittlement. [10] If ODS steels have titanium or tungsten present, this aids in promoting smaller nano clustered oxides as well as aiding in increased creep resistance at elevated temperatures. Some examples of these materials are 12YWT, MA956, Fe-9Cr-Y_2O_3. [10]

1.4.4 Nickel Based Alloys

Nickel based superalloys, Inconel 690, 625, and 718, are known for being used at elevated temperatures for such application in gas turbines, jet engines, etc. [10] These nickel based superalloys exhibit excellent creep resistance and excellent properties at higher temperatures. However, once irradiation occurs, nickel superalloys are known to experience radiation embrittlement, swelling, and phase instability, and prolonged irradiation-induced activity. [10] These radiation effects make nickel based superalloys less favorable as a cladding or structural material for advanced nuclear reactors. Alloy 617 and other solid solution strengthened alloys may be used in heat exchangers which is part of the VHTR system. [10]

1.4.5 Refractory Metals

Refractory metals have higher melting points and would be able to handle higher operating temperatures and to add a level of safety if a spike in temperature were to occur. The best refractory metal candidates are TZM (a molybdenum-based alloy), Mo-Re alloys, W-Re alloys, and Ta alloys. [10] Niobium based materials show a major lack of oxidation resistance which leads to embrittlement, which would prevent it from being a good nuclear material. Rhenium alloys would be too expensive to justify its cost as a cladding material; it would be alloyed with molybdenum to improve its weldability and machinability. [10] Some of the issues with these alloys are the higher cost associated with welding, machining, and fabrication, because of the higher ductile-to-brittle transition temperatures. Additionally, refractory metals need more

extensive research in the longevity and understanding mechanical properties during irradiation exposure at elevated temperatures. [10]

While these materials may be potential candidates, other materials need additional research or discovery. As shown in Table 1.3, the six Generation-IV reactors have a list of candidates cladding materials. It is shown that no material will work for every reactor design. That is why it is important to research every potential material and develop fundamental understanding of their behavior. If the limitation of a material is its inadequate weldability, improving welding techniques would lower the cost and improve quality of welds, the focus of this thesis.

Table 1.3: Main characteristics of Generation-IV nuclear fission reactor systems. [11]

Reactor type	Fuel	Coolant	Moderator	Neutron spectrum	Core outlet temperature (°C)	Dose (dpa)	Candidate cladding material
Super critical water-cooled reactor (SCWR)	UO_2 (thermal) MOX (fast)	Water	Water	Thermal or Fast	~ 550	10–40	Zr alloys Austenitic stainless steel F/M steels Ni–based superalloys ODS alloys
Sodium-cooled fast reactor (SFR)	UPuC/SiC U–Pu–Zr MOX	Liquid Na	–	Fast	~ 550	90–160	F/M steels ODS alloys
Lead-cooled reactor (LFR)	Nitrides, MOX	Liquid Pb alloys	–	Fast	550–800	50–130	Austenitic stainless steel F/M steels ODS alloys SiC Refractory alloys
Gas-cooled fast reactor (GFR)	(U, Pu)O_2 Carbide fuel (U, Pu)	He	–	Fast	~ 850	50–90	ODS alloys Refractory alloys SiC
Molten salt reactor (MSR)	Salt	Molten salt	Graphite	Thermal	700–800	100–180	No cladding
Very high temperature reactor (VHTR)	TRISO UOC	He	Graphite (thermal)	Thermal or Fast	1000	7–30	ZrC coating SiC coating

* TRISO: Tristructural isotropic fuel, a type of micro fuel particle consisting of a fuel kernel composed of uranium oxide (sometimes uranium carbide) in the centre, coated with four layers of three isotropic materials.

1.5 Molybdenum

1.5.1 Pure Molybdenum

Molybdenum is a refractory metal with a melting temperature of 2896 K (2623°C), a density of 10.22 g/cc (at room temperature), Young's modulus of 329 GPa, and a Vickers hardness of 1530 MPa. [63] Other refractory metals, metals with melting points are greater than 2000 °C, include niobium (Nb), tantalum (Ta), tungsten (W), and rhenium (Re). When compared to these refractory metals, molybdenum exhibits excellent strength and higher temperature creep

resistance with about half the density of tungsten. [12] However, an issue with molybdenum is oxidation above 650 °C to produce MoO_3, a volatile gas, which results in the decay of a solid molybdenum component. Additionally, molybdenum has difficulties with fabrication due to its ductile-to-brittle transition temperature (DBTT) being close to room temperature, depending on the microstructure. [12]

The process for molybdenum production is shown in Figure 1.1. The process begins by mining molybdenite ore (MoS_2) and converting it into technical molybdic oxide (MoO_3). This conversion is done by using a Nichols-Herreshoff type multiple hearth furnaces, in which molybdenite concentrate is fed from the top against a current of heated air and gases blown from the bottom. This exothermic reaction requires coolant to prevent the molybdic oxide to reach 650 °C, because it will sublimate from a solid into a gas. After the sulfide concentration is less than 0.1 wt%, the remainder of the process follows the diagram depicted in Figure 1.1. [13]

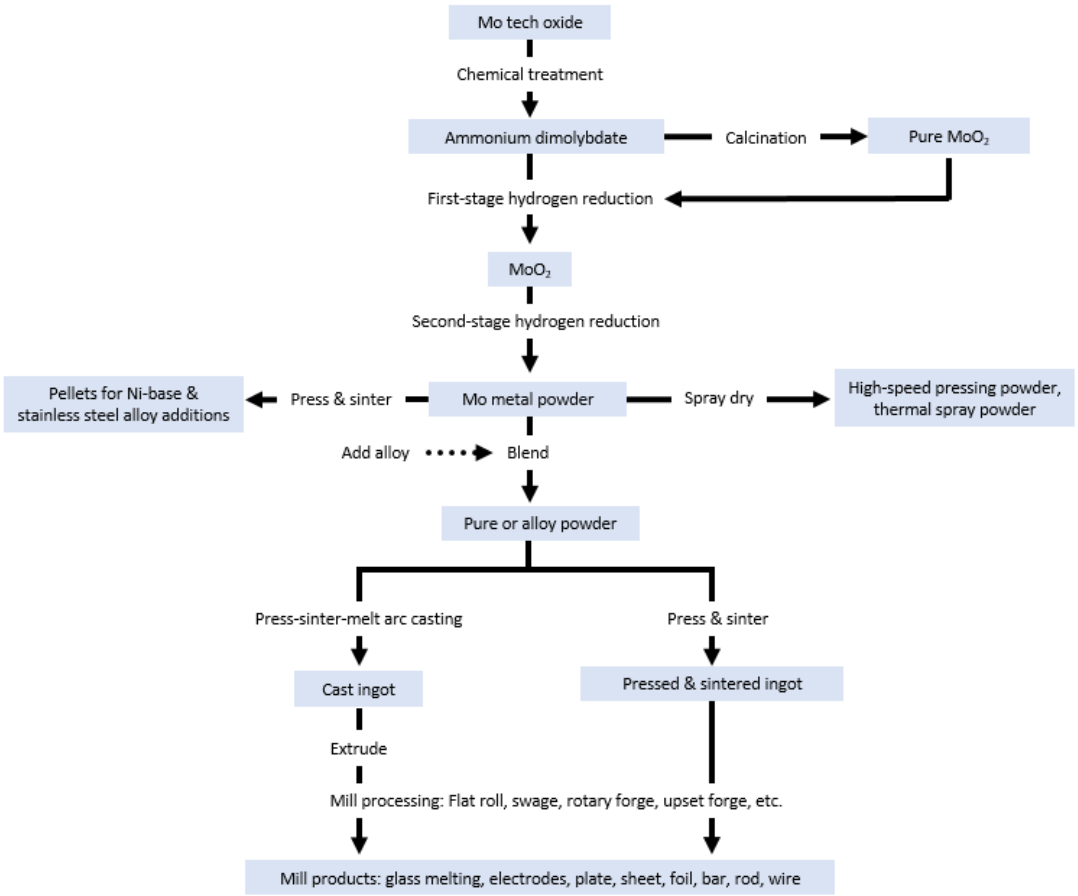

Figure 1.1: Flow chart showing steps involving molybdenum production. *Source:* www.imoa.info

The major use of molybdenum is as an alloying element in various steels; molybdenum improves high temperature strength, creep resistance, and corrosion resistance. Stainless steels account for ~22% of molybdenum, while engineered steels account for ~41% by weight. [13] Molybdenum is preferred over other refractory metals because of its lower density and reduced cost. Molybdenum casting must be done in an inert atmosphere due to molybdic oxide formation, which adds cost to the process. Another way to produce molybdenum alloys is by sintering molybdenum powder; the molybdenum alloys used in this research were sintered. [13]

1.5.2 TZM

TZM (0.5 wt.% Ti, 0.08 wt.% Zr, Bal. Mo) is a well-established molybdenum alloy and is considered a particle strengthened material. TZM consists of molybdenum matrix with dispersed titanium and zirconium carbide particles. Alloying elements, titanium and zirconium, serve as 'getters' because of their affinity for reacting with carbon. The presence of these dispersed carbides within the grains, prevents grain growth at higher temperatures, increases strength, and lowers ductility compared to pure molybdenum. The strength of TZM comes from a few strengthening mechanisms, some of which include particle strengthening due to TiC and ZrC, subgrains and elongated 'pancake' grains found in the longitudinal orientation of the rolled wrought microstructure, and ductile laminate layers. These strengthening mechanisms make TZM stable upwards of 1400 °C, until recrystallization occurs. [57, 58]

1.5.3 Mo-La

Mo-La or Mo-La_2O_3 alloy has finely distributed lanthanum oxide dispersoids throughout its molybdenum matrix. This alloy is known as oxide dispersion strengthened alloy (ODS). The lanthanum oxide (also called lanthana) particles strengthen molybdenum by preventing grain size increase at higher temperatures, impedes the movement of grain boundaries and dislocations, which improves strength and creep resistance. [59, 60] The presence of finely distributed oxide particles also lowers the ductile-to-brittle transition temperature (DBTT), depending on the volume fraction and radius of the particles. For this research, 2 vol. percent of lanthanum oxide with particle sizes of ~50 nm in mean diameter lower the DBTT to below -50 °C and increases the recrystallization temperature to above 1800 °C. [59, 60]

1.6 Current Applications of Molybdenum

Molybdenum based materials are used in various applications throughout the world and a multitude of industries. Molybdenum is used in lighting, electrical devices, medical equipment, high temperature furnace applications, X-ray tubes, hot-work tooling, and thermal coating. Table 4 shows which property of molybdenum is useful for the application in which it is used. It can be seen from Table 1.4 that molybdenum heat sinks are excellent heat sinks for silicon chips because of the nearly identical thermal expansion without compromising with density, electrical and thermal conductivity, and bond strength. With excellent combinations of mechanical and physical properties such as high temperature strength, creep resistance, toughness, thermal conductivity, and thermal expansion coefficient, molybdenum has good characteristics required for a structural material.

Table 1.4: Selected applications and properties required of molybdenum. *Source: www.imoa.info*

Property	**Application**								
	Halogen lamp	Heat sinks	LCD & photo-voltaic	Semi-conductor manufa-cturing	X-ray tubes	Hot-work tooling	Liquid-metal and glass processing	Furnace compo-nents	Surface Coating
Physical Properties									
Density		x							
Electrical conductivity	x	x	x		x		x	x	
Thermal conductivity		x			x	x	x		
Thermal expansion	x	x	x		x	x	x	x	
Mechanical Properties									
Elastic modulus	x	x		x	x	x	x	x	
Hot strength	x			x	x	x	x	x	
Creep resistance				x	x	x	x	x	
Other Properties									
Wear/Erosion resistance	x					x	x		x
Corrosion resistance	x		x	x			x		x
Bond strength with substrates	x	x	x		x				x

1.7 Potential Nuclear Energy Applications of Molybdenum

The potential for molybdenum and other refectory metals is highest as fuel cladding materials and as a matrix in some dispersion fuel forms. This is applicable to certain Generation-IV reactors, space fission reactors, and nuclear thermal propulsion reactors. Refractory metals add a level of safety due to their high melting point and most have excellent creep resistance properties. These metals show the required physical properties including corrosion resistance, low neutron absorption cross section (transparent to neutrons), operation temperature compatibility, thermal conduction, irradiation stability, and great mechanical strength properties. [12] Molybdenum does have compatibility issues with oxidizing coolants; this would eliminate any reactor design which uses water or an oxidizing gas which would eliminate the super-critical water-cooled reactor. [10]

The operating temperature needs to be considered due to irradiation embrittlement. Figure 1.2 shows the operating temperatures certain materials need to be reach certain level to reverse the neutron damage effect. [12] The refractory metals need a higher operating temperature. At a minimal, molybdenum would need an operating temperature of 1000 K (727 °C) and can go as high as 1700 K (1427 °C). This operating range would eliminate sodium cooled reactors and would demand higher operation temperatures of the other Generation-IV reactors. Lastly, molten salt reactor (liquid fuel) uses a graphite core instead of traditional fuel cladding. [12]

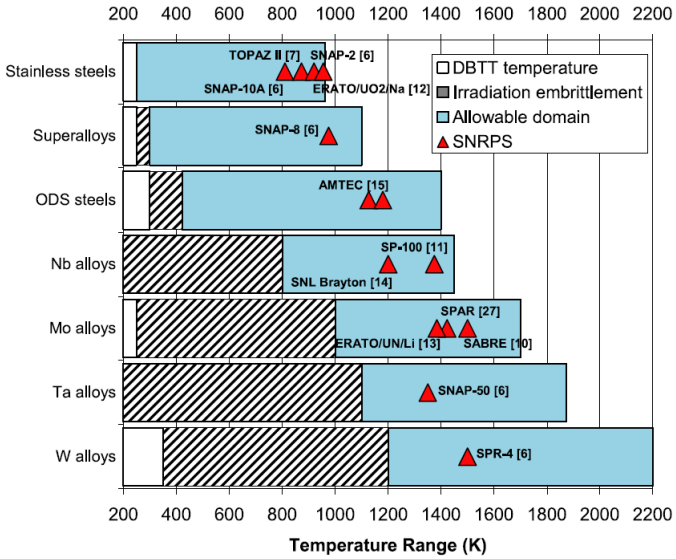

Figure 1.2: Recommended operation temperature range for structural materials in space nuclear power systems. [12]

1.7.1 Generation-IV Reactor Candidates

Of the six Generation-IV reactors, two reactor designs could use molybdenum as a fuel cladding material. These two Generation-IV reactors include lead-cooled fast reactor (LFR) and gas-cooled fast reactor (GFR). Both have coolant and operation temperature compatibility, and both have fast neutron energy spectrums instead of using thermal neutrons. Thermal neutrons have a kinetic energy of 0.025 eV which corresponds to a neutron speed of 2,200 m/s, while a fast neutron has a kinetic energy of about 1 MeV which corresponds to a neutron speed of 14,000 m/s. [14]

1.7.1.1 Lead-Cooled Fast Reactor (LFR)

Lead-cooled fast reactors are terrestrial fission reactors designed for generating electrical power. Figure 1.3 shows a schematic of a LFR. They use molten lead or lead-bismuth eutectic (LBE) as the coolant, have a fast neutron spectrum, and have a higher operating temperature.

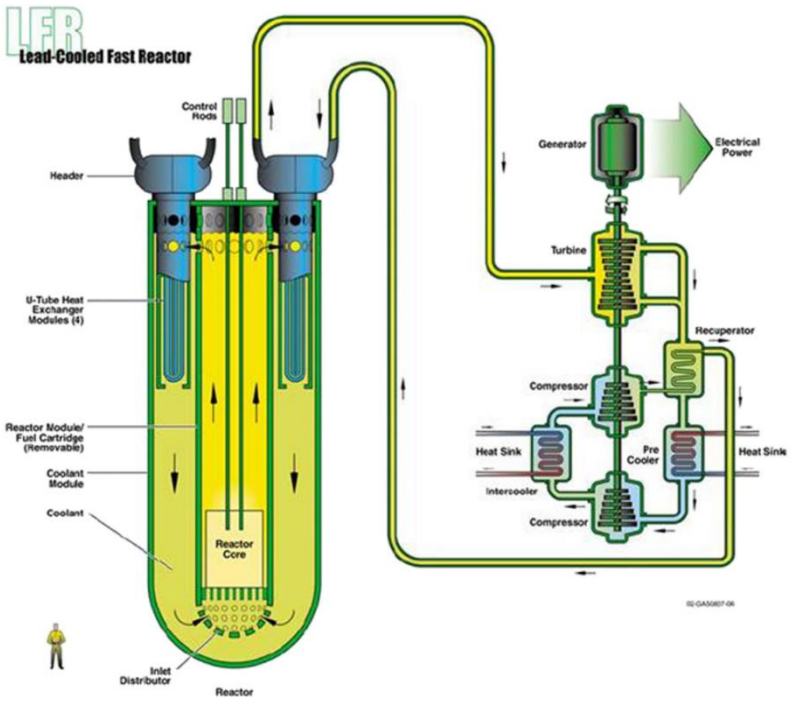

Figure 1.3: Lead-Cooled Fast Reactor (LFR) design. [7]

Lead coolant has great thermodynamic properties compared to other coolant types and is chemically inert. [19] One of the benefits of LFR is that it is a closed fuel cycle reactor enhanced

by the fertile conversion of uranium. A closed fuel cycle would drastically reduce the number of years for which nuclear waste needs to be stored because of radioactive decay. [15] Additionally, LFR can be used as a burner reactor which could use the already existing nuclear waste from previous LWRs, and convert the remaining nuclear materials and actinides left. It increases the safety of a nuclear reactor due to the lower pressure of the coolant and the closed fuel cycle ensures that nuclear waste will not be a burden to future generations. [15]

LFR has three general system sizes, the 600 MWe European Lead-cooled Fast Reactor (ELFR), the 300 MWe Russian BREST-OD-300 reactor, and the 20 MWe United States Small Secure Transportable Autonomous Reactor (SSTAR). While these reactors are designed to operate at ~550-650 °C, the boiling point of pure lead is 1749 °C and lead-bismuth eutectic is 1670 °C, which means the operating temperature could go higher depending on the cladding material. Additional research on if lead or LBE reacts with molybdenum or other cladding materials would need to be researched and especially at higher temperatures. [16,17]

1.7.1.2 Gas-Cooled Fast Reactor (GFR)

Gas-cooled fast reactors are terrestrial fission reactors designed for generating electrical power. GFR uses gas, such as helium, carbon dioxide, or steam, as coolant and have a fast neutron spectrum. [18] The reactor core temperature is ~850 °C and under a pressure of 7 MPa (for helium) and 25 MPa (for super critical CO_2) due to the poorer heat transfer of gases. More mass flow of gas is required to cool the reactor down, this adds safety concerns because of high pressures and higher temperatures, which means more research in materials, such as ODS alloys, refractory materials, and SiC to see if they could handle the environment. [18] However, a benefit of GFR is the direct Brayton closed-cycle gas turbine which results in high thermal efficiency, this is shown in Figure 1.4 as the scheme for GFR. [19]

The advantages to a GFR are as followed: obviating the need for an intermediate coolant loop, negligible activation of coolant, optically transparent which simplifies inspection, gas coolant does not change phase, and potential to become a breeder reactor. [7] Some disadvantages are: higher pumping power compared to liquid coolant, need high pressures which decrease safety, gas coolant requires artificial roughening of the cladding material to maintain acceptable cladding temperature, high coolant flow velocity can lead to significant vibrations of the fuel

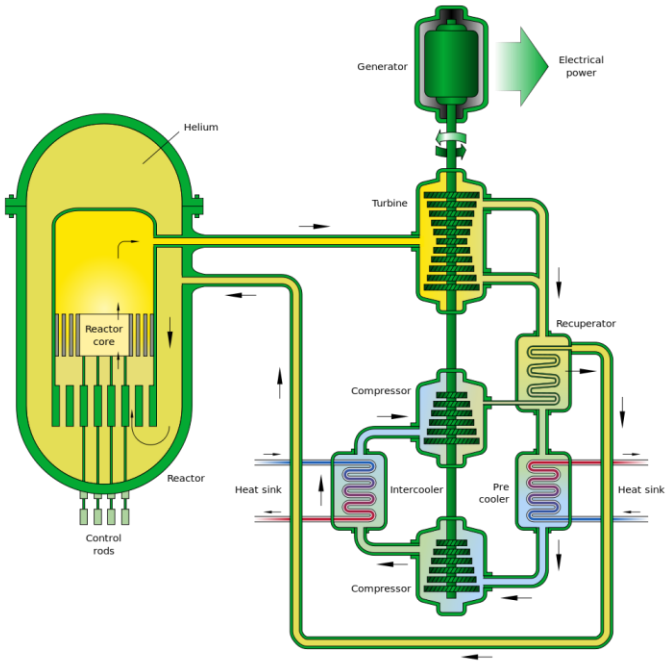

Figure 1.4: Gas-Cooled Fast Reactor (GFR) design. [7]

pins, and decay heat extraction has large requirements in case of emergencies. [7] GFR designs range in size and power output, of the current designs include 50, 600, and 2400 MW_{th} of power generation. The main structural material is SiC, but other materials like refractory metals, ODS alloys have potential. [18, 19]

1.7.2 Space Fission Reactors

Space fission reactors have had a renewed interest in the recent decades for future NASA missions and long-term space travel. These Space Reactor Power Systems (SRPSs) can enable missions to Mars, Jupiter, and other deep space exploration. SRPSs can provide reliable power in the 100s to 1000s of KW_e and can last for up to a 15-year mission. Potential SRPSs technologies have either heat pipe cooled, liquid metal cooled, or gas cooled designs. Each

design will have unique material needs along with advancements in technology to make SRPRs a reality. [20]

Each of these designs have benefits and limitations; heat pipe reactors offer cooling redundancy and can be restarted from a frozen state without complications, but heat pipes add complexity when designing the reactor due to the number of them and the compact space allotted. [20] For a liquid metal coolant system, an external or auxiliary heating system would be required to melt the metal prior to the reactor being turned on. Lastly, a gas-cooled reactor does not need to be thawed, but an issue is the pressures required to add size and mass to the reactor's cooling system. These systems would not be used for launching into space and would only be used once in space. Due to the compact space and concerns with mass, smaller space fission reactors would require higher enriched fuel of uranium ~50-95 wt%, which means more neutron leakage and requires additional safety measures. A generic layout of a SRPS is shown in Figure 1.5. [20]

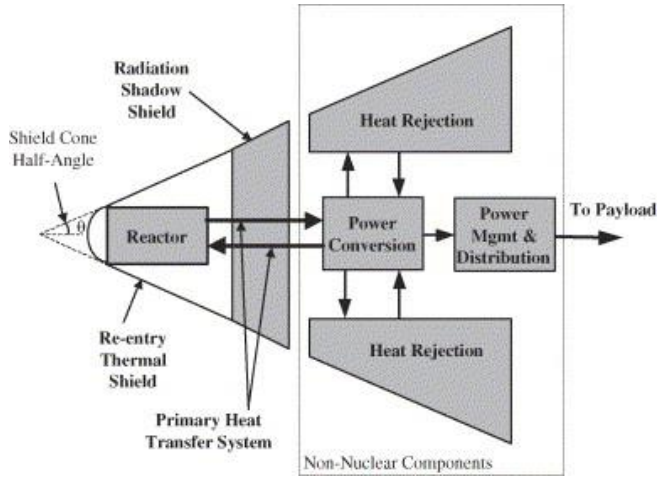

Figure 1.5: Generic layout of a space nuclear reactor power system. [20]

system would be separate from where any humans or payload would be located. A huge concern for SRPSs is maximizing safety while maintaining smaller compact designs. To do this, designs need to avoid single-point failure in the cooling system, to ensure if something happens to a coolant pipe, alternate routes are available. [21] This can be seen in Figures 1.6 and 1.7, both are SRPSs designs which utilize a different cooling technique. Figure 1.6 is a schematic of a Scalable AMTEC Integrated Reactor Space Power system, SAIRS reactor, which employs a fast neutron spectrum nuclear reactor cooled with a multitude of sodium (Na)

heat pipes. The SAIRS reactor can be designed to scale up to various power needs. Figure 1.6, shows the SAIRS hexagonal fast-spectrum nuclear reactor which is cooled with 60, 1.5 cm OD, Mo-14%Re sodium heat pipes. [21]

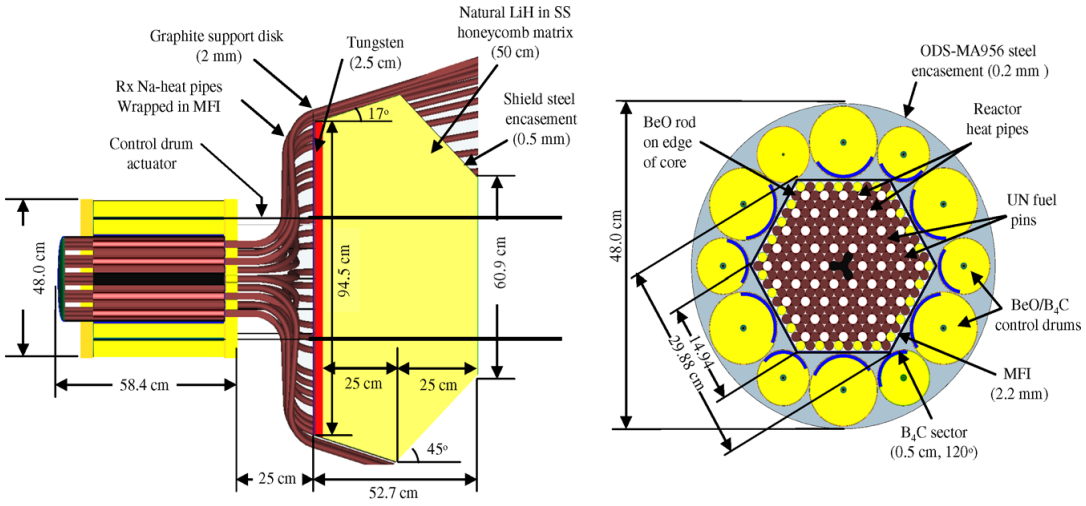

(a) Arial Cross-section in SAIRS Reactor and shield. (b) Radial Cross-section in SAIRS Reactor.

Figure 1.6: Cross-sectional views of SAIRS reactor and radiation shadow shield. [21]

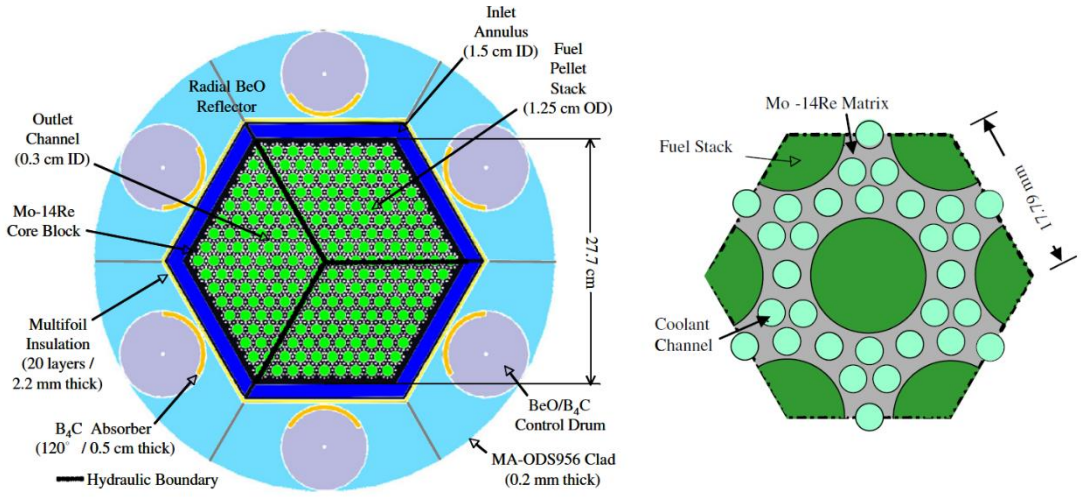

(a) Radial Cross-Section of S^4 Reactor. (b) Fuel Elements - Coolant Channels Unit Cell.

Figure 1.7: A radial cross-section of and the arrangement of UN fuel and coolant channels in S^4 reactor. [21]

Another SRPS as shown in Figure 1.7 is the submersion-subcritical safe space (S^4) reactor power system. The reactor has a hexagonal, Mo-14%Re solid core with cylindrical cavities loaded with UN fuel pellets. From Figure 1.7b, the coolant channels are shown, a coolant of He-Xe binary mixture would flow through the Mo-14%Re core to cool the reactor and generate 471 kW_{th} of power. [21] The S^4 reactor has a unique design in which it is divided into three

sections, that are thermally and neutronically coupled, but hydraulically decoupled. This is done to avoid single-point failure of the cooling system and requires additional closed Brayton cycles, radiator panels, water heat pipes, and a NaK-78 secondary loop. [21]

Material selection and engineering design are extremely important in SRPSs because of the stability these reactors need once they are out in space. A variety of potential fuel cladding materials and structural materials are shown in Figure 1.8. These potential materials include oxide dispersion strengthened (ODS) steels, iron-based superalloys, refractory metals, and 316FR stainless steel. [12] It can be shown, from Figure 1.8, that molybdenum alloys show the best stability and creep resistance at elevated temperatures. That is why molybdenum based materials are key candidates for some space fission reactors. However, as mentioned by El-Genk et al. [12], these refractory metals need to have new technologies and improvements in fabrication and joining techniques to make them more suitable with reduced costs for such application. [12]

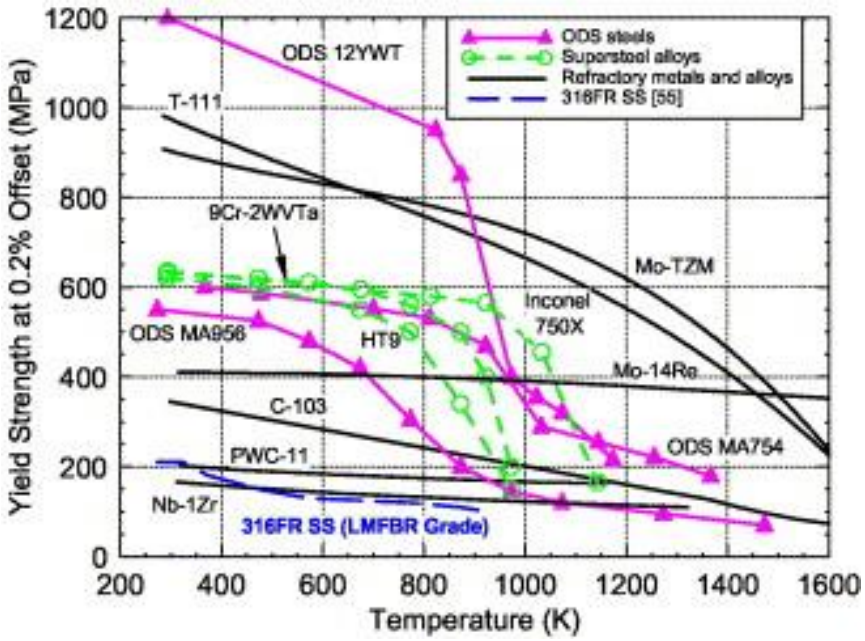

Figure 1.8: Comparison of the yield strengths of key materials for space nuclear reactors. [12]

1.7.3 Nuclear Thermal Propulsion

Nuclear thermal propulsion (NTP) system is a non-chemical propulsion technology. It uses heat generated from a fission reactor from a uranium-based fuel, to quickly heat up hydrogen to thrust a spacecraft. The fuel of the reactor needs to be able to withstand extremely high

temperatures greater than 2500 K (2773 °C) and have hot hydrogen erosion resistance, low neutron absorption cross section, retention of fission products/fuel, mechanical strength/structural stability, and thermal shock resistance. The GE710 program used cermet fuel, which consist of ceramic fuel particles of uranium mononitride (UN) or uranium dioxide (UO_2) dispersed in a refractory material matrix such as tungsten or molybdenum. [22, 23]

The schematics in Figure 1.9 shows a NTP system design (left) and the system where fuel would interact with the hydrogen (right), respectively. Currently, fuel matrix choice is tungsten based alloys, because of their higher melting point (3422 ^oC) than any other metals. [24] While tungsten does have a larger melting point than molybdenum, both have similar issues with welding and fabrication, which would be benefitted by this current research. Additionally, refractory and transition carbides, nitrides, oxides, etc. are being considered for low enriched uranium (LEU) NTP systems because of their high melting points. LEU NTP has been researched lately to replace the need for highly enriched uranium (HEU) which may be able to have similar performance without the danger enriching uranium to such a high amount. With any cermet fuel or matrix material used, new welding technologies will be needed and need to be studied. [24, 25]

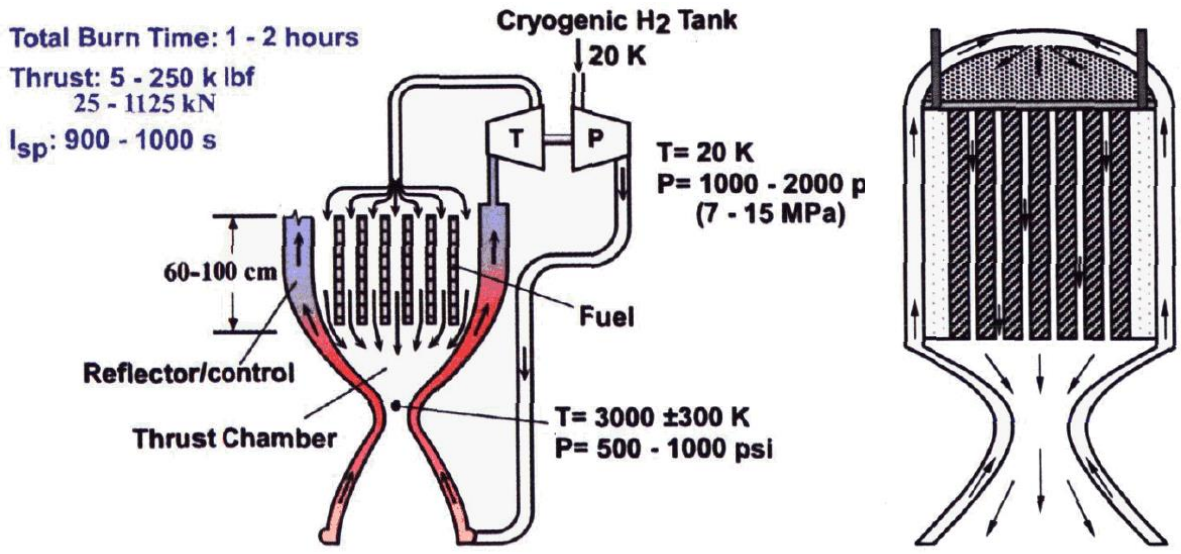

Figure 1.9: Schematics of the nuclear thermal propulsion system design. [22]

1.8 Welding of Molybdenum-Based Materials

Welding molybdenum, refractory metals like tungsten, and ODS steel have difficulties in joining and fabrication. Some of the issues which arise with refractory metals is due to oxidation of molybdenum at temperatures greater than 650°C. This rules out most fusion welding techniques under normal atmospheric conditions which consist of ~21% oxygen. For ODS alloys, the presence of the oxide particles makes joining difficult due to differing density and melting points of the metal matrix to that of the ceramic particle. If fusion welding occurs, the oxide particles lead to flocculation and coagulation of oxide particles to generate coarser particles. [26] This also applies to one of the molybdenum alloys being one of the focus of this thesis research, Mo-La, so by studying better welding techniques of molybdenum, this can also aid in research for other metals. Welding can be done for both similar metals and dissimilar metals, each type of joining requires knowledge of melting temperature, heat transfer, and oxidation. To further nuclear reactor technology, new techniques need to be developed and studied, whether this is fusion or solid-state welding. [26, 27]

1.8.1 Fusion Welding of Molybdenum

Fusion welding is the joining of two components, typically made of metals, by melting the interfaces and subsequent solidification of the adjacent components. Welding results in a metallurgical bond between the components rather than bonding to a filler as with soldering or brazing. There are many types of fusion welding techniques, which can be categorized as electrical or chemical. [28] Electrical refers to melting the base metal by an arc, laser beam, or induction. While chemical refers to using a fuel source such as an oxyfuel or solid reactant. Some examples of common welding techniques are shown in Table 1.5, which shows estimated cost, weld quality, heat affected zone (HAZ) width, automation, plate thickness, and addition characteristics. Each type of weld aims at welding different metals and some protect or prevent oxide build up with slags or inert gas flowing over the weld pool. A diagram of fusion welding is shown in Figure 1.10. [28, 29]

Table 1.5: Summary of fusion joining processes. [31, 32]

Process	Equipment Cost	Weld Quality	HAZ width [mm]	Automation	Plate Thickness [mm]	Characteristics
Shielded Metal-Arc Welding (SMAW)	$1500	poor	5-6	none	all (multi-pass)	very portable; electrode consumed; electrode coating acts as shielding gas
Submerged-Arc Welding (SAW)	$2000 - $10,000	good	7-10	very capable	all (multi-pass)	high productivity; good for thick plates; uses a granular flux; electrode consumed
Gas Metal-Arc Welding (GMAW)	$1000 - $3000	acceptable	3-4	capable	all (multi-pass)	simple process; productivity double of SAW; uses shielding gas; electrode consumed
Gas Tungsten-Arc Welding (GTAW)	$1000 - $5000	good	2-3	capable	all (multi-pass)	good for thin plates; uses filler materials; uses shielding gas; portable; non-consumed electrode
Laser Beam Welding	$40,000 - $1million	very good	<0.5	very capable	25 – 30	no filler materials; low distortion; good for thin plates
Electron Beam Welding	$75,000 - $1million	very good	<0.5	low	150 – 250	requires vacuum; low distortion; no filler materials; all materials can be joined

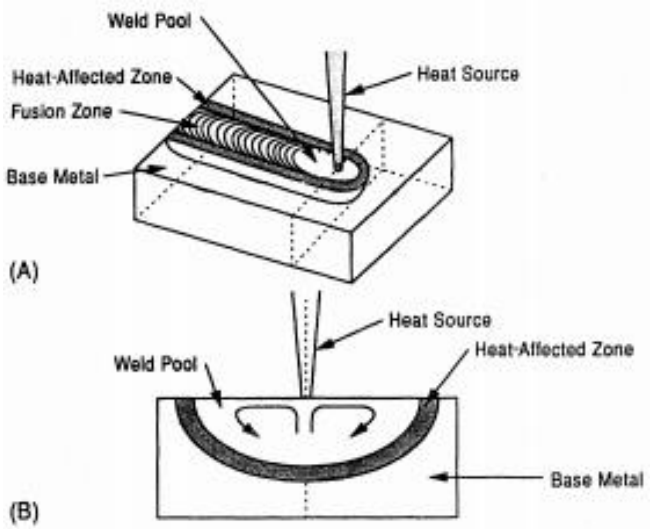

Figure 1.10: Schematic diagram of the fusion welding process:
(a) interaction between the heat source and the base metal;
(b) transverse section. [28]

The HAZ creates a lot of issues in welding and is typically where failure occurs. [28] Microstructural changes such as the change in grain size, changes in phase (e.g. in welding martensitic material: γ + ferrite → martensite + ferrite) and adding impurities such as oxides or carbides occur in the HAZ. [30]

For fusion welding molybdenum and other refractory metals, joining above the ductile-to-brittle transition temperature (DBTT) is important as well as reducing the presence of oxygen, nitrogen, and carbon. For pure molybdenum the DBTT falls around room temperature while tungsten's DBTT is up to ~370°C. [12] The presence of oxygen, nitrogen, and carbon negatively affect the DBTT and creates unwanted intermetallic compounds which can lead to failure of the material under stress. For molybdenum, if oxygen is present above 650 °C, MoO_3 forms, which leads to cracking at the weld surface. Tadayuki Fujii and Gary A. Rozak [33] have demonstrated how even low amounts of oxygen present during gas tungsten arc welding (GTAW) welding can create cracks, Figure 1.11. Any amount above 16 ppm of oxygen leads to the crack development on the surface and generation of pores on a pure molybdenum plate, during GTAW. [33, 34]

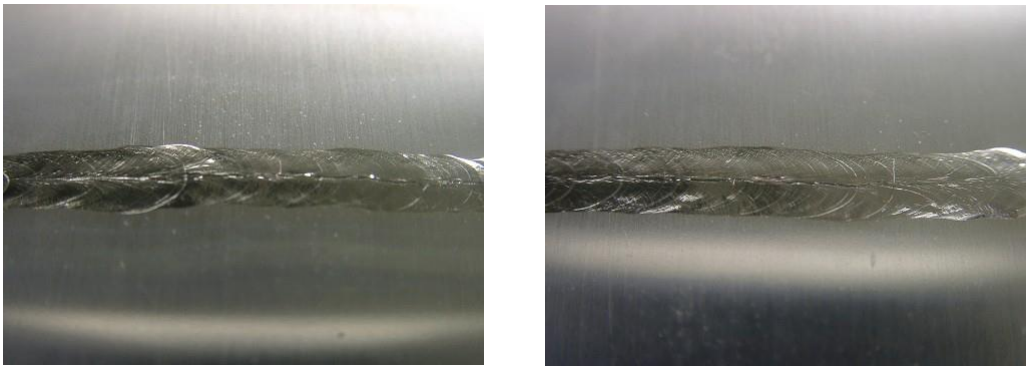

(a) 69ppm O_2 (b) 78ppm O_2

Figure 1.11: Typical microstructures showing bead cracking after TIG-Weld (GTAW) Mo sheet made by H.C. Starck, Inc. [34]

Since oxygen contamination also affects the weld quality of molybdenum, fusion welding needs to be done under vacuum or a controlled argon gas environment. This would greatly increase the cost of welding, while still having a HAZ. To minimize the HAZ, fusion techniques such as laser beam welding (LBW) and electron-beam welding (EBW) could be used. [31] These techniques deliver high energy density to the precise joining interface. The high energy density reduces the spread of the heat and results in a better weld. These welds exhibit good ductility and strength, however also cost substantially more than the traditional methods. [31]

1.8.2 Solid State Welding of Molybdenum

Solid state welding is the process of joining two adjacent surfaces without melting or introducing a liquid phase. In theory, solid state joining can be achieved if the two surfaces are clean and enough pressure is applied to bring the two surfaces atomically close. Heat can be applied to the materials to make diffusion of atoms easier to create a better metallurgical bond. Solid state joining techniques are preferred over fusion welding techniques when a material has a complex microstructure which would be altered due to the HAZ, has the presence of fine dispersoid particles or particles which have different densities and melting points than the base material, or if retention of joint strength is highly important. [31]

The next few sections goes over some typical solid-state welding techniques and ends with pressure resistance welding, which is the focus of this thesis research.

1.8.2.1 Friction Welding

Friction welding is a welding technique which joins two metal components by generating heat at the interface through mechanical friction. Typically, this is done by rotating tubes or rods at the interface while applying a unilateral force. The force is called 'upset' and is enough to push the heated interface once the metal becomes plastically deformed. [35] This force pushes the plastically deformed material out from the interface into an expulsion region as shown in Figure 1.12. Friction welding can be done either in atmospheric conditions or under a liquid such as oil as done by Andrzej Ambroziak [35]. For welding molybdenum, friction welding has been shown to be a very effective welding technique and can be used to weld similar and dissimilar metals. [35-37]

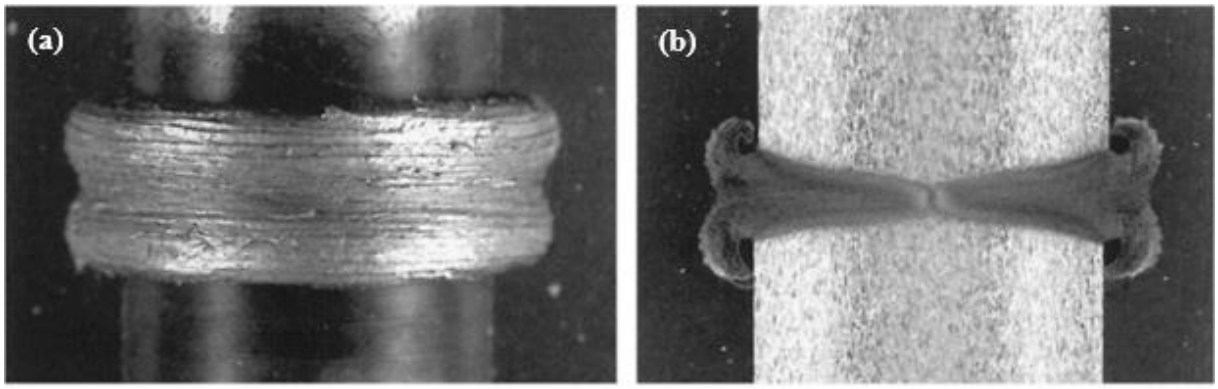

Figure 1.12: (a) Photo and (b) metallographic section of friction welded TZM. [36]

1.8.2.2 Friction Stir Welding

Similar to friction welding, is a popular technique called friction stir welding (FSW), which uses a rotating cylindrical tool with a profiled probe to join two clamped pieces. As shown in Figure 1.13, the rotating cylindrical tool heats up the material at the interface, as a butt joint, and mixes the material in the 'stir-zone'. This 'stir-zone' consists of a fine dynamically recrystallized grain structure due to the intense heating and severe plastic deformation from the rotating tool. This results in a thermos-mechanically affect zone (TMAZ), which also changes the microstructure of the weld and affects recrystallization and grain growth due to high temperatures and induced deformation. [38, 39]

Both friction welding processes have TMAZ areas as well as HAZ, however, the HAZ area is minimal compared to fusion welding. The TMAZ is represented in Figure 1.14, which shows the different distinct zones of the FSW process. Friction stir welding can be done on a wide range of materials; the limiting factor is the tool material. The tool is typically tungsten because of its high melting point but other materials are used, traditionally, friction stir welding is done on aluminum and steel alloys. Fujii et al. [61], showed that commercially pure molybdenum of 1.5 mm thickness could be friction stirred welded using a Ir-Re alloy tool while still retaining 86% of its strength compared to the base material. [61]

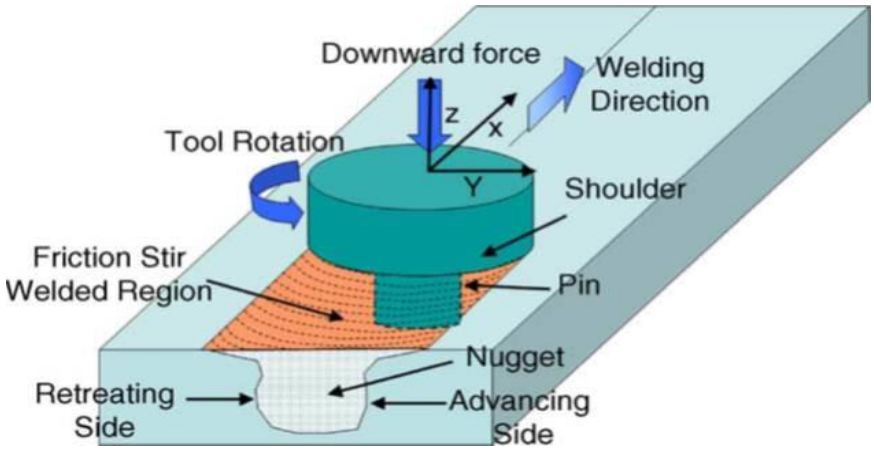

Figure 1.13: Schematic drawing of the friction stir welding process. [38]

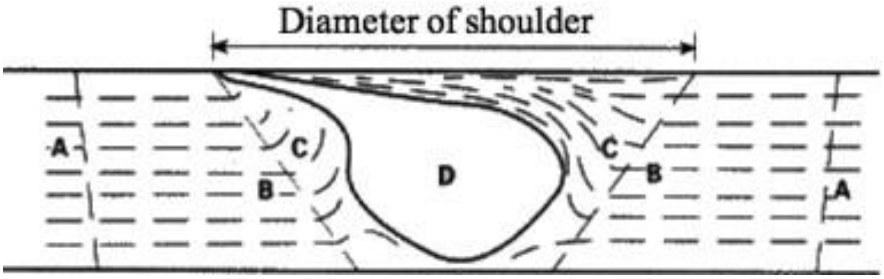

Figure 1.14: Schematic cross-section of a typical FSW weld showing four distinct zones: (A) base metal, (B) heat-affected, (C) thermo-mechanically affected and (D) stirred (nugget) zone. [39]

1.8.2.3 Explosion Bonding

Explosion bonding is a joining technique mainly used to join two dissimilar metals on a larger scale. This process uses controlled explosions from one side of a material to the other to join two plates together. A large drawback for explosion bonding is its limited geometry. [40]

However, it is an excellent bonding technique which yields minimal heat generation and produces great metallurgical bonds. A schematic of the explosion bonding process is shown in Figure 1.15, which shows how the materials bond at varying location on the plate. This offset and delay of explosions ensure a minimal amount of trapped gas and improves the weld quality. [40]

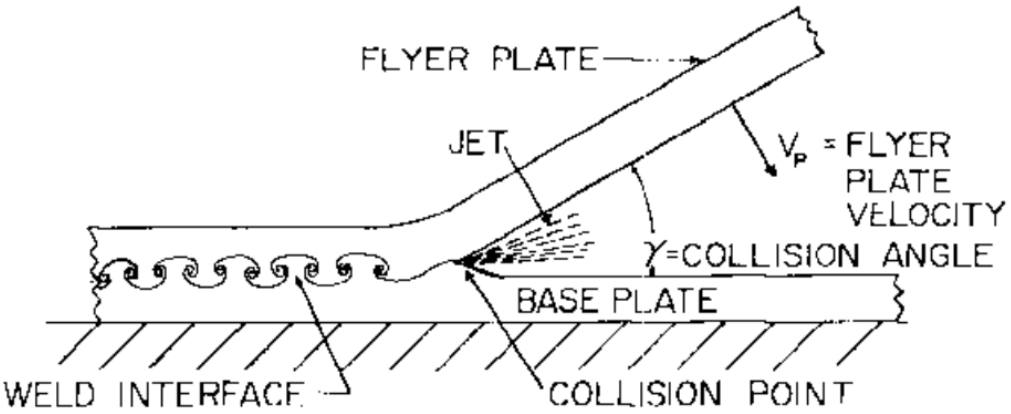

Figure 1.15: Schematic of an oblique collision like that in an explosion welding operation. [40]

While explosion bonding has many advantages, it is a dangerous process which requires special explosive expertise and government approval.

1.8.2.4 Magnetic Impulse Welding

Magnetic impulse welding or magnetic pulse welding (MPW), is a joining technique which uses magnetic forces to weld two components together. MPW is compared to explosion welding because of the high velocity the atoms collide with the bonding material. Like explosion welding, MPW can weld similar and dissimilar metals. [41] The process for MPW is based on magnetic pulses of less than 100 μs, this is done by discharging capacitors quickly through a low induction coil. A repulsive force is produced between the magnetic field in the cladding, and the magnetic field in the coil. This causes the cladding to rapidly collapse onto the end-plug creating a solid-state joint. This welding process is more efficient for conductive materials. However, since this process works similarly as explosion welding, brittle metals such as molybdenum and tungsten may have issues. [41, 42]

The MPW process has had a lot of interest in welding fuel pins for the nuclear industry as shown in Figure 1.16. Research has shown the success for welding end-plugs to cladding fuel rods;

however, more research needs to be done for refractory metals and ODS iron based alloys. The advantages of the MPW are ability to weld dissimilar metals, no filler materials required, weld various configurations, quick welding process, no HAZ, and can be scaled up. [41]

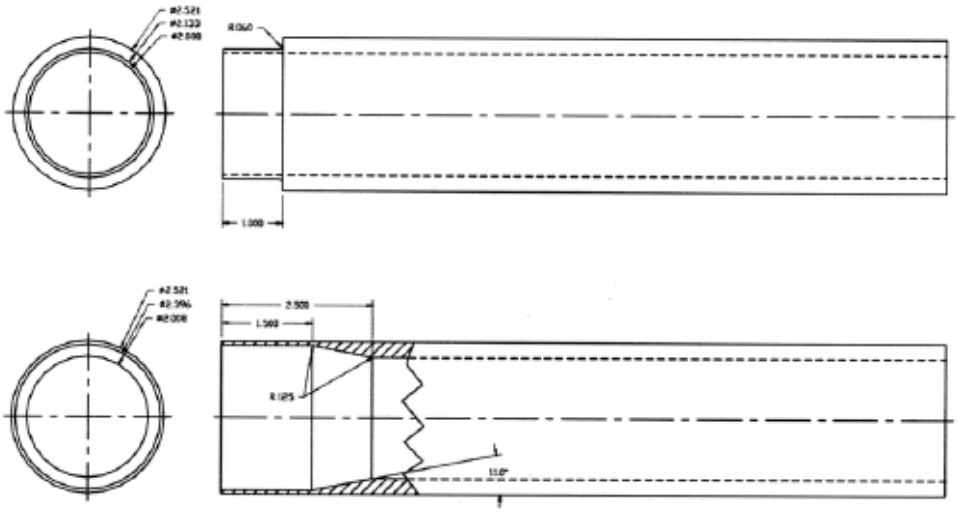

Figure 1.16: Lap joint configuration for joining end-plugs to fuel pin cladding in magnetic impulse welding. [42]

1.8.2.5 Diffusion Bonding/Pulsed Plasma-Assisted Sintering

Diffusion bonding/pulsed plasma-assisted sintering (PPAS) is a joining technique which joins two flat and cleaned surfaces by applying axial force and holding the components together at a high temperature below the material's melting temperature. This process promotes diffusion of atoms across the weld joint interface and creates a sound joint. The pulse is due to electrical current passing through the material at a constraint rate and amount to heat the material. This process is the same for sintering in a spark plasma sintering (SPS) system. [43]

A diagram of the SPS system is shown in Figure 1.17, typically for sintering, powder is compressed in a graphite die as shown in Figure 1.17. The graphite die is a cylindrical piece with a cylinder opening, this opening is where to graphite punches of similar size, to that of the opening, are used to compress the powder together and aids in passing the current through the material. [43] Electrodes are built into the press of the SPS system (segment 2 in Figure 1.17), a thermal couple is placed in a small hole on the side of the graphite die to measure internal

temperatures (segment 8 in Figure 1.17) which feedbacks to the control system. For high melting point materials, even ceramics, a pyrometer can be used to measure temperature. [43]

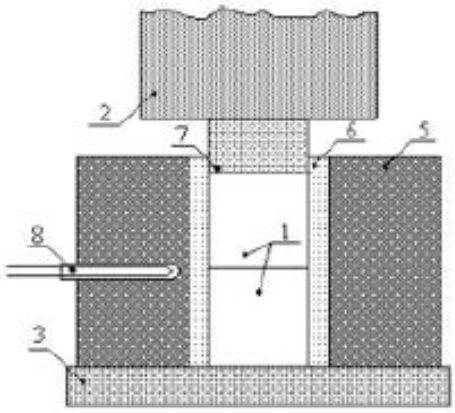

Figure 1.17: PPAS schematic of joining samples. 1-samples to be joined; 2-ram/upper electrode; 3-lower electrode; 4-pyrometer (not pictured); 5-die; 6-die cladding; 7-die punch; 8-thermal couple. [43]

The PPAS technique has been proven to work to join ODS alloys and can be used for post-bonding heat treatment. Grain growth occurs due to the ability to hold the samples at elevated temperatures. Additionally, the SPS system is operated under a high vacuum and flushed with argon, which allows for the sintering or joining of oxygen sensitive materials such as molybdenum or tungsten. [43] A drawback of this process is the diffusion of carbon on the outer surface of the material. Since graphite die, punches, and foil are used in the operation of the SPS/PPAS system, carbon atoms may diffuse into the surface of the material. This could be an issue and would require machining of the sample to remove the impurity. [43]

1.8.2.6 Pressure Resistance Welding

Pressure Resistance Welding (PWR), is a joining technique which uses a combination of uniaxial pressure and electrical resistance induced heating to join two components. It was initially developed at the Argonne National Laboratory (West) in Idaho (ANL-W) but was further developed in Japan's fast reactor program following the shutdown of EBR-II [44]. The energy input is based on the Joule heating principle, shown in Equation (1), where high current is passed through a material and the resistance will be the highest at the interface of the two pieces. PRW can be used to weld similar and dissimilar metals. The amount of current needed

to weld depends on the resistance of the materials being welded, the PRW has adjustable parameters for current, voltage, and force applied.

$$H = I^2 \cdot R \cdot t \tag{1}$$

where H = total energy [J], I = current [A], R = resistance [Ω], and t = time [s]. Resistance welding is widely used in different industries, spot welding is a form of resistance welding commonly used in the automobile manufactures and applies a large amount of current on a focused area to join thin metal sheets. The spot welding process is typically done autonomously and only takes about a hundred milliseconds. [45]

Pressure resistance welding is a modified spot welder which simultaneously applies force on the components. Applying force, typically 1000lb_f, helps improve the weld bond and expels any oxide formation and does not require full melt of the interface. A schematic of the PRW system is shown in Figure 1.18, Larry Zirker and Craig Tyler [47], showed PRW's capabilities with joining high temperature metals with a tube configuration. Additional instruments are used to calibrate the force applied and to measure the current passing through. The expulsion region is machined off and the surface is cleaned, this is similar to what happens in friction welding, Figure 1.12, which is an industrial process and can be accomplished easily. [45-47]

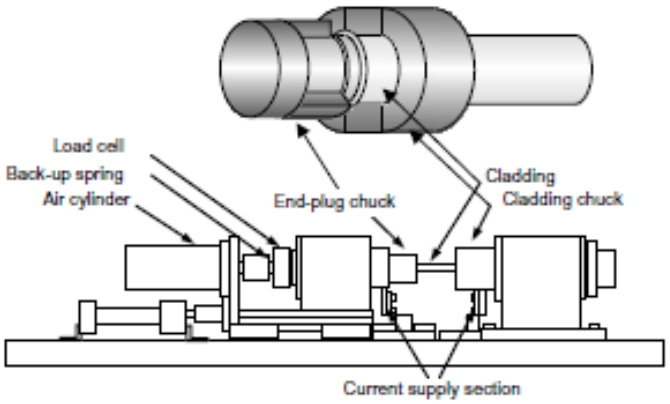

Figure 1.18: Schematic of the pressure resistance welder PRW unit. [46]

The PRW system has a lot of interest in welding metals, refractory metals, ODS iron alloys, and alloys with unique microstructures. Much research has been done with welding different ODS iron alloys MA957, MA956, and MA754 and the F/M alloy HT9. [48] Additionally, refractory metals like tungsten were welded and become the foundation of this research. This research will focus on PRW of pure molybdenum, TZM, and Mo-La.

2.0 Experimental Procedures

2.1 Molybdenum Alloys

The three molybdenum alloys used in this study were pure molybdenum, TZM, and Mo-La. These alloys were prepared by H.C. Starck by blending molybdenum powder and powder alloy elements, afterwards apply cold isostatic pressing (CIP), then in a hydrogen atmosphere sinter at a temperature greater than 1650 °C, ending with hot roll billet to plate.

The molybdenum rods were provided from an unknown source, but its composition was determined to be pure molybdenum via energy-dispersive X-ray spectroscopy (EDX) in a scanning electron microscope. The compositions of the alloys are shown in Table 2.1. More information on the as-received material compositions can be found in Appendix A.

Table 2.1: Nominal compositions of molybdenum based materials used in this study.

	Composition (wt.%)				
Element	**C**	**Zr**	**Ti**	**La**	**Mo**
Pure Mo	Max: 0.01	-	-	-	99.95
TZM	0.02	0.08	0.5	-	Bal.
Mo-La	Max: 0.01	-	-	1.1	Bal.

Each of the as-received alloys underwent preliminary characterization to capture the microstructure and mechanical properties prior to joining. Optical microscopy was used to image the grain morphology of the wrought microstructure. Micro-hardness was used to gather the initial strength of the molybdenum alloys prior to joining.

2.2 Sample Preparation of Rods and Coupons

The samples were prepared by cutting the received pure molybdenum rod (3/4” diameter, 19 mm) into smaller cylinders of ~1.2 inch in length. A Kalamazoo metal cutting band saw with a water-based lubricant was used for cutting the rod. For further preparing of the molybdenum sample, a Nardini – MS 1640E lathe machine, water-based lubricant, was used to create two rods of 0.313 inch (7.95 mm) and 0.267 inch (6.78 mm) diameters with a length of 1 inch. Figure 2.1 shows the view of the rod samples prior to welding. The rod samples were ground

at the joint interface using 600, 800, and 1200 grit SiC to reduce surface roughness, remove impurities, and disrupt oxide layer at the interface. Additionally, the weldments were subjected to an ultrasonic cleaning bath first submerged in acetone and then submerged in ethanol to remove impurities. From there, the samples underwent the pressure resistance welding.

Figure 2.1: Molybdenum rods for PRW weldment.

Coupon weldment preparation was done by cutting the as received plates perpendicular to the rolling direction with a ~0.5 inch (12.7 mm) thickness. A Kalamazoo metal cutting band saw with a water-based lubricant was used for cutting the plate. The cut sample was then squared using an Acer 10 inch × 50 inch electric variable speed mill machine to create 90^{o} edges. The mill used a tungsten carbide drill bit (0.5 inch diameter), rotation at 500 rpm, and used a water-based liquid coolant.

Once 90-degree edges were achieved, the sample was milled to achieve the dimensions shown in Figure 2.2, the step-by-step preparation is illustrated in Figure 2.3. The coupon samples were ground at the joint interface using 600, 800, and 1200 grit SiC to reduce interface surface roughness and to disrupt the oxide layer. The weldments were subjected to an ultrasonic cleansing bath first submerged in acetone and then submerged in ethanol. From there, the weldments would undergo the pressure resistance welding process.

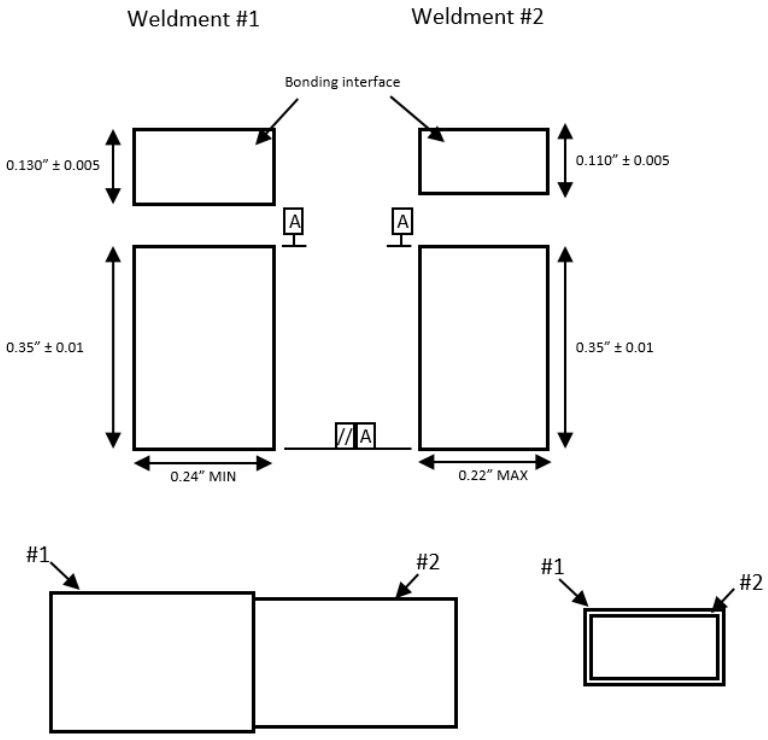

Figure 2.2: Coupon dimensions for PRW weldment.

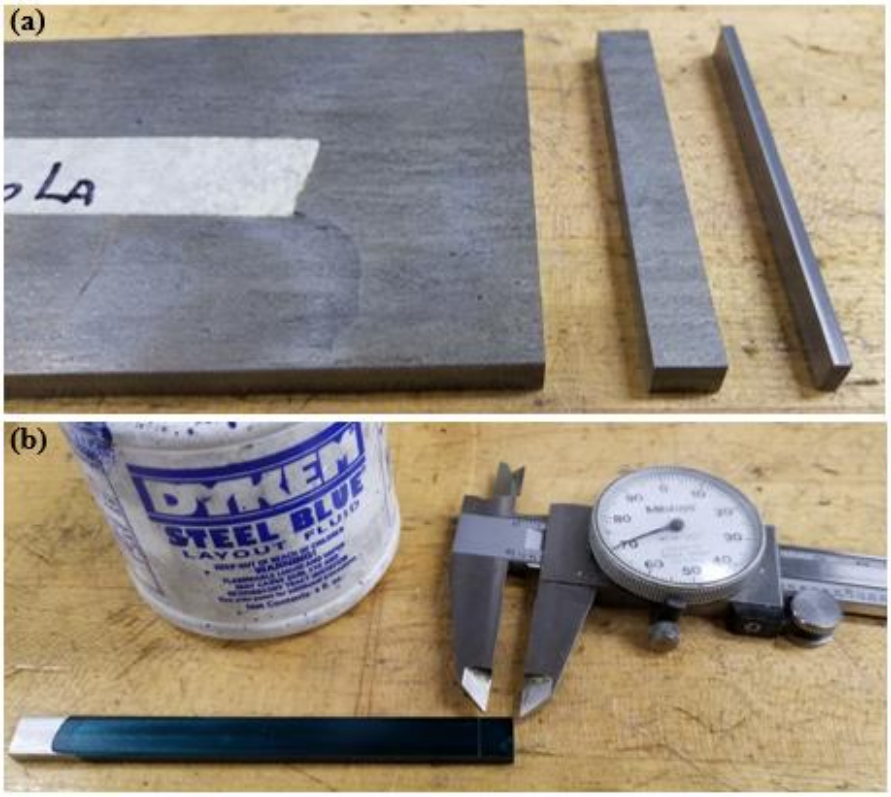

Figure 2.3: Coupon preparation from AR plate: (a) Plate of Mo-La, cut then milled (b) width measured and scored on steel blue layout fluid for additional cut, then milled.

2.3 Pressure Resistance Welding Process

The pressure resistance welding (PRW) process is a versatile joining technique which can be used to join pure metals, metal alloys, ODS alloys, and dissimilar metals. Since the PRW process is an electrical resistance-based joining technique, the electrical current applied would need to be adjusted to meet specific material properties. These properties include thermal conductivity, melting temperature, electrical resistivity, etc.

2.3.1 Pressure Resistance Welding Machine

The PRW equipment utilized for the study is a three-phase, 60 Hz, Voltza® Transgun procured from the Centerline Ltd. for the University of Idaho and was operated within the Advanced Materials Laboratory located at the Center for Advanced Energy Studies (CAES), Idaho Falls, ID. A 'C' style Transgun based on the electrode configuration as seen in Figure 2.4, uses an OHMA® activator cylinder, which is responsible for delivering the hydraulically powered force up to 1,200 lb_f (~5.34 kN). Connected in line with the hydraulic cylinder is the electrode ram and water-cooled end-plug fixture along with the adjacent electrode water-cooled cladding fixture. The opposing electrode is connected to the lower electrode arm, which is linked to the transformer, completing the electron flow path.

The transformer is powered by a 480 V line voltage, which has a turn ratio of 62:1 and operates in a high current, low voltage configuration. The welding control unit controls the process, but a handheld pendant known as the Medar is responsible for programming the welding schedules and executable variables as well as recording the operational data. In addition, data are also acquired through a separate device called 'The Wave'. This unit measures the current being passed by an inductance loop around the electrode arm as well as the voltage by clips attached to both fixtures. The data unit reports the current being passed, the voltage drop between the two fixtures, and the resistance. This data can then be transferred from 'The Wave' to the computer through the program, 'Inspector,' which reports the data as a function of time. [48]

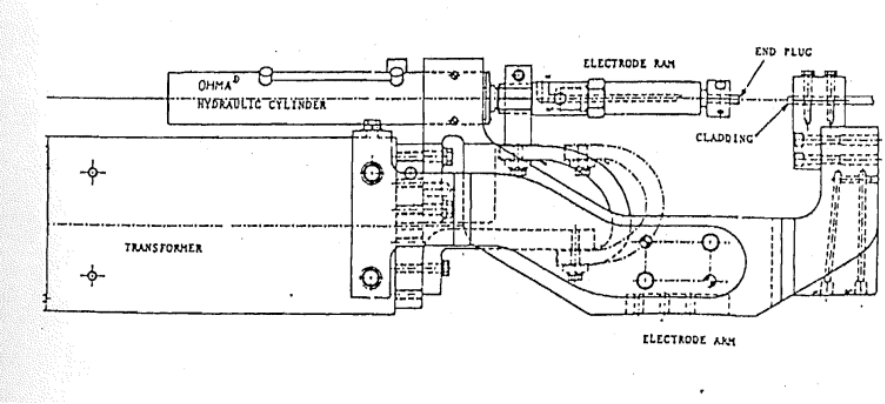

Figure 2.4: Schematic of PRW unit used for research study. [47]

There are several controllable variables that are found to dictate the bond integrity of the specimen. They are current, joining time, forging force and stick-out length. The current is programmed as a percentage (maximum current of 30kA) and joining time is in cycles based on the frequency 60 Hz (cycles/second) that the unit operates with. The forging force is applied by measuring air over oil pressure and has a set air pressure (psi) reading. That psi reading is translated back to pounds by manual measurements taken between the electrodes using a force gauge, as shown in Figure 2.5. The stick-out length is the amount of specimen material that protrudes out of each respective joining. [48]

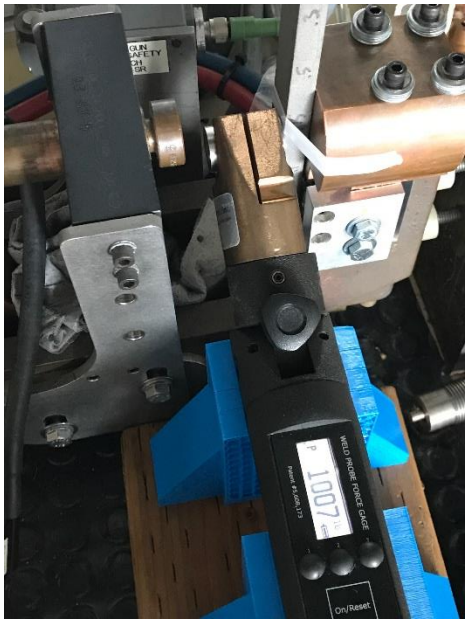

Figure 2.5: Weld force gun placement for force measurements between the PRW electrodes.

There exist other programmable variables such as the squeeze and hold time. The squeeze time is the amount of time the activator cylinder applies pressure to the specimen before applying a current. This phase in the joining process is important because the resistance at the interface is dependent on the ability to keep the surfaces in contact. Too short of a squeeze time may not lead to proper surface contact prior to current being passed, causing a large resistance and too much heat input. The hold time is the amount of time the electrode force is applied after the welding current has ceased. This phase continues to forge the joining inerface into one another and most importantly keeps the force applied while the weld cools. The continuation of the electrode force keeps the weld intact until cooling is achieved; this allows for the maximum strength to be reached. [48]

2.3.2 Welding Process and Parameters

Throughout the study, the force applied for each sample was approximately 1,000 lb_f (4.45 kN) for both rod and coupon configurations. What changed was the current applied and the amount of time applied. Some samples had a 'single-pass' approach, which involved passing high current without passing a 'preheat' current, typically a much lower percentage, followed by a 'tempering' current after the main pass of current. This process can be shown in Figure 2.6, which shows a 'multi-pass' approach, as a schedule of the joining profile.

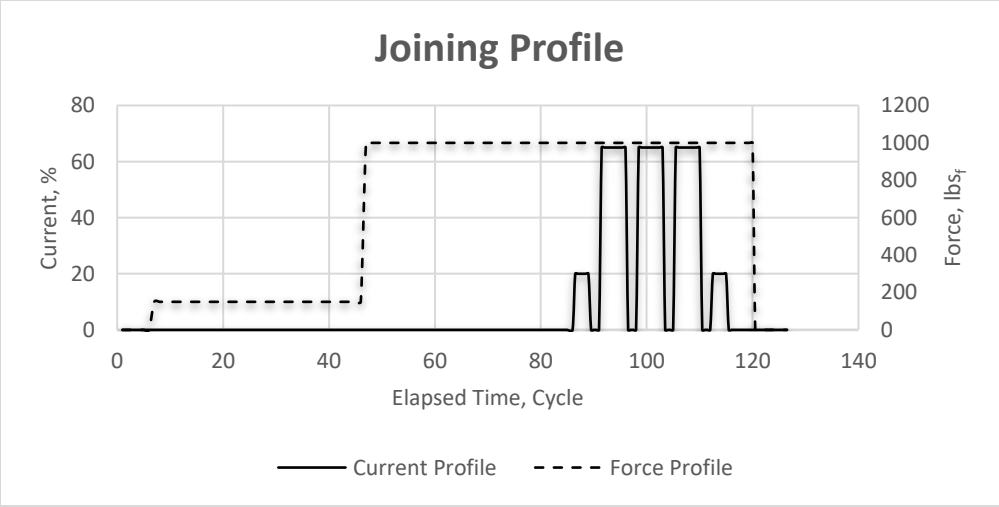

Figure 2.6: Graphical representation of a typical joining schedule used for the tungsten test sample. note: 1 cycle = 16.67 msec (Courtesy: Nathan Jerred).

Based on research done on pressure resistance welding of tungsten [47], similar operating parameters were chosen and adjusted due to molybdenum's lower melting point than tungsten. The PRW operating parameters for the pure molybdenum rods are shown in Table 2.2. Samples without adequate uniaxial force applied resulted in poor welds. The expulsion region expels unwanted oxides and impurities from the interface of the joining samples. Since sample 2 and 4 resulted in faulty welds, only samples 1 and 3 were characterized.

Table 2.2: PRW operating parameters for pure molybdenum rods.

Sample No.	Force	Applied Current Schedule [Current(A) - Time – Impulse(s)]
1 & 3	1,000 lb_f (4,448 N)	20% - 3 cycles - 1 impulse
		55% - 5 cycles - 3 impulses
		20% - 3 cycles - 1 impulse
2 & 4	150 lb_f (667 N)	20% - 3 cycles - 1 impulse
		55% - 5 cycles - 3 impulses
		20% - 3 cycles - 1 impulse

The PRW operating parameters for each coupon weld is shown in Table 2.3, a full table of measured current and voltage can be found in Appendix C. Force was kept at 1,000 lb_f (4.45

Table 2.3: Welding parameters of pure Mo, TZM, Mo-La coupons.

Sample No.	Force	Applied Current Schedule [Current(A) - Time – Impulse(s)]	Calculated Total Energy $H = I^2 \cdot R \cdot t$ [J]
1	1,000lb_f (4,448 N)	65% -3 cycles -1 impulse	Mo: 1,835.9 TZM: 1,818.5 Mo-La: 1,570.1
2	1,000 lb_f (4,448 N)	20% - 2 cycles - 1 impulse 35% - 5 cycles - 3 impulses 20% - 2 cycles - 1 impulse	Mo: 2,472.3 TZM: 2,483.2 Mo-La: 2,476.0
3	1,000 lb_f (4,448 N)	20% - 2 cycles - 1 impulse 45% - 5 cycles - 3 impulses 20% - 2 cycles - 1 impulse	Mo: 3,964.3 TZM: 4,048.5 Mo-La: 4,027.0

kN) for each weld due to the research done earlier with PRW of molybdenum rods. Three different welding schedules were chosen to see how different welding times and currents applied would affect the quality of the weld and its effect on the grain morphology and hardness.

2.3.2.1 PRW of Molybdenum Rods

For this study, only pure molybdenum rods were created to test how a rod configuration would work. For a rod configuration the PRW uses different electrodes to clamp down on the cylindrical pieces, this set up is shown in Figure 2.7. Prior to welding, an alignment check is performed to ensure a sound joint. This alignment can be seen in Figure 2.8.

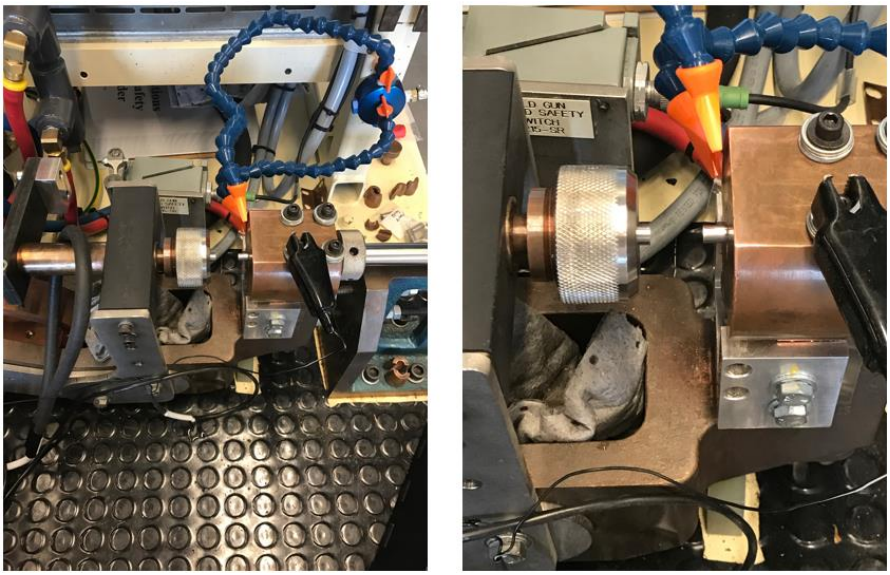

Figure 2.7: Weldments placed within electrodes prior to rod joining.

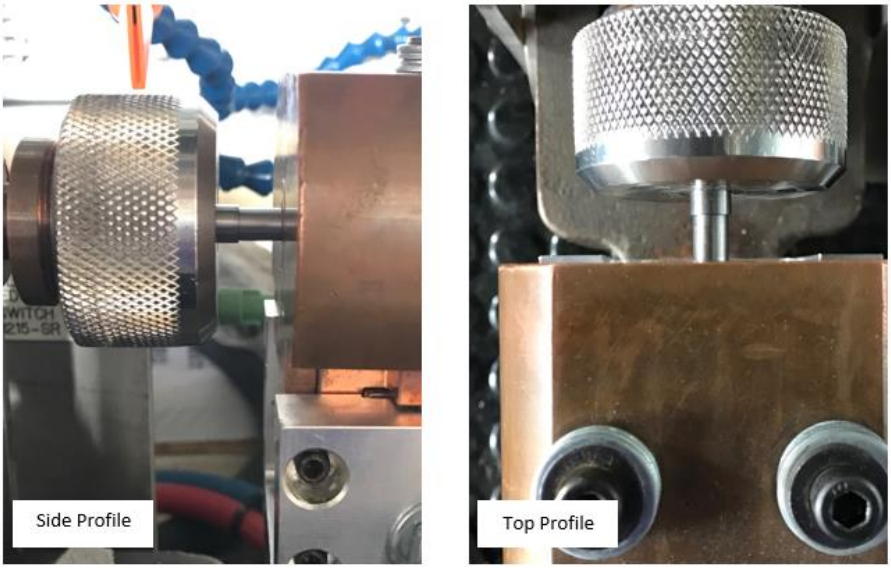

Figure 2.8: Alignment between rod weldments is checked.

As shown previously in Figure 2.6, the joining profile was represented for a tungsten rod sample. The highest amperage applied was 65% and was selected based on the prior research done by Nathan Jerred [46, 47]. Based on the results of the tungsten joining, the parameters for joining molybdenum were adjusted slightly due to the less melting temperature of molybdenum compared to tungsten. The number of heating cycles used for the 'preheat' and 'temper' sections were decreased from 5 cycles to 3 cycles. Also, the current setting was decreased from 65% to 55%. A cycle represents time and the equipment operates at 60 Hz [cycles/sec], thus 1 cycle = 16.67 msec. The full joining schedule of both the tungsten test sample and molybdenum sample can be found in Appendix B. [49]

Examples of the welded samples are shown in Figure 2.9, which shows when force is applied to create an expulsion region and when force is not applied. Welds with an expulsion region exhibit a much stronger metallurgical bond than welds without an expulsion region.

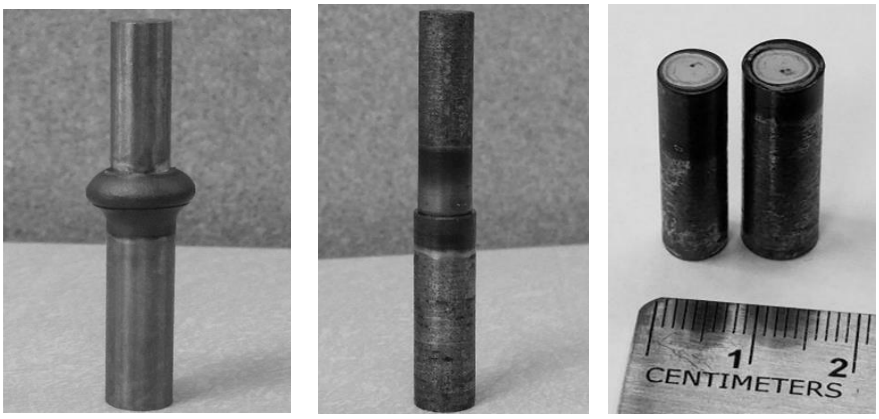

(a) (b) (c)

Figure 2.9: Welded molybdenum rod images: (a) expulsion region (b) no expulsion region (c) no expulsion region, post weld interface.

2.3.2.2 PRW of Molybdenum Coupons

For this study, pure molybdenum, TZM, and Mo-La were used in creating coupon welds. Only similar materials were welded together, i.e. Mo to Mo, TZM to TZM, and Mo-La to Mo-La. All the samples had dimensions as shown in Figure 2.2 and were within the margin of error. The coupon weld parameters were similar to that of the rod weld parameters; however, the PRW machine had different electrode components to handle the rectangular pieces. This is shown in Figure 2.10.

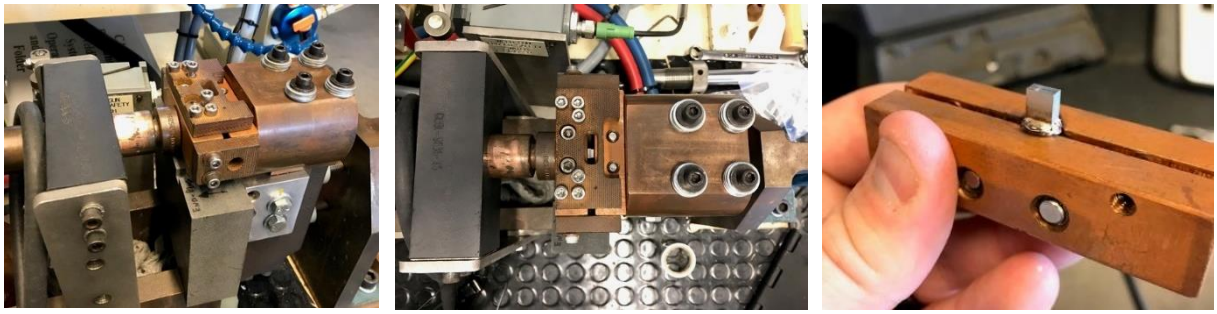

(a) *(b)* *(c)*

Figure 2.10: PRW setup for welding coupons; (a) PRW set up (b) coupon alignment check (c) post weld of coupon left in copper electrode.

2.4 Preparing Welded Samples for Metallographic Characterization

The as-received samples, those from the pure molybdenum rod and the plates of Mo, TZM, and Mo-La, and the post-welded sample were characterized using various characterization tools. Prior to microstructural characterization, all the samples were prepared by cutting, mounting, grinding and polishing, and then chemically etched. Prior to these steps, the expulsion region of the welded samples was partially removed by a grinding belt to ensure a sound cut could be performed. The removal of the expulsion region can be seen in Figure 2.11. The next few sections cover the mounting, grinding and polishing, and etching processes in more detail.

(a) (b)

Figure 2.11: Removing expulsion region for cutting welded specimens, (a) prior to removing expulsion region (b) after removal of expulsion region.

2.4.1 Cutting Welded Samples

For both rod and coupon welded samples, a perpendicular cut to the weld interface was performed using a Buehler Isomet 1000 precision diamond blade saw with water-based lubricant. The weld cut is shown in Figure 2.12. After cutting the samples, light grinding (240 grit SiC paper) was conducted to remove any problems arising out of non-level sample surfaces during mounting.

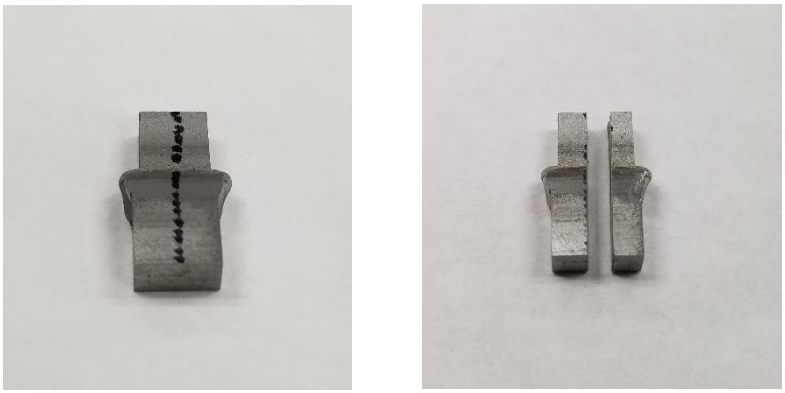

Figure 2.12: Precision cut of welded molybdenum sample after partial removal of expulsion region.

2.4.2 Mounting

Throughout this thesis work, two different mounting materials and techniques were used. The original mounting technique was hot mounting using black phenolic mounting material in a Pace Technologies Terapress hot mounting machine. The hot mount heated up to 170 °C and held for 10 min under 85 psi of pressure. However, this technique was quickly replaced due to long grinding & polishing times along with erosion of the mounting material during etching. This erosion resulted in deposition of the mounting material onto the weld sample leaving behind a stained surface.

Cold mounting with acrylic became the preferred mounting technique because of the reduced grinding & polishing time and the lack of erosion of the mounting material from the chemical etchant. Acrylic powder and acrylic liquid, from Allied High Tech Products, Inc., with a 2:1 (by volume) powder to liquid ratio was used. Cure time was approximately 15 minutes.

2.4.3 Grinding, Polishing, and Etching

After mounting the samples, the mounted sample surface was ground using 120, 240, 400, 600, 800, and 1200 grit SiC paper on an Allied Twinprep 3 grinding/polishing machine. Each stage of the grinding process would remove the scratches induced from the previous stage by rotating the sample surface perpendicular to the grinding direction. Once grinding was complete with the 1200 grit SiC paper, polishing the samples on a cloth polishing pad was conducted. For polishing, 1 µm alumina with 3 µm suspended diamond particles was used as the first stage followed by 1 µm alumina with 1 µm suspended diamond particles. The last stage of polishing was 0.3 µm alumina with 0.1 µm suspended diamond particles.

After polishing, the samples were cleaned with deionized water and soap to remove any impurities. After air drying, the samples were etched using Murakami's etchant, a composition found in Table 2.4. The etching time was ~1 min and was done by pipetting the etchant unto the surface of the sample and swabbing with cotton. The etchant was removed with 3% hydrogen peroxide and cleaned with methanol.

Table 2.4: Murakami's chemical etchant composition. [50]

$K_3Fe(CN)_6$	10 g
KOH	10 g
H_2O	100 ml

2.5 Microstructural Characterization

2.5.1 Optical Microscopy

Microstructural characterization was performed on the as-received molybdenum alloys as well as the post welded specimens. Most of the microstructural images were taken by using an Olympus PMG-3 optical microscope. The as-received metallographic samples of pure molybdenum, TZM, and Mo-La were imaged at various magnifications to capture the grain structure.

The 3-D orientation of the as-received rolled plates are shown in Figure 2.13 along with how the coupon weldments are orientated. The grain orientation is defined as follows: L is

longitudinal direction (rolling direction), LT is long transverse direction, and ST is the short transverse (i.e. through-thickness) direction, as shown in Figure 2.13. After welding, the samples were imaged to show the change in the grain morphology along the welded specimen.

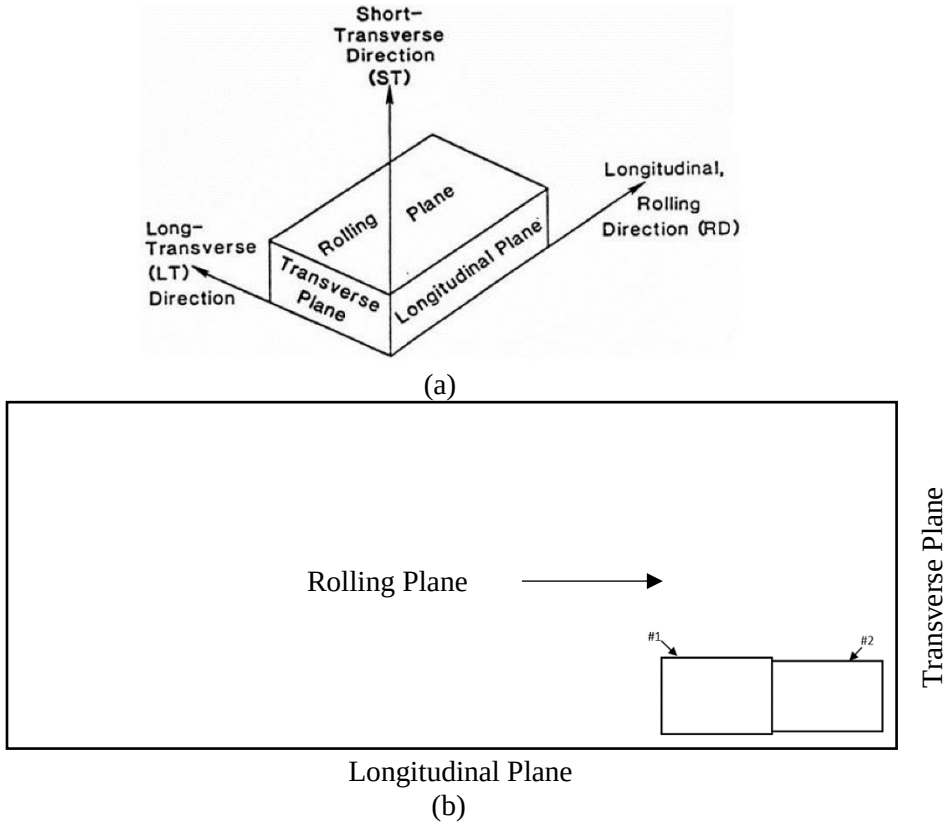

Figure 2.13: 3-D AR plate orientation and coupon weldment grain orientation (a) the 3-D reference frame of direction. (b) Reference frame with respect to geometry of the as-received plate along with a view of the coupon joint configuration (top view, not to scale).

2.5.2 Scanning Electron Microscopy

A LEO Supra 35 VP scanning electron microscope (SEM) was used to show the microhardness indents by secondary electron imaging. An accelerating voltage of 5 kV was used in capturing the Vickers microhardness indentations to reveal more of the contours left behind from the indents. Electron backscatter diffraction (EBSD) was used to reveal topographical information of the material surface, visualizing the grain structure as well as the grain orientation and grain angle of as-received and post welded samples. Samples were placed on carbon tape to assist with holding samples and improving conductivity of samples to prevent electrode charge build-up. An accelerating voltage of 15 kV was used for a wide range of magnifications.

2.5.3 Transmission Electron Microscopy

Transmission electron microscopy (TEM), a JEOL 2010J, was used at an accelerating voltage of 200 kV for chemical microanalysis of precipitates via EDX, and other fine-scale microstructural analysis. As-received samples of pure molybdenum, TZM, and Mo-La in the long transverse direction were characterized along with welded samples of the same alloys.

For TEM and EBSD sample preparation, samples were ground down and polished to ~200 μm in thickness. Discs with 3 mm diameter were punched out and further thinned down in a Fischione instruments Twin-jet electropolisher model 110. The chemical etchant used was 13% sulfuric acid solution to 87% methanol, by volume. Dry ice was used to lower the temperature of the mixture to -40 ^{o}C to reduce the evaporation of the sulfuric acid solution during electropolishing. The samples were jet polished until a small hole formed; the samples were then characterized soon thereafter to reduce oxide formation on the surface of the samples. A PIPS II model 695 argon ion mill was used to further thin and remove any contaminants from the sample surface.

2.6 Mechanical Characterization

Mechanical characterization was used to understand the strength molybdenum alloys prior to welding and post welding. In this study, mechanical characterization was performed using Vickers micro-indentation analysis on molybdenum alloys before and after welding. Micro-tensile analysis was used on post welded specimens which was used to produce micro-indentation hardness profile. Hardness is generally considered roughly proportional to strength.

2.6.1 Micro-Indentation Analysis

In this study, a LECO LM100 Vickers microhardness tester was used to conduct hardness analysis for as-received samples and for post-welded samples. Figure 2.14 shows a diagram of the tip of a Vickers microhardness tester, which is a diamond pyramid. The equation for hardness is shown below as Equation 2. For as-received samples, each grain orientation had several indents taken to produce an average hardness. Each indent had 500 g_f applied and resulted in typical pyramidal diagonals with a maximum of 65 μm (0.00255 inch).

where VHN is Vickers hardness number, L is $(d_1 + d_2)/2$ in mm, and F is force in kg_f.

$$VHN = 1.854^* (F) / (L^2) \quad (2)$$

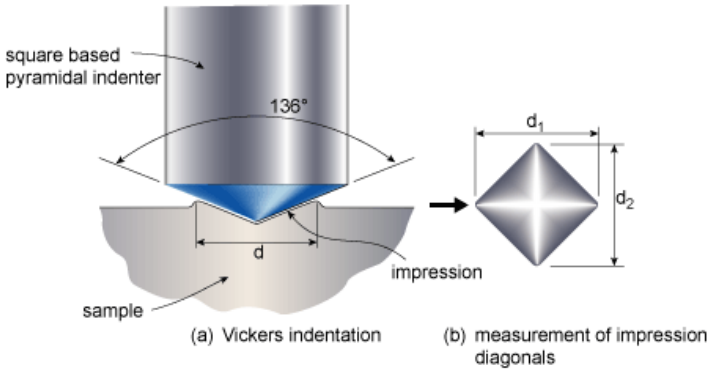

Figure 2.14: Schematic of Vickers microhardness indentation. *Source www.twi-global.com*

For microhardness along the welded samples, an indent was taken every 0.025 inches along the weld samples as shown in Figure 2.15, this spacing satisfies the minimum standard of 2.5 times the diagonal of the indents, to prevent interference of other indents. Additionally, each welded sample had three rows of indents taken to analyze the strength of the material towards the edges and the middle, which is shown in Figure 2.15 as well. Each row typically had 20 indents taken along the entire welded sample.

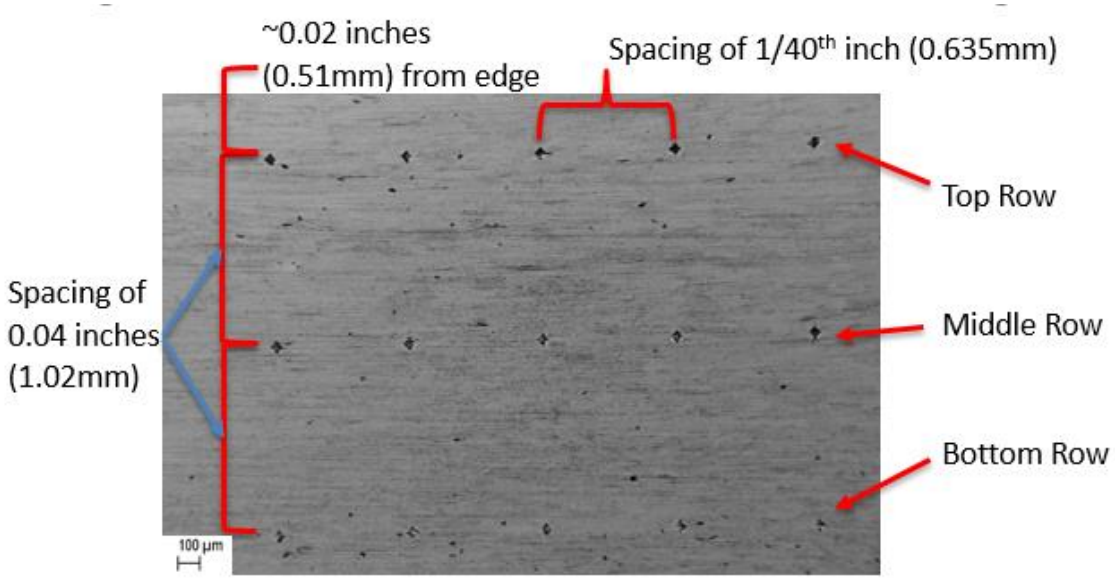

Figure 2.15: Scanning electron microscope image of Vickers hardness indents along Mo-La sample 2.

3.0 Results

3.1 Molybdenum Rod Configuration

The purpose of the molybdenum rod configuration was to determine the importance of applying uniaxial force and if the pressure resistance welding technique can create sound welds. These were the first welds produced in this study and became a stepping stone for further weld experiments.

3.1.1 As-Received Material Characterization

Optical microscopy, scanning electron microscopy, and Vickers hardness testing were used to characterize as-received pure molybdenum rod samples used for welding. Figure 3.1 shows the pure molybdenum rod microstructure via optical microscopy. The grains appear as elongated in the longitudinal section whereas the grains show near-equiaxed grain morphology in the transverse section. The grain morphology observed resembles that of a typical extruded rod microstructure. The geometric mean grain size of 126±7 μm in the longitudinal direction and 50±4 μm in the transverse direction were measured.

(a) **(b)**

Figure 3.1: As-received microstructure of molybdenum rod (a) longitudinal (b) transverse sections.

The chemical composition of the pure molybdenum rod was analyzed using energy-dispersive X-ray spectroscopy (EDX) available a scanning electron microscope. Figure 3.2 shows a representative EDX spectrum which showed only molybdenum peaks. It was not possible to

detect a low amount of carbon in the EDX due to the low resolution of this technique toward light elements.

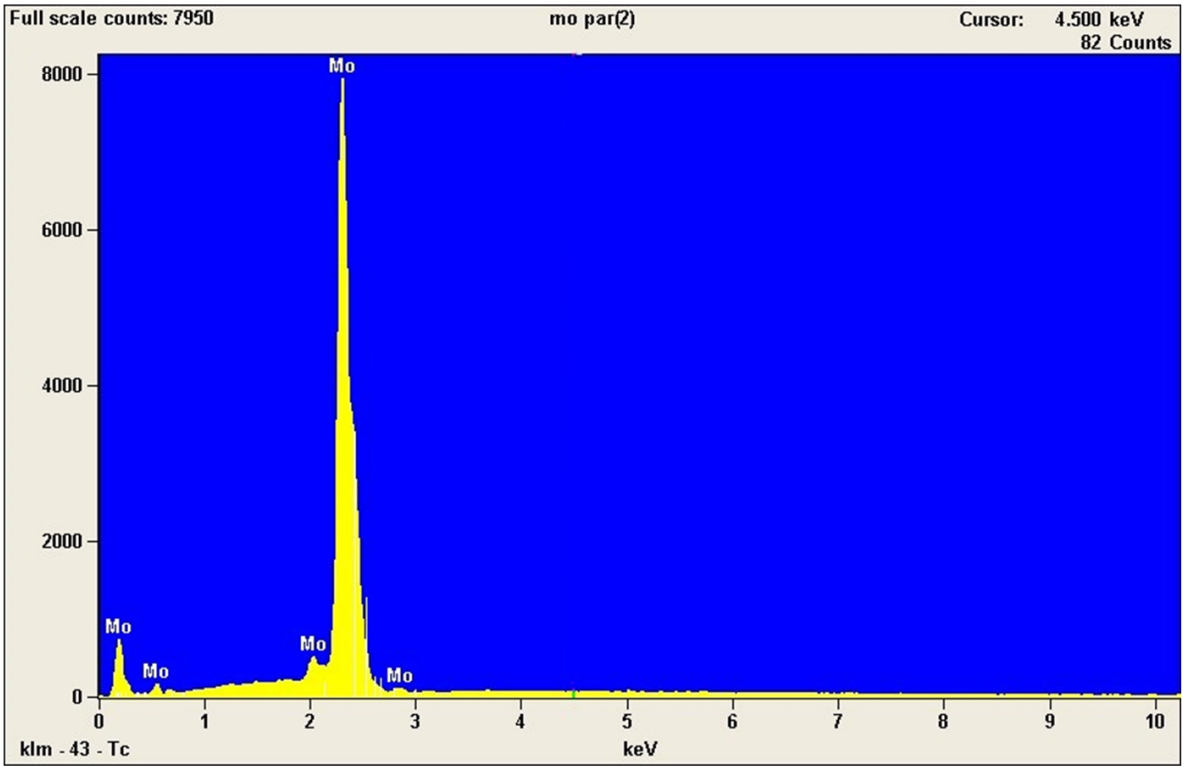

Quantitative Results for: mo

Element Line	Net Counts	Net Counts Error	Weight %	Weight % Error	Atom %	Atom % Error
Mo L	129735	+/- 1584	100.00	+/- 0.61	100.00	+/- 1.22
Total			100.00		100.00	

Figure 3.2: Energy-dispersive X-ray spectroscopy spectrum of pure molybdenum rod.

Vickers microhardness was performed on the as-received molybdenum rod, 6 indents were taken with 500 g_f, which produced an average Vickers hardness number (VHN) of 230±8 for the transverse surface and 233±8 for the longitudinal section.

3.1.2 Optical Microscopy

Optical microstructure in Figure 3.3 shows the change along the weld zone from elongated grains, base material, to equiaxed recrystallized grains at the middle of the weld zone.

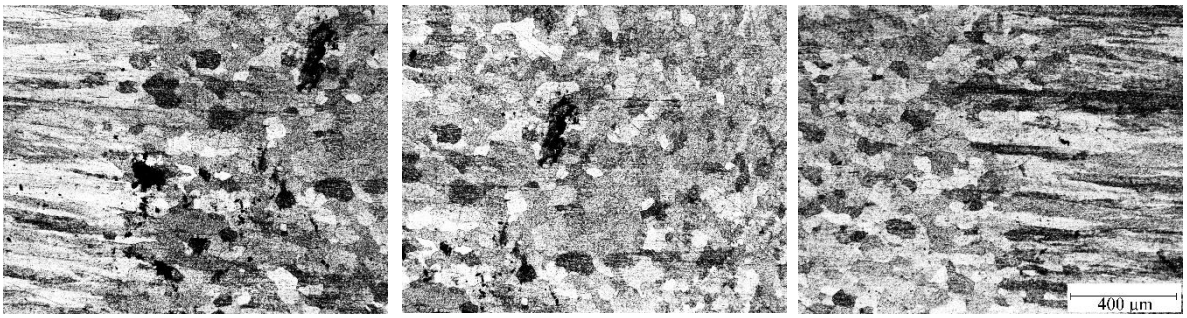

Figure 3.3: Optical images across the weld zone of pure molybdenum rod sample 3. Images taken at 50X magnification. (a) left transition from the parent material into the weld zone, (b) middle of the weld and, (c) right transition from the weld zone to the base material.

3.1.3 Vickers Microhardness Analysis

Vickers microhardness testing was performed on sample 3 and resulted in a hardness profile shown in Figure 3.4. From Figure 3.4, the average hardness, VHN, in the base material was measured to be 242±10, while the lowest hardness recorded in the weld zone was 199±1, a 16.6% decrease. From the hardness profile, the curve is mostly smooth and only one dip is present, indicating a lack of both TMAZ and HAZ zone. If both were present, more peaks and valleys in the hardness profile would be present. This may be due to the very short weld times and lack of melting of the molybdenum during welding.

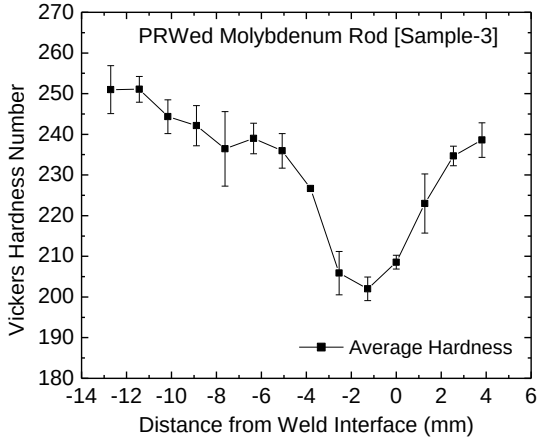

Figure 3.4: Microhardness profile of molybdenum rod, Sample-3.

3.2 Molybdenum Coupon Configuration

From the research conducted with pure molybdenum rod, adjusting the applied current schedule to molybdenum coupons became the next progression of the research. For the coupon configuration, 3 molybdenum alloys were welded and characterized, pure molybdenum, TZM, and Mo-La.

3.2.1 As-Received Material Characterization

The as-received plates of pure molybdenum, TZM, and Mo-La were characterized prior to welding. Optical microscopy and Vickers micro-indentation was performed on the plates. The orientation of interest for the coupon configuration was the longitudinal cross section, Figure 3.5. The grain sizes for as-received plates are shown in Table 3.1.

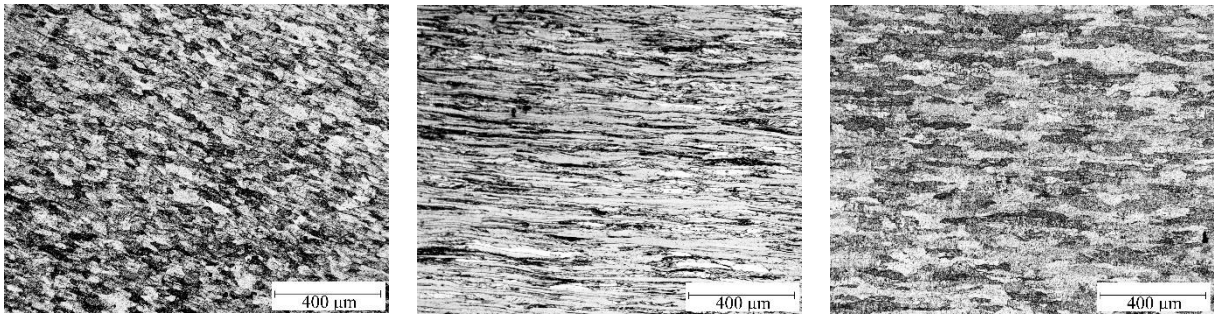

(a) (b) (c)

Figure 3.5: Optical micrographs of the as-received plates in the longitudinal cross section (all images are taken at 50X): (a) pure Mo (b) TZM (c) Mo-La.

According to H.C. Starck (the manufacturer of the plates), Mo-La is processed at a higher temperature than other molybdenum based materials in order to anneal out dislocations. It is likely the reason for Mo-La having a much higher average grain size and lower hardness.

Table 3.1: Average grain size and Vickers microhardness of AR molybdenum alloys.

Alloys	Orientation	Ave. Grain Size (µm)	Aspect Ratio	VHN
Pure Mo	L	32±15	2.1	251±13
TZM	L	43±17	9.8	279±15
Mo-La	L	55±10	3.4	203±4

TEM was performed on the as-received plates to study fine microstructural details such as dislocations configurations, presence of precipitates, and grain boundaries. This information would be used to compare the changes in the as-received microstructure to the post-welded material. Figures 3.6(a) and (b) show bright field TEM images of pure molybdenum, with dislocation tangles and forming some form of cells as well. Given that the mean grain size measured by optical microscopy is 32 μm, the features seen present within the elongated grains. Figures 3.6(c) and (d) show the fine scale microstructural details with the dislocation substructures consisting of dislocation tangles, Ti and Zr carbides in grain, and cell structures. In TEM, it is not possible to view the whole grains as the mean grain size of the as received TZM is 43 μm.

Figures 3.6(e) and (f) are the TEM bright field images showing the microstructural details of the as received Mo-La plate. Mo-La did not show the type of dislocation configurations seen in as received Mo and TZM, which is likely related to the result of the heat treatment applied to the material by the manufacturer (H.C. Starck). The TEM image in Figure 3.6(f) show spheroidal lanthanum oxide particles. The typical particle size is fine, mean dimeter being 50 nm.

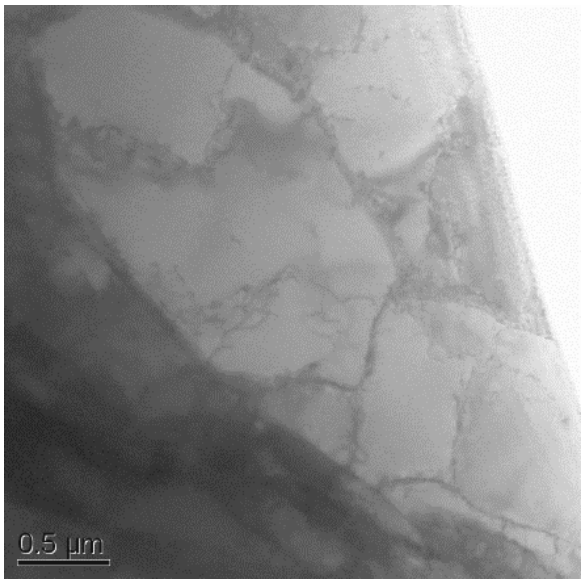

(a)

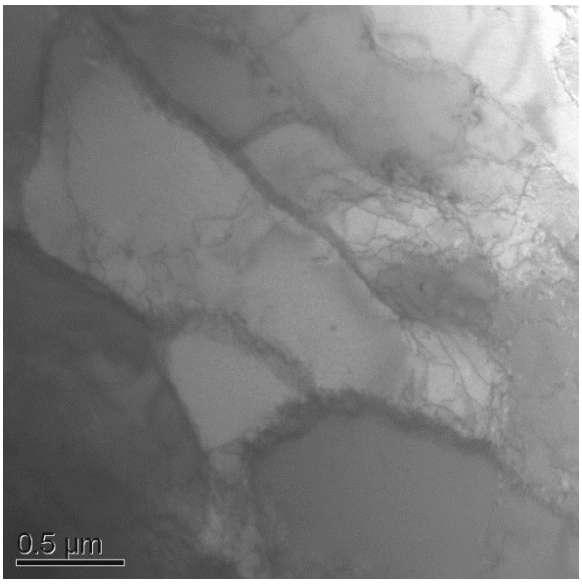

(b)

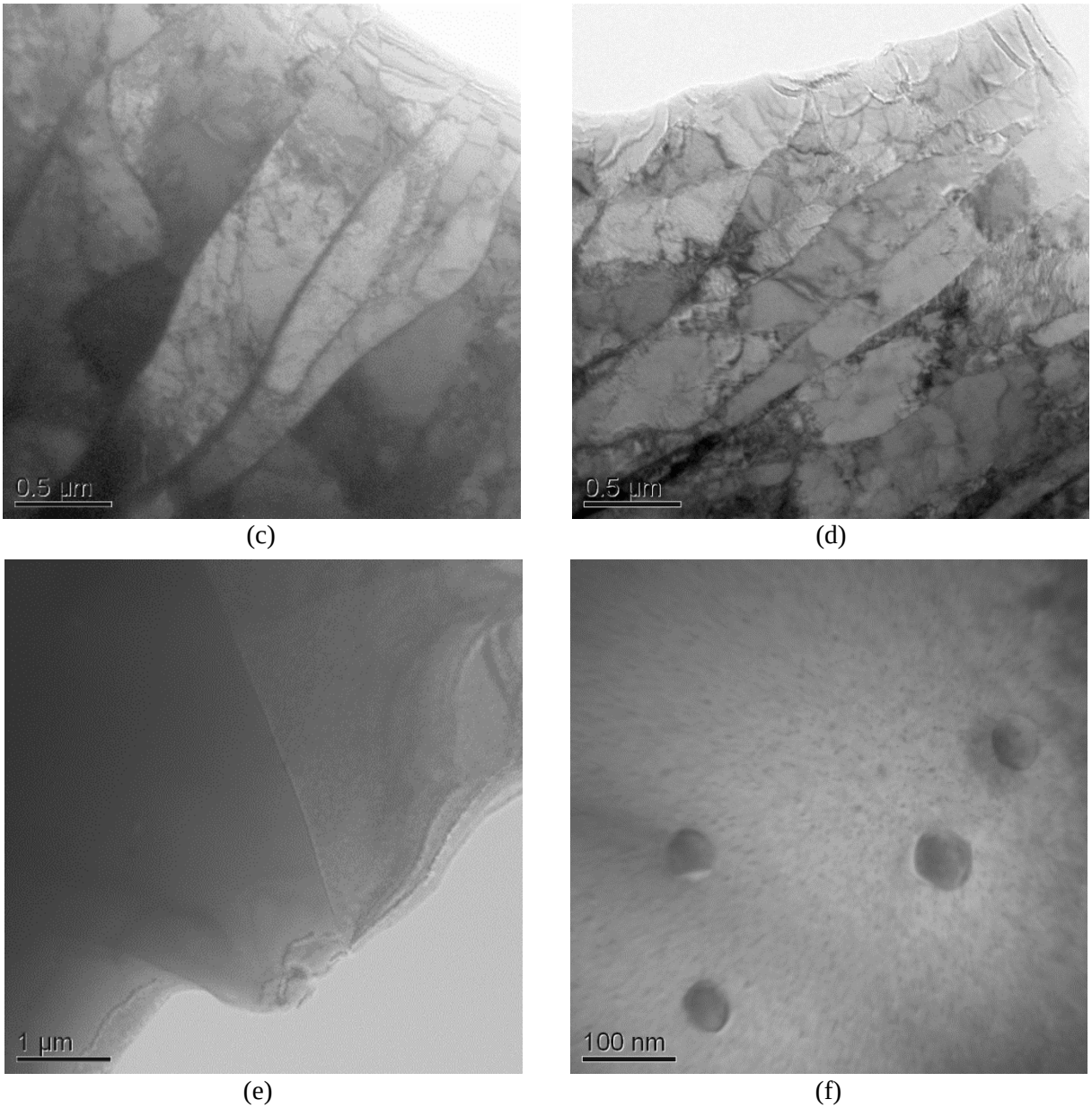

(c) (d)

(e) (f)

Figure 3.6: TEM images of as-received plates in the longitudinal cross section (a, b) pure Mo, (c, d) TZM, and (e, f) Mo-La.

3.2.2 Characterization of PRWed Pure Molybdenum

3.2.2.1 Optical Microscopy

As shown in Figures 3.7-3.9, the grain morphology of PRWed samples of pure molybdenum changed quite significantly across the weld zone. As revealed by optical microscopy, the base material of the welded samples appears to be similar to the as-received material microstructure.

Figures 3.7-3.9 show the microstructure of the welded samples with some of the base material present in the transition images as well as showing the center of the weld zone.

The transition region from the base material to the weld zone shows a drastic shift in microstructure from the elongated grains to small equiaxed grains. Because of the concurrent heating and extensive plastic deformation, the weld zone undergone dynamic recrystallization as can be shown in optical images of Figures 3.7-3.9 (b). The center of the weld zone exhibited the largest grains, the average grain size of the weld zone and base material from each PRWed pure molybdenum sample is listed in Table 3.2.

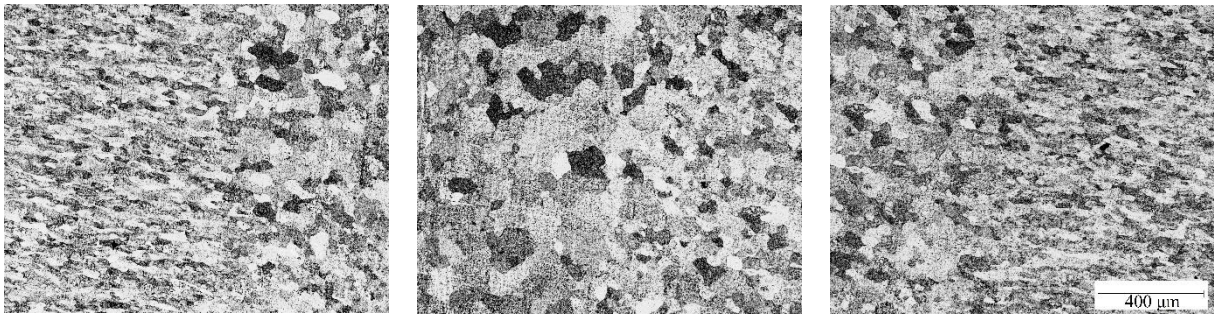

(a) **(b)** **(c)**

Figure 3.7: Optical images across the weld zone of pure Mo, Sample-1. Images taken at 50X magnification. (a) Left transition from the parent material to the weld zone, (b) middle of the weld, and (c) transition on the right from the weld zone to the parent material.

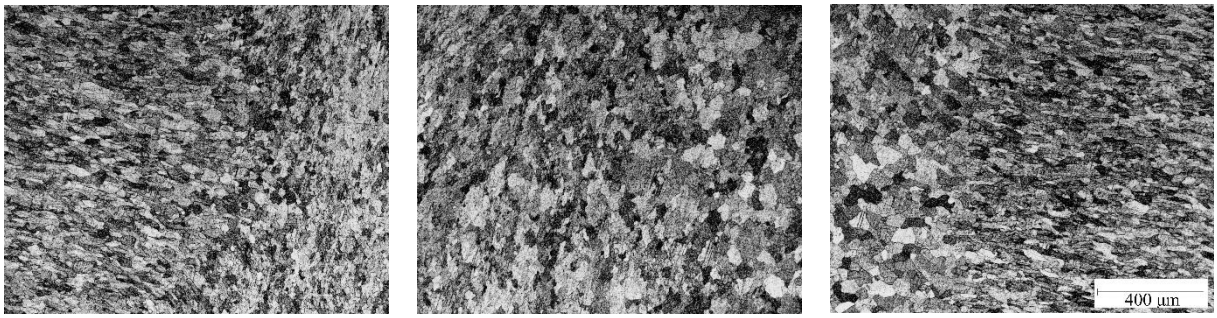

(a) **(b)** **(c)**

Figure 3.8: Optical images across the weld zone of pure Mo, Sample-2. Images taken at 50X magnification. (a) Left transition from the parent material to the weld zone, (b) middle of the weld, and (c) transition on the right from the weld zone to the parent material.

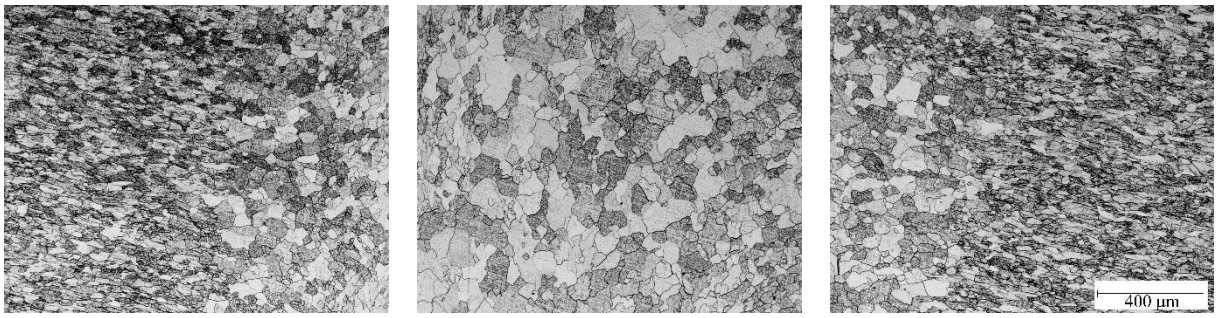

(a) **(b)** **(c)**

Figure 3.9: Optical images across the weld zone of pure Mo, Sample-3. Images taken at 50X magnification. (a) Left transition from the parent material to the weld zone, (b) middle of the weld, and (c) transition on the right from the weld zone to the parent material.

Table 3.2: Grain sizes in PRWed pure molybdenum samples.

Sample No.	Base Material (µm)	Weld Zone (µm)
1	33±6	62±9
2	35±5	43±4
3	32±3	49±6

3.2.2.2 Vickers Microhardness Analysis

Vickers microhardness testing was used to create microhardness profile of the three pure molybdenum coupons, as depicted in Figure 3.10. From the hardness profile, all three showed a decrease in hardness throughout the weld region, which is the TMAZ zone. Sample-1 had an average Vickers hardness number (VHN) of 252±15 for the base material and a low of 203±3 VHN in the weld zone, resulting in a decrease of 19%. Sample-2 had an average VHN of 251±21 for the base material and a low of 209±3 VHN, resulting in a decrease of 17%. Sample-3 had an average VHN of 253±15 for the base material and a low of 202±4 VHN in the weld zone, resulting in a decrease of 20%. The TMAZ width can be measured based on the hardness profile and the change shown in the optical microstructure. For Sample-1, the TMAZ was ~4.5 mm, Sample-2 was ~6.0 mm, and Sample-3 was ~4.5 mm. From the hardness profiles, the HAZ was minimal if non-existent entirely.

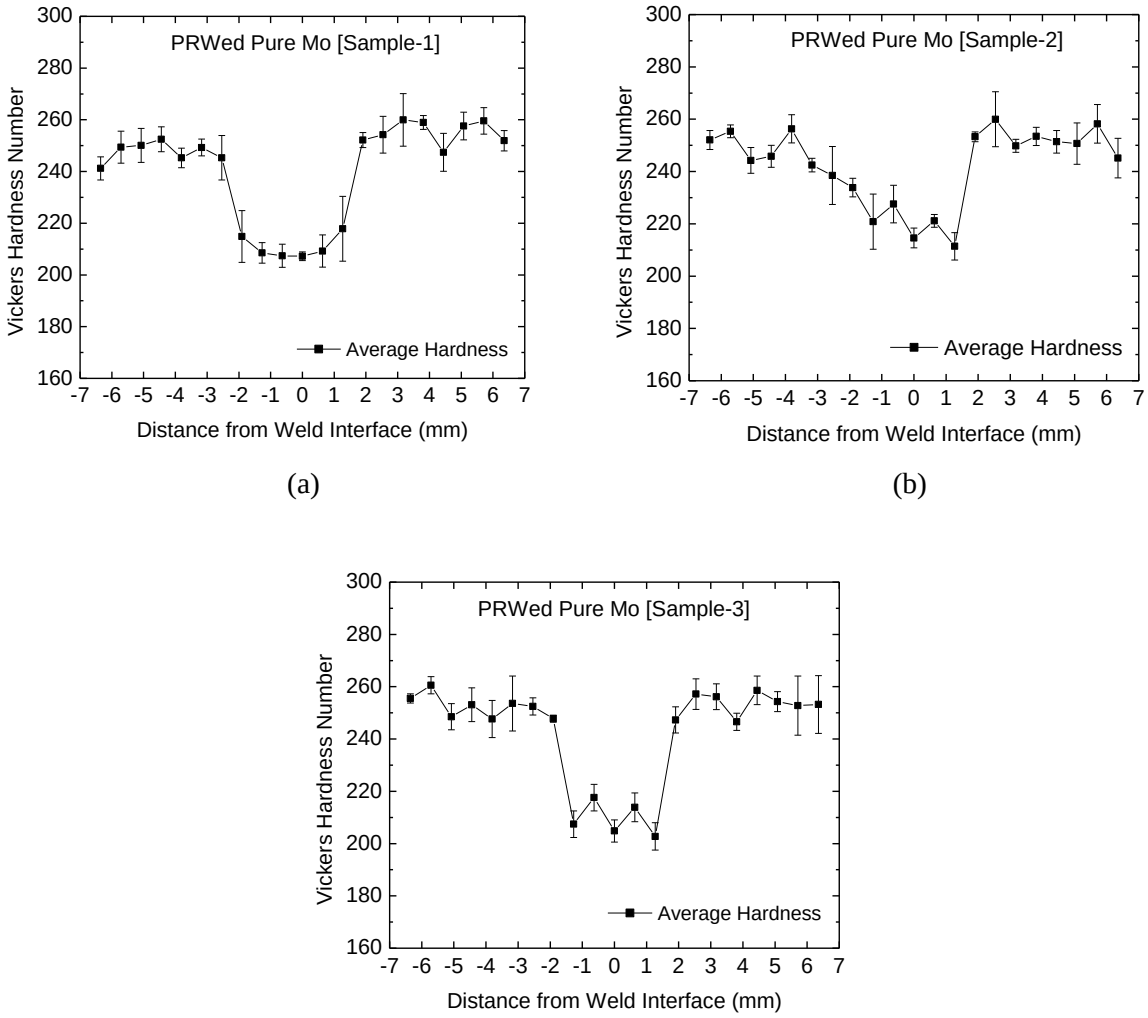

Figure 3.10: Microhardness profiles of pure Mo coupons (a) Sample-1 (b) Sample-2 (c) Sample-3.

3.2.2.3 Transmission Electron Microscopy Results

Transmission electron microscope (TEM) was used to capture microstructural information for PRWed pure molybdenum, as shown in Figure 3.11. TEM images taken of the weld zone of pure molybdenum Sample-1 showed areas of equiaxed subgrains, Figure 3.11(c), with very few dislocations present. In Figure 3.11 (a, b, and d), larger grains with dislocations can be spotted. The combination of recrystallized grains with dislocations is often typical with dynamic recrystallization.

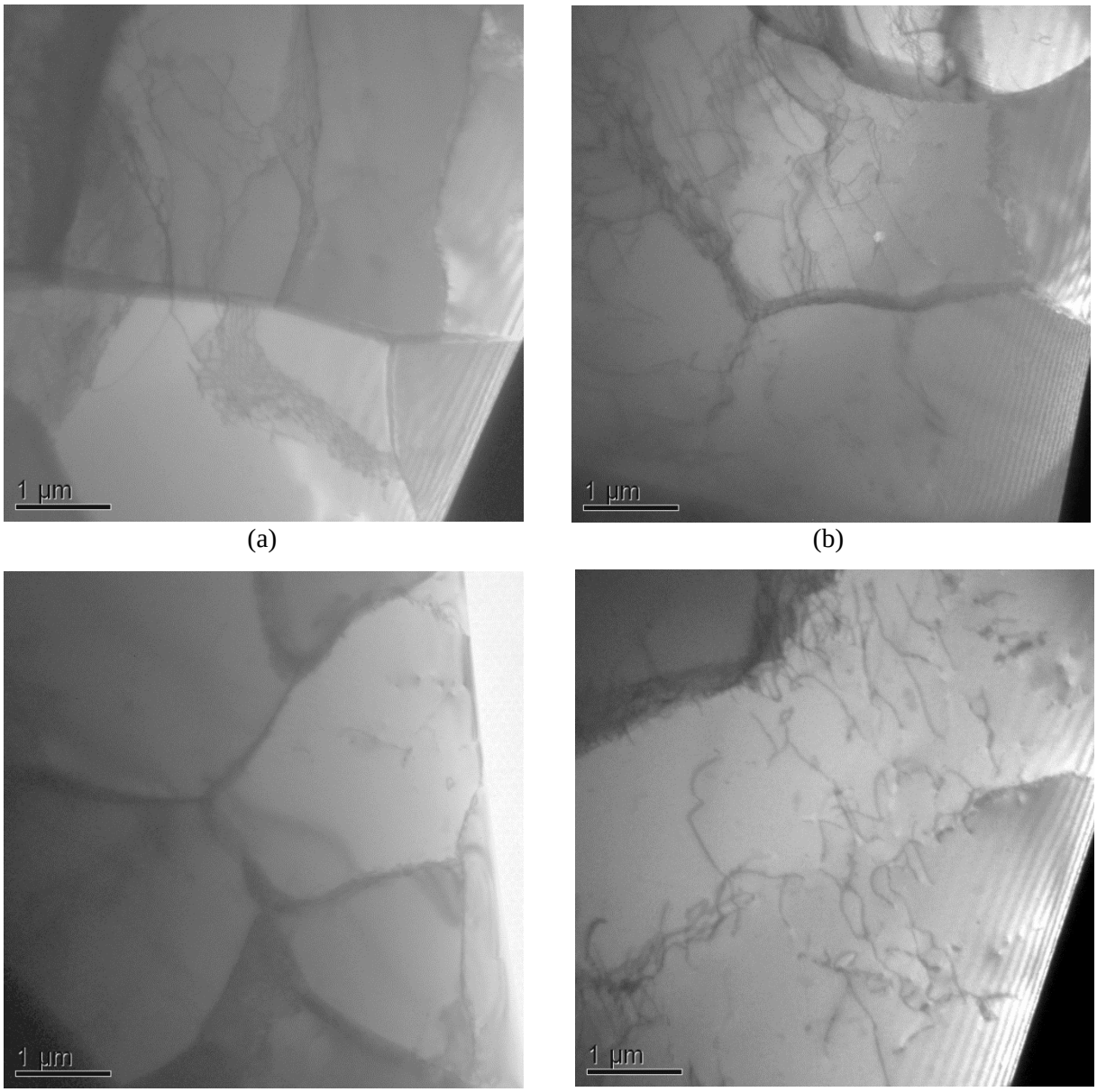

(a) (b)

(c) (d)

Figure 3.11: TEM images of the weld zone of PRWed pure molybdenum Sample-1.

3.2.3 Characterization of PRWed TZM

3.2.3.1 Optical Microscopy

As shown in Figures 3.12-3.14, the grain morphology of PRWed samples of TZM changed throughout the weld zone. The base material of the welded samples appears to be similar to the as-received plate microstructure. Figures 3.12-3.14 show the microstructure of the welded samples with some of the base material present in the transition images as well as showing the center of the weld zone.

The transition region from the base material to the weld zone shows a drastic shift in microstructure from elongated grains to small equiaxed grain. Dynamic recrystallization is apparent in the weld zones as shown in Figures 3.12-3.14 (b). The center of the weld zone exhibited the largest grains, the average grain sizes for the weld zone are listed in Table 3.3.

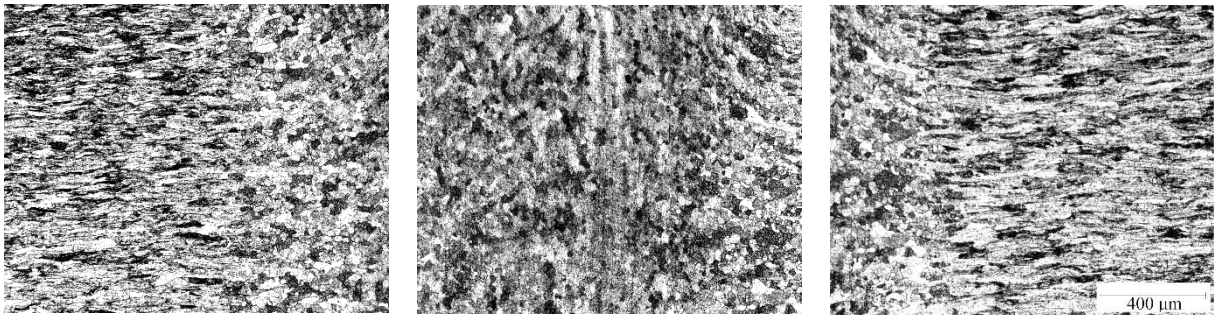

(a) (b) (c)

Figure 3.12: Optical images across the weld zone of TZM, Sample-1 (All images taken at 50X magnification): (a) Left transition from the base material to the weld zone, (b) middle of the weld and, (c) right transition from the weld zone to the base material.

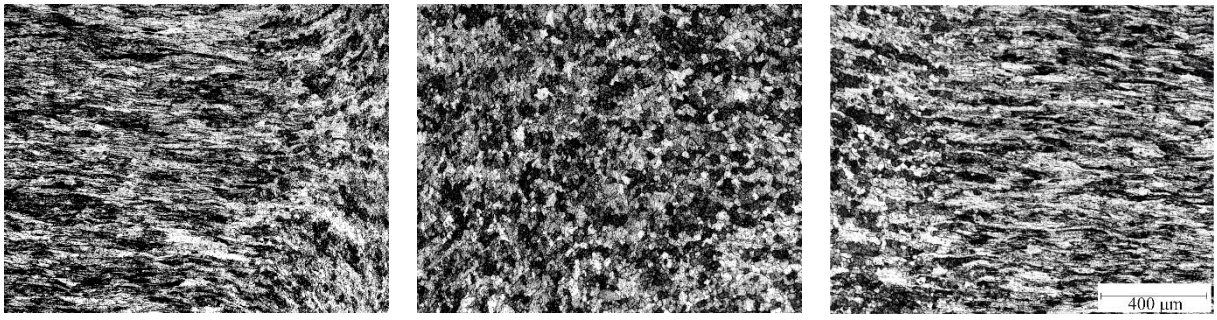

(a) (b) (c)

Figure 3.13: Optical images across the weld zone of TZM, Sample-2 (All images taken at 50X magnification): (a) Left transition from the base material to the weld zone, (b) middle of the weld and, (c) right transition from the weld zone to the base material.

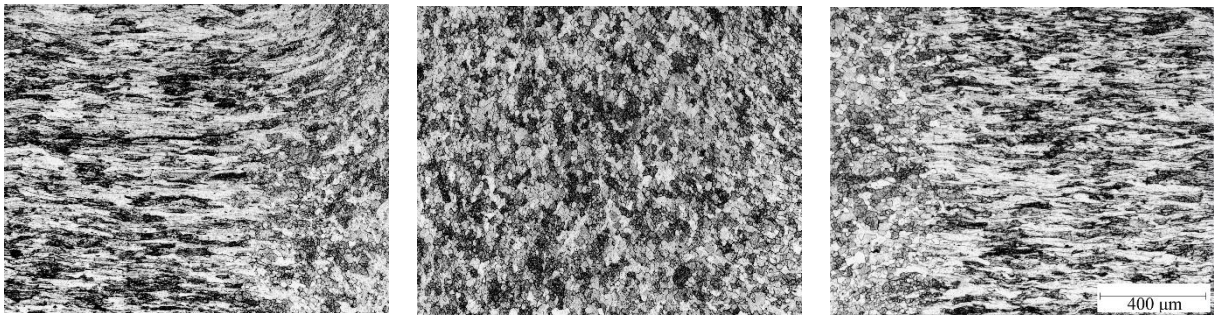

(a) (b) (c)

Figure 3.14: Optical images across the weld zone of TZM, Sample-3 (All images taken at 50X magnification): (a) Left transition from the base material to the weld zone, (b) middle of the weld and, (c) right transition from the weld zone to the base material.

From Figure 3.14(a), a crack was present, this is shown in more detail in Figure 3.15 with a closer look at the crack site. The crack was perpendicular to the weld interface and was ~1 mm in length.

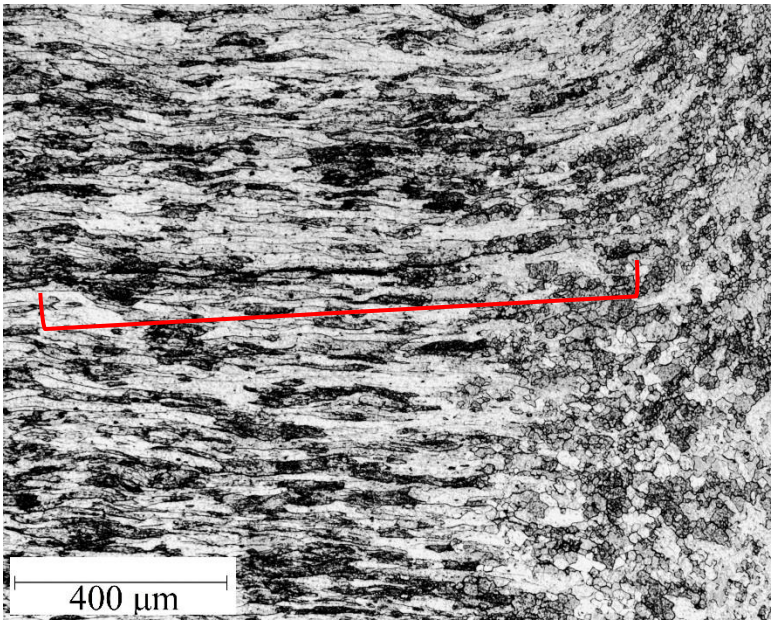

Figure 3.15: Optical image taken at 50X magnification of crack site found on TZM Sample-3.

Table 3.3: Grain sizes of PRWed TZM samples.

Sample No.	Base Material (µm)	Weld Zone (µm)
1	36±15	20±2
2	38±19	23±2
3	40±9	21±2

3.2.3.2 Vickers Microhardness Analysis

Vickers microhardness indentation was used to create microhardness profile of the three TZM coupons, as shown in Figure 3.16. From the hardness profiles, all three showed a decrease in hardness throughout the weld region, which is the TMAZ zone. Sample-1 had an average microhardness of 307±16 VHN for the base material and a low of 245±4 VHN in the weld zone, resulting in a decrease of hardness by about 20%. Sample-2 had an average microhardness of 306±17 VHN for the base material and of 229±11 VHN for the weld zone, resulting in a decrease of about 25%. Sample-3 had an average microhardness of 305±19 VHN for the base material and a low of 238±6 VHN in the weld zone, resulting in a decrease of microhardness by 22%. The TMAZ width can be measured based on the hardness profile and the change shown in the optical microstructure. For Sample-1, the TMAZ was ~4.0 mm, Sample-2 was ~6.0 mm, and Sample-3 was ~4.5 mm. Here also as revealed by the hardness profiles, the HAZ could not be detected to any significant extent if not non-existent entirely.

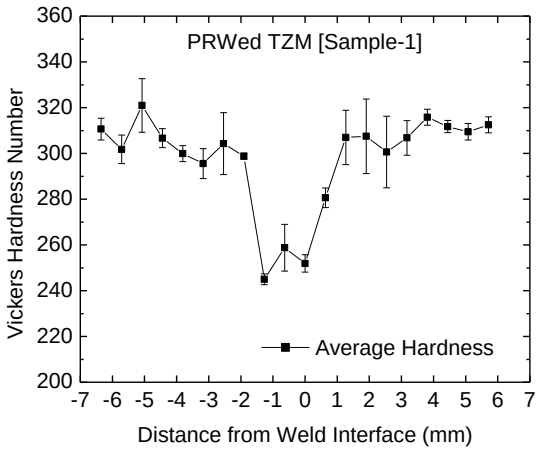

(a)

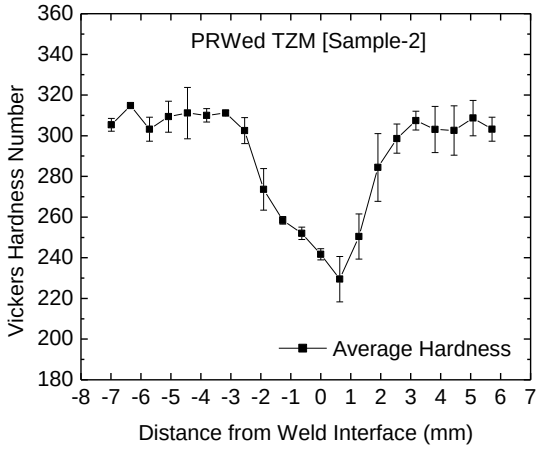

(b)

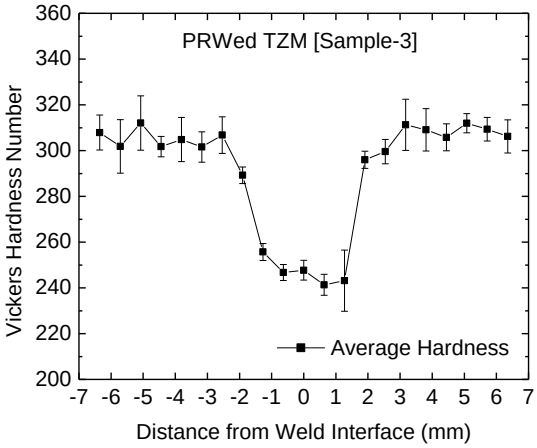

(c)

Figure 3.16: Microhardness profiles of TZM coupons (a) Sample-1 (b) Sample-2 (c) Sample-3.

3.2.3.3 Transmission Electron Microscopy Results

Transmission electron microscope (TEM) images was used to capture microstructural imaging of PRWed TZM Sample-1, as shown in Figure 3.17. TEM images of the weld zone revealed more equiaxed grains with precipitates present. Plenty of dislocation looping is present for most grains observed. It was not clear whether any precipitates segregated to the grain boundaries. The PRW process does occur in less than a second, so diffusion is limited.

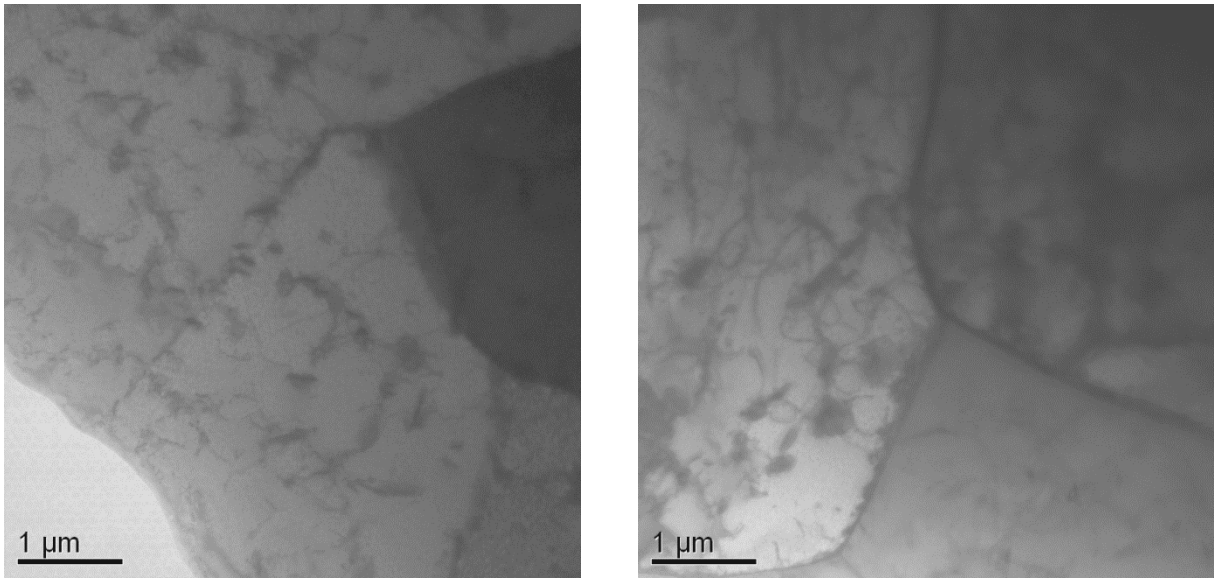

(a) (b)

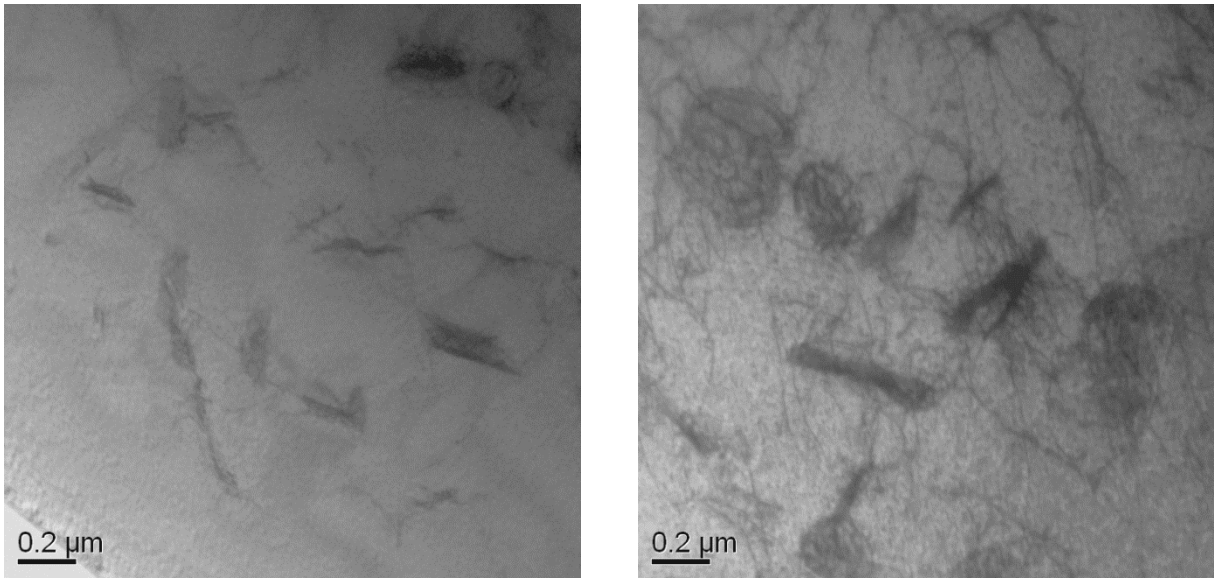

(c) (d)

Figure 3.17: TEM images of the weld zone of PRWed TZM Sample-1.

3.2.4 Characterization of PRWed Mo-La

3.2.4.1 Optical Microscopy

As shown in Figures 3.18-3.20, the grain morphology of PRWed samples of Mo-La hardly changed throughout the weld zone. The base material of the welded samples appears to be similar to the as-received base material microstructure. Figures 3.18-3.20 show the microstructure of the welded samples with some of the base material present in the transition images as well as showing the center of the weld zone. The optical microscopy images showed the flow of material at the interface and a limited amount of dynamic recrystallization throughout most of the weld zone.

While Figures 3.18-3.20 do not clearly show dynamic recrystallization, Figure 3.21 shows a higher magnification of Mo-La Sample-1, in which small recrystallized grains can be observed on the edges of larger grains.

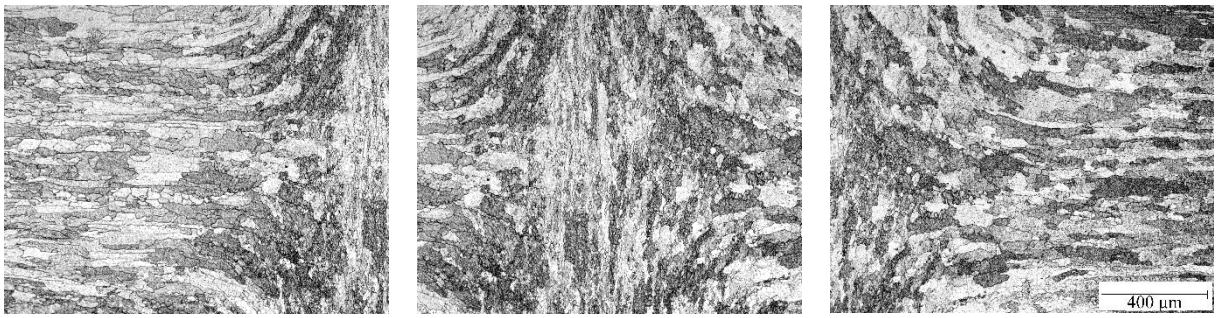

(a) (b) (c)

Figure 3.18: Optical images across the weld zone of Mo-La, Sample-1 (All images taken at 50X magnification): (a) Left transition from the base material to the weld zone, (b) middle of the weld and, (c) right transition from the weld zone to the base material.

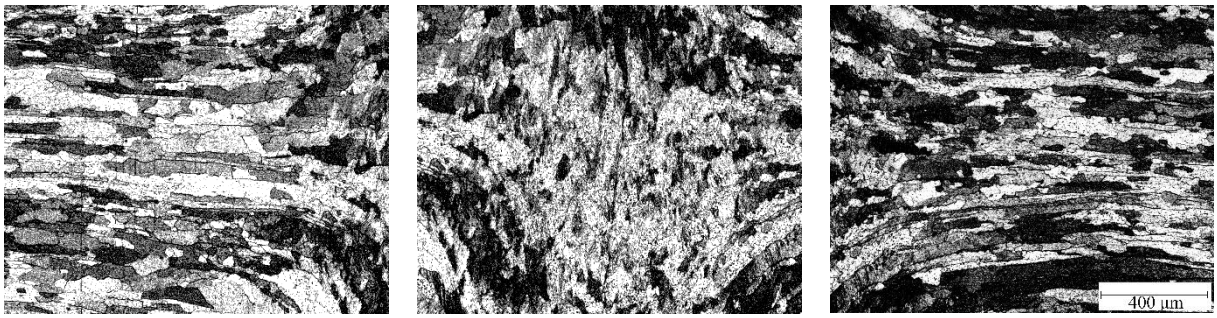

(a) (b) (c)

Figure 3.19: Optical images across the weld zone of Mo-La, Sample-2 (All images taken at 50X magnification): (a) Left transition from the base material to the weld zone, (b) middle of the weld and, (c) right transition from the weld zone to the base material.

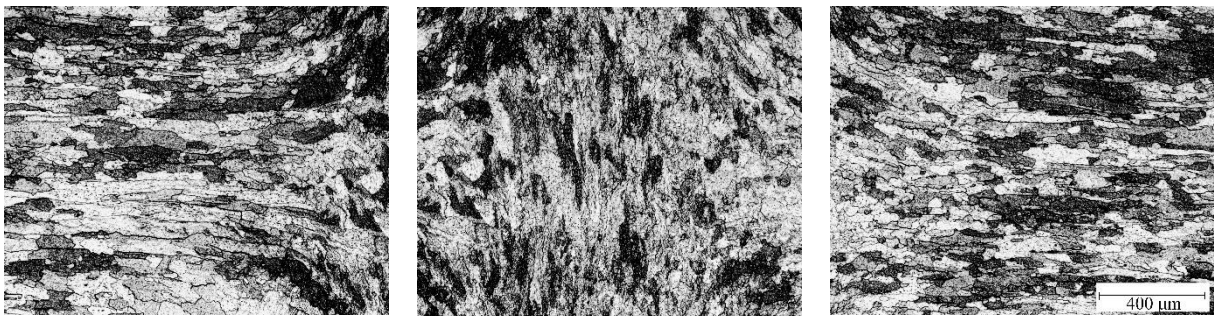

(a) (b) (c)

Figure 3.20: Optical images across the weld zone of Mo-La, Sample-3 (All images taken at 50X magnification): (a) Left transition from the base material to the weld zone, (b) middle of the weld and, (c) right transition from the weld zone to the base material.

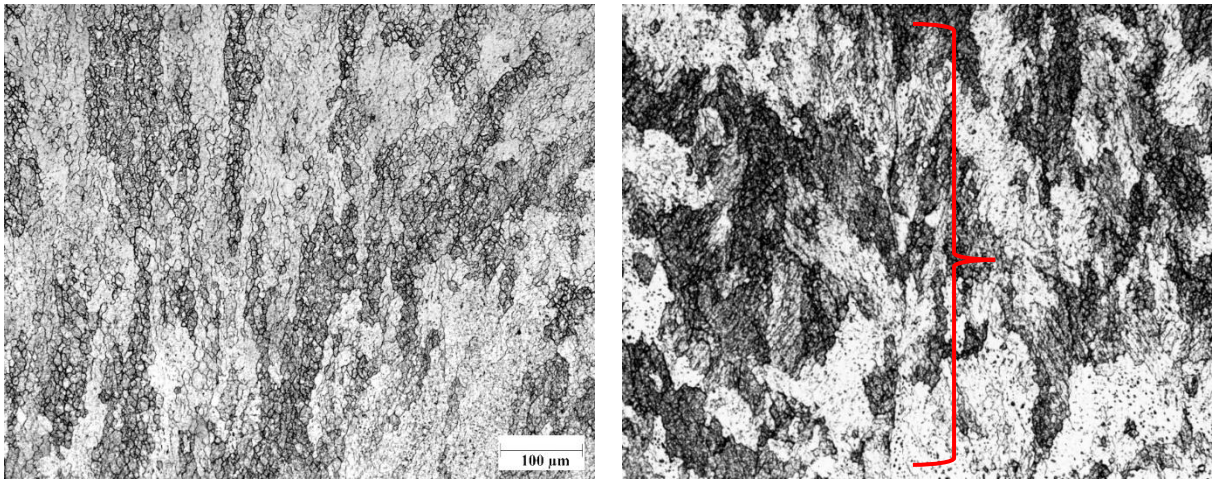

(a) (b)

Figure 3.21: Optical image of weld zone of Mo-La (a) Sample-1 (b) Sample-2. Shows the evidence of some dynamic recrystallization, Sample-2 shows a lack of mixing at the interface.

The grain sizes for the weld zones are measured by the mean linear intercept technique and are summarized in Table 3.4. The base material does show a slight decrease in grain size compared to the as-received Mo-La plate (55±10 µm for as-received). The weld zone does show a drastic change in grain size due to the presence of small equiaxed grains along with elongated grains.

Table 3.4: Grain sizes of PRWed Mo-La samples.

Sample No.	Base Material (µm)	Weld Zone (µm)
1	42±15	24±4
2	50±10	27±2
3	49±26	23±4

3.2.4.2 Vickers Microhardness Analysis

Vickers microhardness testing was used to create microhardness profile of the three Mo-La coupons, Figure 3.22. From the hardness profiles, all three samples showed slight increases in hardness through the weld zone. Sample-1 had an average microhardness of 216±21 VHN for the base material and a high of 227±3 VHN in the weld zone, resulting in an increase of 5%. Sample-2 had an average microhardness of 213±13 VHN for the base material and a high of 241±4 VHN, resulting in an increase of 13%. Sample-3 had an average microhardness of 212±19 VHN for the base material and a high of 235±3 VHN in the weld zone, resulting in an increase of 11%. The TMAZ width can be measured based on the hardness profile and the change shown in the optical microstructure. For Sample-1, the TMAZ was ~3.0 mm wide, Sample-2 was ~4.5

mm wide, and Sample-3 was ~4.0 mm wide. From the hardness profiles, the HAZ could not be observed as adverse effect of PRW.

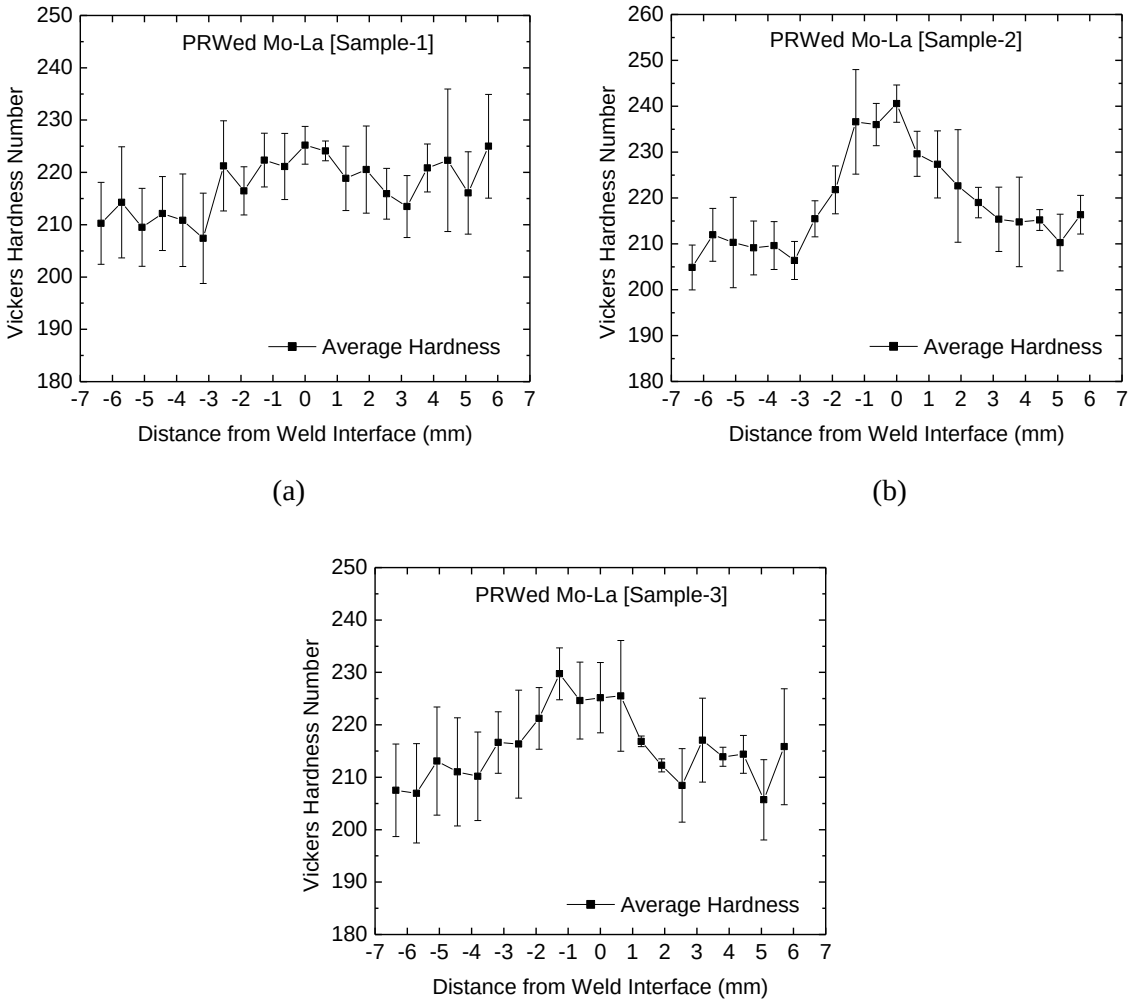

Figure 3.22: Microhardness profiles of Mo-La coupons (a) Sample-1 (b) Sample-2 (c) Sample-3.

3.2.4.3 Transmission Electron Microscopy and EBSD Results

TEM images of the weld zone of Mo-La sample 1 in Figure 3.23 show dislocations throughout the grains and around lanthanum oxide particles. The presence of subgrains (not well developed) in the weld zone can be seen in Figure 3.23(a); these grains are smaller than the as-received plate of Mo-La from Figure 3.6 (c).

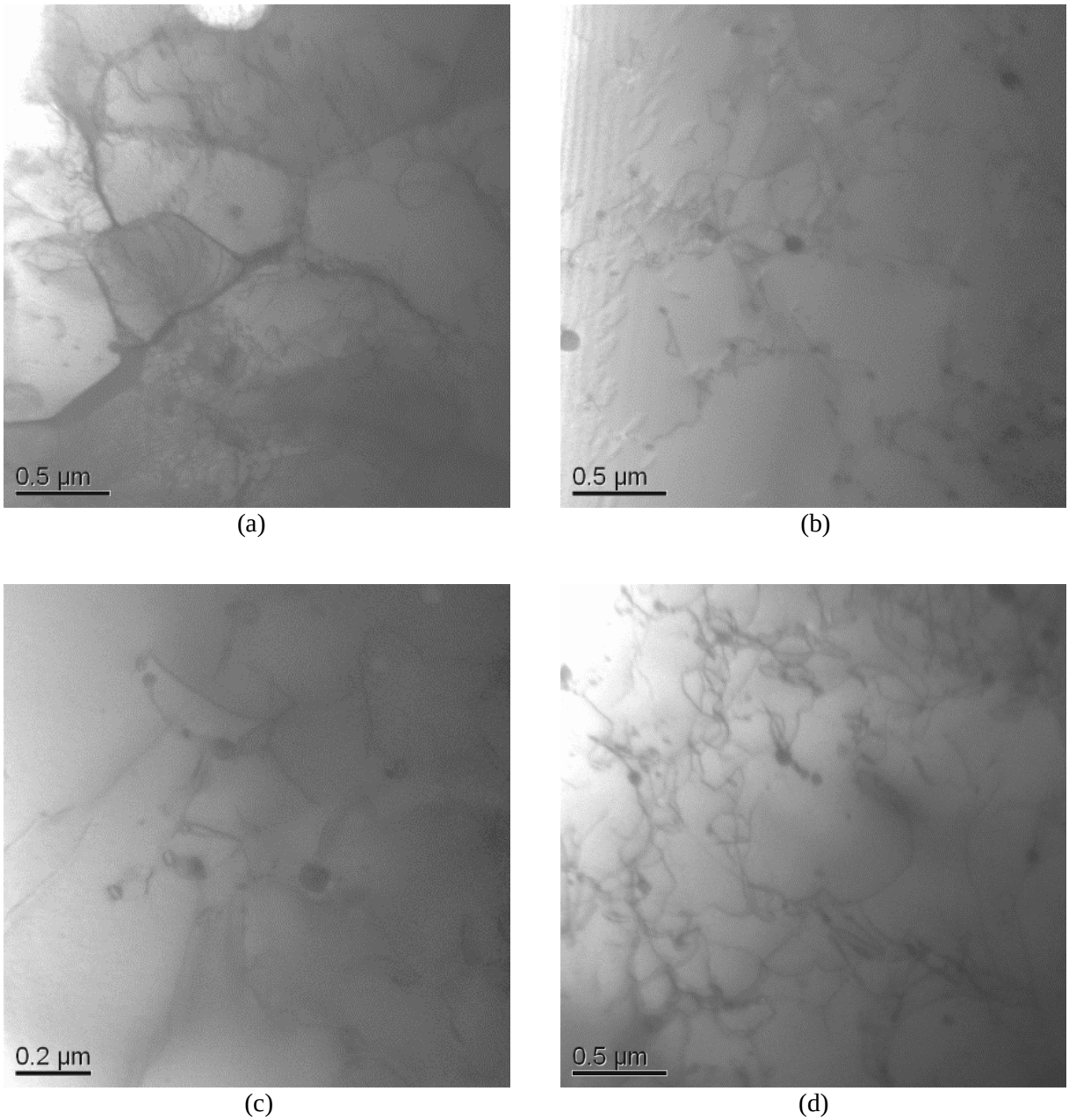

(a) (b)

(c) (d)

Figure 3.23: TEM images of the welded region of Mo-La sample 1, (a) (sub)grain structure with dislocations, (b-d) La_2O_3 particles and dislocations.

EBSD results show the presence of elongated grains plus the development of some subgrains, as shown in Figure 3.24. Figure 3.24 shows a comparison of as-received Mo-La to that of PRW Mo-La Sample-1 in the weld zone. More EBSD scans will be needed to understand the extent of recrystallization.

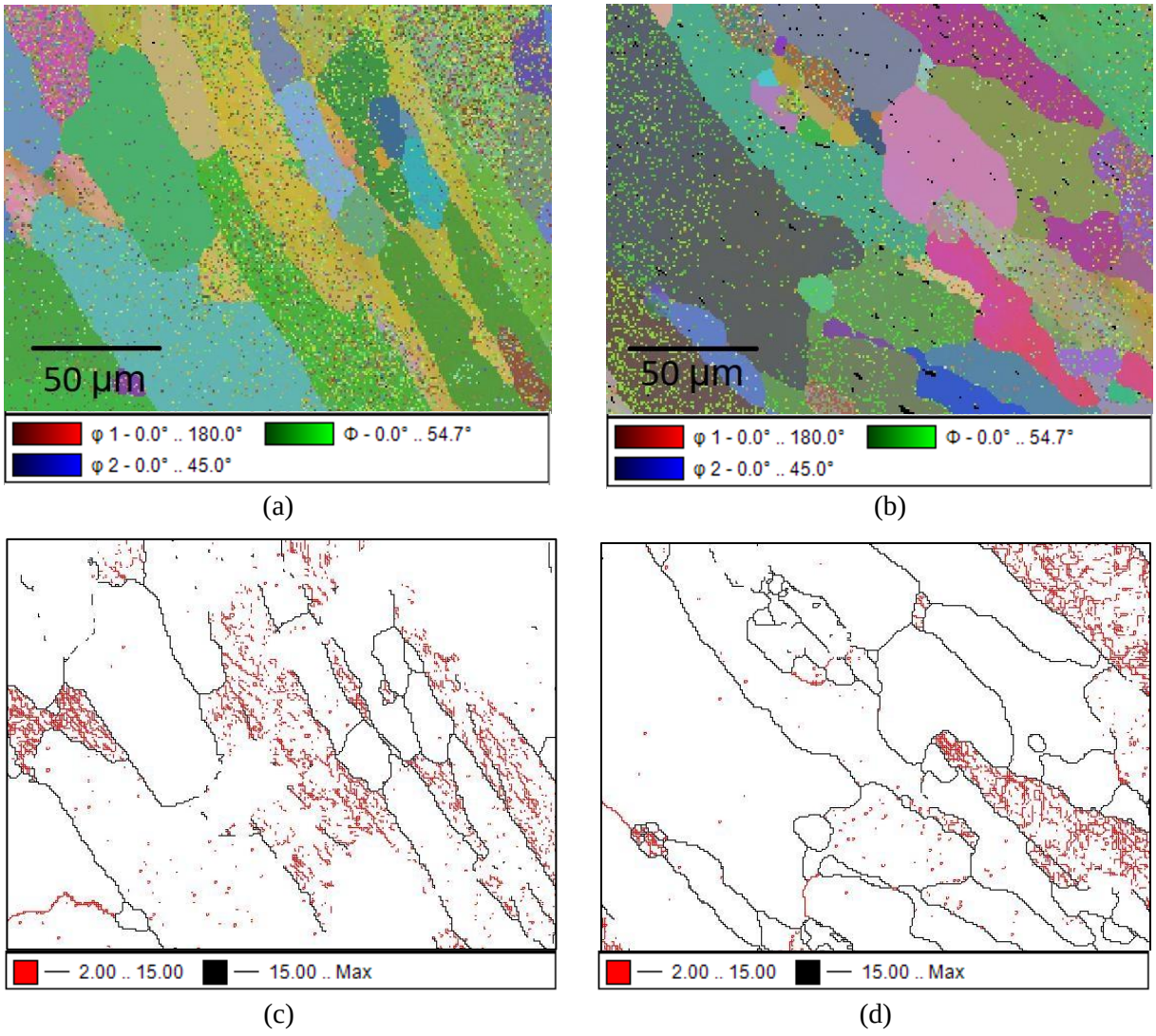

Figure 3.24: EBSD scans showing Euler maps and grain boundary angle maps for (a, c) AR Mo-La, (b, d) PRWed Mo-La Sample-1 weld zone.

4.0 Discussion

4.1 Effect of PRW Operating Parameters – Microstructure and Hardness

Applying sufficient uniaxial pressure for the PRW process resulted in sound welds for molybdenum-base materials except a couple of cases (such as formation of a crack in Sample-3 of PRWed TZM and lack of mixing in Sample-2 of PRWed Mo-La). By applying uniaxial pressure, the material at the joining interface are pushed closer together and due to the intermingling plastic flow, it is more likely to create a metallurgical bond during welding. [64] The impurities at the weld interface are expelled outwards along with some of the plastically deformed material to create an expulsion region, which reduces the adverse effect of any surface oxides being trapped within the weld zone. The effect of applied pressure on the PRW joint needs to be further explored to understand if applied pressure can affect the width of the TMAZ and to reduce material waste produced due to the creation of the expulsion region during PRW.

4.1.1 Microstructural Evolution During PRW

A noticeable change is observed, both microstructurally and microhardness, throughout the weld zone compared to the base material after the PRW process. All three current schedules applied for the molybdenum coupons, as summarized in Table 2.3, resulted in similar microstructure and microhardness profiles for each alloy. For pure molybdenum, the PRW process resulted in both dynamic recrystallization and grain growth throughout the weld zone. Dynamic recrystallization (DRX) occurs when a material has simultaneous presence of deformation and high temperatures, while static recrystallization occurs after deformation of a material has occurred followed by heat treatment. We can understand DRX by using the Zener-Hollomon parameter: [71, 72]

$$Z = \dot{\varepsilon} \cdot \exp(\frac{Q}{RT}) \quad (3)$$

and

$$d^{-1} = a + b\, lnZ \quad (4)$$

where $\dot{\varepsilon}$ is the strain rate, Q is the appropriate activation energy, R is the gas constant, T is the deformation temperature, d is grain diameter, and a and b are materials parameters. From Equations (3) [71] and (4) [72], higher strain rate and lower temperature lead to higher Z values, which result in smaller grain size. During the PRW process, the material flow and heat

distribution of PRW is complex; computational technique would need to be explored to understand the strain in different regions of the weld zone and the temperature profile. For the three welding schedules, strain rate and temperature should vary due to the different energy inputs and the rate of current per unit time as calculated in Appendix C. For each molybdenum alloy, only the activation energy should be different due to the presence of alloying elements. Some of the factors which influence DRX include stacking fault energy, initial grain size, thermo-mechanical processing conditions, and second phase particles. [51]

For DRX, a few different recrystallization processes exist including continuous dynamic recrystallization (CDRX), discontinuous dynamic recrystallization (DDRX), and geometric dynamic recrystallization (GDRX). CDRX involves mechanism through which cell or subgrain boundaries (i.e. low angle grain boundaries or LAGBs) are formed during deformation for materials with high stacking fault energies due to the efficient DRX, which progressively evolve into high angle grain boundaries (HAGBs) at larger deformations. This is also sometimes known as extended recovery. DDRX is observed for materials with low stacking fault energies where nucleation of new strain-free grains occurs, and these grains grow at the expense of regions full of dislocations, during hot deformation. GDRX can be observed at large strain rates where deformed grains become elongated with local serrations but remain distinguishable during deformation. [51]

For TZM, the optical images showed DRX prominently throughout the weld zone with clear equiaxed grains. The presence of the titanium and zirconium as alloying elements forming stable carbide particles appear to prevent grain growth from occurring. For TZM, the type of DRX appears to be CDRX, due to its uniform equiaxed grain morphology shown in TZM micrographs. For Mo-La, the optical images showed partial DRX present through most of the weld zone, with faint equiaxed grains developing within larger deformed grains. From EBSD scans of Mo-La, Figure 3.24, the as-received and the weld zone of the PRWed Mo-La showed similar grains sizes, shapes, and grain boundary angles. The weld zone EBSD scan did show a small increase in subgrains, however, more scans would need to be conducted to confirm it. Based on the review of DRX mechanisms in the work of Huang and Logé [51], it appears Mo-

La may have partial CDRX or geometric DRX. More studies are needed to confirm the exact nature of the DRX event that took place in Mo-La.

The effect of DRX and recrystallization in general for molybdenum alloys is clear with the change of the grain morphology throughout the weld zone. Research done by Brian Cockeram [52, 53] showed that the elongated 'pancake' shaped grains in the longitudinal cross section of wrought rolled plates exhibit higher ductility and higher fracture resistance than shorter/equiaxed grains because of the presence of ductile laminate toughening mechanisms and the anisotropic mechanical properties. To confirm this, mini-tensile testing would need to be performed on the as-received molybdenum plates and welded molybdenum samples.

4.1.2 Strengthening Mechanisms in the As-received and PRWed Molybdenum Alloys

For each molybdenum alloy, the changes in the hardness profiles directly correlated with the optical microstructure changes throughout the weld zone. The average Vickers hardness number for the as-received molybdenum plates, post PRW base material, and PRW weld zone were tabulated in Table 4.1, along with their respective grain sizes. The effect of DRX is clear for pure molybdenum and TZM PRW welds with decreases in microhardness throughout the weld zone.

Table 4.1: Comparison of grain sizes and microhardness for Mo-alloys, before and after PRW

Mo Alloy	Sample No.	As-Received (μm)	AR VHN	Base Material Post PRW (μm)	Base Material Post PRW VHN	Weld Zone Post PRW (μm)	Weld Zone PRW VHN
Pure Mo	1	32±15	251±13	33±6	252±15	62±9	203±3
	2			35±5	251±21	43±4	209±3
	3			32±3	253±15	49±6	202±4
TZM	1	43±17	279±15	36±15	307±16	20±2	245±4
	2			38±19	306±17	23±2	229±11
	3			40±9	306±19	21±2	238±6
Mo-La	1	55±10	203±4	42±15	216±21	24±4	227±3
	2			50±10	213±13	27±2	241±4
	3			49±26	212±19	23±4	235±3

To try to understand the effect of microstructural changes on mechanical behavior for pure molybdenum, TZM, and Mo-La, the operating strengthening mechanisms need to be explored for each of this material for both pristine and welded conditions. In this study, Vickers microhardness testing was conducted. But no tensile testing could be done to obtain actual tensile strength parameters like yield strength and ultimate tensile strength. But we know that hardness is generally roughly a measure of strength and generally directly proportional. In the literature, there are many instances of empirical equations available to correlate the tensile strength parameters with Vickers hardness. However, that is not the intent of the section given the lack of robustness of such relations. Therefore, in the next sections we qualitatively discuss the effect of individual strengthening mechanisms on the overall strength of each base material and the likely reasons of change in them after welding.

In general, the overall yield strength (σ_y) of a material can be represented as the summation of individual contributions made by lattice friction stress (σ_O) or basically Peierls-Nabarro stress, solid solution strengthening (σ_{SS}), dislocation strengthening (σ_D), grain boundary strengthening (σ_{GB}), and particle strengthening (σ_P). If present, subgrain boundary strengthening can be added to the grain boundary strengthening effect. While there are many forms of additivity relations available in the literature, for simplification the linear superposition of all strengthening mechanisms is considered here and is described in Equation (5). [67, 68]

$$\sigma_y = \sigma_O + \sigma_{SS} + \sigma_{GB} + \sigma_P + \sigma_D \quad (5)$$

For pure molybdenum, Equation (5) can be reduced to Equation (6) because of the lack of alloying elements for solid solution strengthening and particle strengthening.

$$\sigma_y = \sigma_O + \sigma_{GB} + \sigma_D \quad (6)$$

For TZM, Equation (7) needs to be used because of the presence of Ti and Zr creating Ti and Zr based carbide particles; these could provide possibility of solid solution strengthening. However, as Ti and Zr carbides are formed, and they are quite stable carbides, it is unlikely that Ti and Zr will be left in solid solution. Thus, TiC and ZrC particles strengthen the material with

particle strengthening. Given the incoherent nature of these particles, the particle strengthening effect in TZM will be mostly created via the Orowan dislocation bypassing mechanism. [67]

$$\sigma_y = \sigma_O + \sigma_{GB} + \sigma_P + \sigma_D \quad (7)$$

For Mo-La, Equation (7) can also be used because of the lack of alloying elements in the matrix for solid solution strengthening.

Since pure molybdenum, TZM, and Mo-La are molybdenum based materials, σ_O can be assumed to be the same for each alloy. From the work of Zhang et al. [65], the lattice friction stress (σ_O) of molybdenum was calculated to be 417 MPa. Solid solution strengthening occurs because solute atoms in metal introduce strain fields in lattice structure of the metal solvent (in this case Mo), which interact with dislocations. The contributions of these alloying elements are shown in Equation (8), where A_i is the strengthening coefficient of the alloying elements and C_i is concentration of the element (in wt%). [67]

$$\sigma_{SS} = \sum A_i C_i \quad (8)$$

The effect that grain boundaries have can be related to the well-known Hall-Petch relation, as shown in Equation (9). The decrease in grain size means an increase in area of grain boundaries, which act as barriers to dislocation motion, resulting in an increase in strength. [67]

$$\sigma_{GB} = k_{HP} D^{-1/2} \quad (9)$$

The effect that particle strengthening on molybdenum can be represented by the Orowan-Ashby equation, [66, 69] (Equation 10), which is a modification to the original Orowan particle bypassing model. Particle strengthening is likely the most important strengthening mechanism in TZM and Mo-La, especially for achieving high temperature strength. Particles, such as La_2O_3, TiC, and ZrC, impede dislocation movement.

$$\sigma_{P(Orowan-Ashby)} = \frac{0.538Gb\sqrt{f}}{d} \ln\left(\frac{d}{2b}\right) \quad (10)$$

where d is the mean particle diameter in μm, f is volume fraction of the particles in the matrix, G is the shear modulus, and b is the Burgers vector. The Orowan-Ashby equation shows that particle strengthening increases with the increase in volume fraction of the particle or the decrease in particle diameter. [66, 69]

Lastly, dislocation strengthening is generally created by the interaction between dislocations. For molybdenum, this would typically occur during the formation of the as-received plates as they are rolled from an extruded hot billet after sintering. Dislocation strengthening can be represented by the following equation:

$$\sigma_D = M\alpha G b \rho^{1/2} \tag{11}$$

where M is the Taylor factor of the polycrystalline material (generally taken as 2.733 for BCC metals) [70], G is the shear modulus, b is the Burgers vector, ρ is dislocation density, and α is a constant. For this research, exact values for each strengthening mechanism was not attainable; however, each strengthening mechanism can be used qualitatively to understand changes from the as-received to PRWed molybdenum alloys.

For pure molybdenum, the change in yield strength is strongly dictated by the change in grain size and the presence of dislocations. From optical microscopy and TEM images, the notable changes for pure molybdenum was recrystallized equiaxed grains, dislocation rearrangement and development of new grains, and grain growth, in the weld zone. The increase in grain size (Table 4.1) decreases σ_{GB} in the weld zone compared to the base material. The size of the subgrains within the microstructures of the base material and the weld zone did not change much. So, their effect could not explain the dip in the hardness. Recrystallization of grains decreased the dislocation density compared to the wrought as-received plate, this can result in the decrease of σ_D. Overall, the change in these two strengthening mechanisms should explain the decrease in hardness throughout the weld zone.

For TZM, the change in hardness throughout the weld zone can be attributed to a change in $\sigma_{GB}, \sigma_P, and\ \sigma_D$. For this research, the change in solid solution strengthening will not be considered because it is not known if Ti and Zr are increasing or decreasing as solute atoms within a molybdenum matrix. From optical microscopy and TEM images, the notable changes for TZM was recrystallized equiaxed grains and potential coarsening of carbide particles. The decrease in grain size, Table 4.1, should increase σ_{GB} in the weld zone compared to the base material. The potential coarsening of carbides would decrease the strengthening contribution of σ_P because of the increase diameter of particles. Lastly, it is not clear whether dislocation density is increasing or decreasing. From TEM images of the weld zone in TZM, most grains have large particles present with dislocation looping present. Thus, the main decrease in strength for TZM may be attributed to change in microstructure and potential coarsening of carbides in the weld zone.

For Mo-La, the change in yield strength throughout the weld zone can be attributed to a change in $\sigma_{GB}, \sigma_P, and\ \sigma_D$. From optical microscopy, TEM images, and EBSD maps, the notable changes for Mo-La was partially recrystallized grains and the presence of dislocations. Partial recrystallized grains and change in grain size, as tabulated in Table 4.1, should increase σ_{GB}. However, the effect of partially recrystallized grains adds complexity to whether σ_{GB} increases or not. One clear observation was the presence of dislocations in the weld zone while the as-received material did not have dislocations. The increase in dislocation density, which increases σ_D, appears to be the main strengthening mechanism difference between the base material and the weld zone of PRWed samples. From TEM images, La_2O_3 particles appear to maintain an average diameter of ~50 nm and were not agglomerating. This means σ_P contribution has not changed from the base material to the weld zone.

Overall, the presence of precipitates and dispersoids affects recrystallization or grain growth in molybdenum materials. Pure Mo recrystallization occurs roughly near 1,100 ºC. the presence of carbides in TZM increases the recrystallization temperature to 1,400 ºC. [57, 58] The presence of La_2O_3 in Mo-La increases the recrystallization temperature to 1,800 ºC [59, 60]. The higher recrystallization temperature of Mo-La appears to be the main reason why Mo-La did not fully

recrystallize during PRW. These stable and fine second phase particles appear to be the reason for the lack of grain growth in the weld zone for TZM and Mo-La. [54, 55]

4.2 Understanding Heat Generated During PRW and Its Effect on Temperature

During the PRW process, heat is mainly generated at the weld interface because the resistance is the highest compared to any other location. Because of the very transient nature of the process, it is not feasible to measure the temperatures experimentally during PRW by conventional means. The heat created from the Joule heating as shown in Equation (1), is what causes the temperature to rise among other effects. By assuming first that all Joule heat is used up for raising the temperature, the simple equation below (Equation 12) can provide us with a simple way of estimating the temperature during PRW..

$$H = m \cdot S \cdot (\Delta T) \tag{12}$$

where H is total energy [J], m is sample mass [g], S is specific heat [J/g·K], and ΔT is the temperature difference [K] of the peak temperature (T_{peak}) and initial temperature (T_o) of the sample (can be taken as room temperature or 298 K) . For molybdenum, specific heat is taken as 0.25 J/g·K and will be used for all alloys. [73] Here we have not taken into account the variation of specific heat as a function of temperature. The mass will have to be estimated by assuming that most of the TMAZ in the welded region participates in the heat capacity prior to heat transfer by conduction. For simplicity, heat transfer will not be considered for each molybdenum weld for the 'single-pass' method.

For estimating the mass, the smallest TMAZ width observed was 3 mm for Mo-La Sample-1. If it is assumed that both sides of the coupon weldments equally participate in PRW, the total volume calculated would be 53.6 mm^3 or 0.0536 cm^3. The density of molybdenum is 10.2 g/cm^3, which makes the mass of the TMAZ ~0.55 g. Table 4.2 shows the tabulated results for the predicted temperature at the weld interface. The calculated temperatures, as shown in Table 4.2, was clearly off; if we assume both weldments heated up, this would increase mass of the sample to 3.25 g. From Table 4.2, the temperature calculated is still too high for the entire sample, but lower than the melting point of molybdenum (2896 K) maintaining the nature of the solid-state nature of PRW.

Table 4.2: Calculated temperatures for 'single-pass' method of molybdenum materials, no conduction.

Material	Total Energy [J]	Temperature at Weld Zone [K]	Temperature for Entire Weldment [K]
Pure Mo	1,836	13,328	2,235
TZM	1,819	13,204	2,214
Mo-La	1,570	11,393	1,907

During PRW, we calculated an overall resistance, however, that resistance is not just present at the weld interface. Resistance occurs at the electrode-weldment surface contacts, within the joining material, weld interface, and any unknown sources. This summation of resistance is similar to adding resistors in series in circuits, as shown in Equation (13). [75]

$$R = R_1 + R_2 + \cdots + R_n \tag{13}$$

where R is resistance [Ω] and each subscript of R is an individual contribution in the PRW process. A 4-point probe technique would be needed to measure individual contributions to the overall resistance. [74] Computer modelling the PRW themall profile would require transient conduction equations, convection equations, Joule heating equation, and understanding the effect that passing high current such as heat loss due to the discharge spark generation (which occurs during PRW) and other effects. All of which is beyond the scope of this research, however, some prior modelling work has been done in understanding resistive spot welding, which could be useful for understanding PRW. [75]

4.3 Understanding Strain Generated During PRW

The PRW process induces strain at the weld interface due to a combination of applied uniaxial force and resistive heating to create severe plastic deformation. The strain present can be estimated by measuring the change in length of the weldments during the PRW process. For the coupon configuration, the total length of the two weldments was 0.70±0.02 inches (17.78±0.5 mm). The measured PRWed specimen lengths are tabulated in Table 4.3, along with strain calculations. For simplicity, only the first impulse of the weld current for the 'multi-pass' method, this means the 'single-pass' method has 3 cycles (50.01 ms) and the 'multi-pass' method has 5 cycles (83.35 ms).

Table 4.3: Calculated strain and strain rates for coupon configuration PRW

Material	Original Length (mm)	Length Post PRW (mm)	Change in Length (mm)	Strain (mm/mm)	Time (ms)	Strain rate (s^{-1})
Pure Mo Sample-1	17.78	15.00	2.78	0.16	50.01	3.12
Pure Mo Sample-2	17.78	15.80	1.98	0.11	83.35	1.34
Pure Mo Sample-3	17.78	15.30	2.48	0.14	83.35	1.67
TZM Sample-1	17.78	15.10	2.68	0.15	50.01	3.01
TZM Sample-2	17.78	15.90	1.88	0.11	83.35	1.27
TZM Sample-3	17.78	15.35	2.43	0.14	83.35	1.64
Mo-La Sample-1	17.78	15.20	2.58	0.15	50.01	2.90
Mo-La Sample-2	17.78	15.65	2.13	0.12	83.35	1.44
Mo-La Sample-3	17.78	15.40	2.38	0.13	83.35	1.60

While Table 4.3 shows strain and strain rates, the ‘multi-pass’ method does have complexity with the different heating stages. It is not known if strain occurs during the ‘pre-heat’ stage, further testing would need to be conducted. Stress was also calculated for PRW coupons, the applied force was 1,000 lb_f (4,448 N) and the weld interface has an area of 15.6 mm^2, thus a simple normal stress is calculated to be about 285 MPa.

The above deformation calculations provide only a simplified version of a complicated stress state. Computer modelling, specifically finite elemental analysis would aid in better understanding the stress/strain profile occurring throughout the joining process.

4.4 Comparison of PRW to Other Welding Techniques

To gauge the effectiveness of PRW for molybdenum based materials, a comparison to other welding techniques is necessary. This section will compare PRW to gas tungsten arc welding (GTAW), electron beam welding (EBW), and friction welding.

As discussed in the introduction, fusion welding in the presence of oxygen, nitrogen, and other impurities severely affects the quality of welds for molybdenum based materials. [12, 33, 34] For GTAW, which typically uses argon gas, the melting of molybdenum results in dendritic grains which adversely affect the strength and ductility of the material. Additionally, a large heat affected zone (HAZ) can be observed, on the scale of several mm in width because of the high temperature involved in such process. Electron beam welding (EBW) has much better properties than GTAW due to the high energy density of the welding beam. The energy is more concentrated than what is shown with GTAW and the heat can move away quickly as the rest of the material can act as heat sink. However, EBW still shows a narrower HAZ of a couple of mm, which can be shown in the optical cross-section of a EBW TZM, as shown in Figure 4.1. A Vickers microhardness profile can be seen for the micrograph shown in Figure 4.1. It appears that the HAZ had a greater adverse effect on the hardness than the melted/re-solidified region at the nugget region; The HAZ resulted in about a 29% decrease in Vickers microhardness for TZM. [56]

The work of Kolarikova et al. [56] showed the Vickers microhardness profile for EBW decrease in microhardness by about 50% for EBWed TZM. For PRW, a total decrease of 20-25% in the weld zone was noted in Vickers microhardness values and a minimal HAZ.

Friction welding is another welding technique which has been used for joining different molybdenum alloys. From Andrzej Ambroziak [35], friction welding of TZM to TZM specimens, in liquid oil, showed a decrease from a Vickers microhardness of 350 $HV_{0.05}$ of the base material to a 250 $HV_{0.05}$ for where the welding interface. However, a HAZ was also observed, which had a Vickers microhardness of 220 $HV_{0.05}$, a 37% decrease to that of the base material. The total TMAZ and HAZ for friction welding of TZM to TZM was ~16 mm wide. Much of the welding performed by PRW resulted in a TMAZ of less than 5 mm width. PRW showed improved Vickers microhardness profiles than friction welding. More studies are needed to further establish this point.

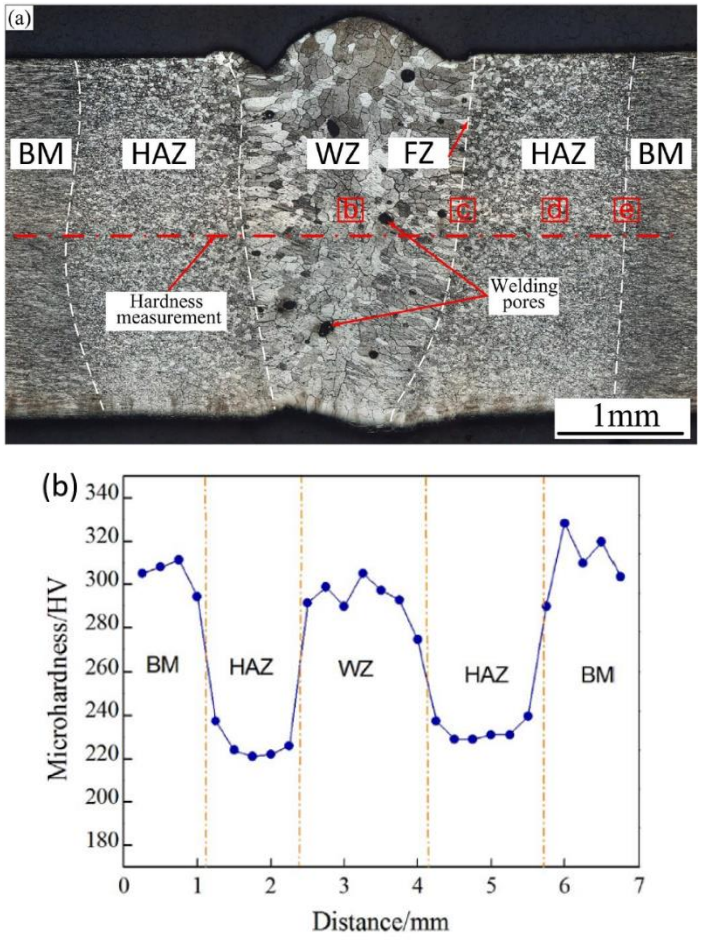

Figure 4.1: (a) Macrostructure of cross section of EBW weld of TZM and (b) Vickers microhardness profile [56]

Friction stir welding is another technique which has recently surfaced as a solid-state welding technique for unalloyed molybdenum. Fujii et al. [61], showed that commercially pure molybdenum of 1.5 mm thickness could be friction stirred welded using a Ir-Re alloy tool while still retaining 86% of its strength compared to the base material. In comparison, the PRW process of pure molybdenum resulted in a 17% decrease in Vickers microhardness.

5.0 Summary and Conclusions

Pressure resistance welding has been studied previously on ODS steels, F/M steels, and tungsten and was demonstrated to be an effective welding technique with promising results. The current research was undertaken to build on the past progress and apply the understanding to PRW of molybdenum-based materials.

5.1 PRW of Molybdenum Rod

With the knowledge gained from PRW of tungsten, similar welding parameters were chosen to test whether those welding parameters would work for molybdenum. The applied current for the tungsten rod test sample had a weld current of 65% (maximum 30 kA) with the multi-pass method. Since molybdenum has a lower melting point than tungsten, a weld current of 55% was chosen with the multi-pass method. Additionally, we were interested in the importance of applied pressure on the welded samples, so we tested samples with 1,000 lb_f and some with 150lb_f. It was quickly noticed the importance of applied force, sample without adequate force did not produce a sound weld. The samples which had 1,000 lb_f force applied created sound welds.

The base material had an average microhardness of 241 VHN and a low of about 200 VHN in the weld zone, which resulted in a 16.6% decrease in hardness. Optical microscopy revealed a change in the grain morphology from long grains seen in the base material to equiaxed grains seen in the weld zone. Additionally, dynamic recrystallization was observed, which can be attributed to the lack of precipitates present in pure molybdenum. Dynamic recrystallization was present due to the higher temperature at the joint interface coupled with deformation. Dynamic recrystallization was shown in the thermo-mechanically affected zone, which correlated well with the microhardness profile.

5.2 PRW of Pure Mo, TZM, and Mo-La Coupons

The PRW process applied to pure molybdenum, TZM, and Mo-La coupons produced largely sound welds. Pure molybdenum was used as a basis for comparing the PRW process with TZM and Mo-La, both of which have strengthening particles which help improve creep resistance and strength at higher temperatures, and makes the material more resistant to recrystallization.

For PRW, pure molybdenum showed a change in grain morphology throughout the weld zone from elongated grains shown in the base material to equiaxed dynamically recrystallized grains in the weld zone. Additionally, grain growth occurred in pure molybdenum weld, which makes sense because of the lack of stable particles or solutes. The Vickers microhardness profile for PRWed pure molybdenum did show a decrease in microhardness of 17-20% for the different welding schedules.

For TZM, the PRW process also showed a change in grain morphology throughout the weld zone from elongated grains shown in the base material to dynamically recrystallized, equiaxed grains. Unlike pure molybdenum welds, TZM did not show grain growth or differences in grain size in the weld zone between the different welding schedules. The Vickers microhardness profile for PRWed TZM did show a decrease in microhardness of 20-25% for the different welding schedules.

For Mo-La, the PRW process also showed a change in grain morphology throughout the weld zone, with some patches of dynamically recrystallized equiaxed grains, with the rest of the weld zone in the unrecrystallized state. Unlike pure molybdenum welds, Mo-La did not show grain growth or differences in grain size in the weld zone between different welding schedules. Also, because of the presence of stable and fine lanthanum oxide particles, the dynamic recrystallization was also found to be restricted. The Vickers microhardness profile for PRWed Mo-La did show an increase in microhardness of 5-13% for the different welding schedules.

Overall, more research is needed to optimize the PRW process for molybdenum based materials by changing applied pressure to see how it affects dynamic recrystallization. The variation of applied pressure will change the strain rates at the joining interface and should provide more data for understanding the dynamic recrystallization occurring during PRW in-depth. Furthermore, varying the applied pressure could reveal if the thermo-mechanically affected zone can be reduced. Additionally, not much is known on why a crack may form in a welded material; the current conclusion is that cracks may form with increasing energy input due to thermal shock. However, this still needs to be further established.

6.0 Future Work

While this study covered pressure resistance welding of pure molybdenum, TZM, and Mo-La coupons, more research is needed to optimize the welding parameters for each alloy. Micro-tensile testing can be used to compare welded samples to as-received samples, which will give important mechanical property data. Additionally, further research into molybdenum tubes will be needed to simulate fuel cladding rod. With molybdenum rods, burst test can be used to test the strength of the welded tubes. Other molybdenum alloys may be of interest, including various Mo-Re alloys which are of interest as a fuel cladding material in space fission reactors.

Modelling and computational work could be explored to gain an understanding of the temperature and strain profile in samples during welding and to try to understand how that relates to recrystallization or changes in the microstructure. Additionally, changing the applied pressure could help minimize the wasted material from the expulsion region as well as reduce the width of the TMAZ region, if the 1,000 lb_f (4.45 kN) was more than what is required for a good quality weld.

After optimization of the PRW process, irradiation testing would be needed to test how irradiation would affect the mechanical properties of PRWed samples. Both tensile testing and creep testing would need to be performed on irradiated samples to test the strength and longevity of welded molybdenum. Residual stress measurement of the joint should be performed. Additionally, heat treatments could be explored to see whether it would improve the microstructure of the weld zone. Lastly, scaling up the welded samples to meet the specification of an actual fuel rod would be needed and further optimization and testing need to be performed prior to PRW on an industrial scale.

7.0 References

[1] Milbrandt, Anelia R., et al. “Renewable Energy Potential on Marginal Lands in the United States.” *Renewable and Sustainable Energy Reviews*, vol. 29, 2014, pp. 473–481., doi:10.1016/j.rser.2013.08.079.

[2] Saenko, V., et al. “The Chernobyl Accident and Its Consequences.” *Clinical Oncology*, vol. 23, no. 4, 2011, pp. 234–243., doi:10.1016/j.clon.2011.01.502.

[3] Kim, Younghwan, et al. “Effect of the Fukushima Nuclear Disaster on Global Public Acceptance of Nuclear Energy.” *Energy Policy*, vol. 61, 2013, pp. 822–828., doi:10.1016/j.enpol.2013.06.107.

[4] Serp, Jérôme, et al. “The Molten Salt Reactor (MSR) in Generation IV: Overview and Perspectives.” *Progress in Nuclear Energy*, vol. 77, 2014, pp. 308–319., doi:10.1016/j.pnucene.2014.02.014

[5] Adamantiades, A., and I. Kessides. “Nuclear Power for Sustainable Development: Current Status and Future Prospects.” *Energy Policy*, vol. 37, no. 12, 2009, pp. 5149–5166., doi:10.1016/j.enpol.2009.07.052.

[6] Nuclear Energy Agency Organisation for Economic Co-Operation and Development. *Nuclear Fuel Behaviour in Loss-of-Coolant Accident Conditions*. State-of-the-Art Report NEA No. 6846 (2009).

[7] Abram, Tim, and Sue Ion. “Generation-IV Nuclear Power: A Review of the State of the Science.” *Energy Policy*, vol. 36, no. 12, 2008, pp. 4323–4330., doi:10.1016/j.enpol.2008.09.059.

[8] Corwin, William R, et al. “Generation IV Reactors Integrated Materials Technology Program Plan: Focus on Very High Temperature Reactor Materials.” 2008, doi:10.2172/951084.

[9] Yvon, Pascal, Marion Le Flem, Céline Cabet, and Jean Louis Seran. "Structural Materials for next Generation Nuclear Systems: Challenges and the Path Forward." *Nuclear Engineering and Design* 294 (2015): 161-69. Web. 1 Feb. 2017.

[10] Murty, K.L., and I. Charit. "Structural Materials for Gen-IV Nuclear Reactors: Challenges and Opportunities." *Journal of Nuclear Materials* 383.1-2 (2008): 189-95. Web. 30 Jan. 2017.

[11] Azevedo, C.R.F. "Selection of Fuel Cladding Material for Nuclear Fission Reactors." *Engineering Failure Analysis* 18.8 (2011): 1943-962. Web. 1 Feb. 2017.

[12] El-Genk, Mohamed S., and Jean-Michel Tournier. “A Review of Refractory Metal Alloys and Mechanically Alloyed-Oxide Dispersion Strengthened Steels for Space Nuclear Power Systems.” *Journal of Nuclear Materials*, vol. 340, no. 1, 2005, pp. 93–112., doi:10.1016/j.jnucmat.2004.10.118.

[13] Association, IMOA International Molybdenum. “A World with Molybdenum.” IMOA: International Molybdenum Association, www.imoa.info/

[14] Carron, N. “An Introduction to the Passage of Energetic Particles through Matter.” Oct. 2006, doi:10.1201/9781420012378.

[15] Alemberti, Alessandro, et al. “Overview of Lead-Cooled Fast Reactor Activities.” *Progress in Nuclear Energy*, vol. 77, 2014, pp. 300–307., doi:10.1016/j.pnucene.2013.11.011.

[16] Lide, David R. *CRC Handbook of Chemistry and Physics: a Ready-Reference Book of Chemical and Physical Data*. Chemical Rubber Publishung Company, 2004.

[17] *Handbook on Lead-Bismuth Eutectic Alloy and Lead Properties, Materials Compatibility, Thermal-Hydraulics and Technologies*. OECD Nuclear Energy Agency, 2007.

[18] Rooijen, W. F. G. Van. "Gas-Cooled Fast Reactor: A Historical Overview and Future Outlook." *Science and Technology of Nuclear Installations*, vol. 2009, 2009, pp. 1–11., doi:10.1155/2009/965757.

[19] Kelly, John E. "Generation IV International Forum: A Decade of Progress through International Cooperation." *Progress in Nuclear Energy*, vol. 77, 2014, pp. 240–246., doi:10.1016/j.pnucene.2014.02.010.

[20] King, Jeffrey C., and Mohamed S. El-Genk. "Submersion-Subcritical Safe Space (S4) Reactor." *Nuclear Engineering and Design*, vol. 236, no. 17, 2006, pp. 1759–1777., doi:10.1016/j.nucengdes.2005.12.010.

[21] El-Genk, Mohamed S. "Space Nuclear Reactor Power System Concepts with Static and Dynamic Energy Conversion." *Energy Conversion and Management*, vol. 49, no. 3, 2008, pp. 402–411., doi:10.1016/j.enconman.2007.10.014.

[22] R. Hickman, B. Panda, and S. Shah, Fabrication of high temperature cermet materials for nuclear thermal propulsion, 53rd JANNF Propulsion Meeting, 1st Spacecraft Propulsion Subcommittee Meeting, Monterey CA, December 2005.

[23] P.F. Venneri and Y. Kim, A feasibility study on low enriched uranium fuel for nuclear thermal rockets – II: Rocket performance, Progress in Nuclear Energy, 87 (2016) 156-167.

[24] V. Patel et al., Comparing low enriched fuel to highly enriched fuel for use in nuclear thermal propulsion systems, in: 52nd AIAA/SAE/ASEE Joint Propulsion Conference, American Institute of Aeronautics and Asronautics (2016).

[25] W.D.M. Eades, C.R. Joyner II, Comparison of LEU and HEU cermet nuclear thermal propulsion systems at 16,000 lbf thrust, in: Nuclear and Emerging Technologies for Space 2016, 2016, USRA: Huntsville, Alabama.

[26] H.D Hedrich, H.G. Meyer, G. Haufler, et al. "Joining of ODS Superalloys." *High-Temperature Materials for Power Engineering* (1990).

[27] L.R. Zirker, J.H. Bottcher, S. Shikakura, C.L. Tsai and M.L. Hamilton, "Fabrication of oxide dispersion strengthened ferritic clad fuel pins," International Conference on Fast Reactors and Related Fuel Cycles, October 28-31, 1991, Kyoto, Japan.

[28] Debroy, T., and S. A. David. "Physical Processes in Fusion Welding." *Reviews of Modern Physics*, vol. 67, no. 1, Jan. 1995, pp. 85–112., doi:10.1103/revmodphys.67.85.

[29] Kou, Sindo. "Welding Metallurgy." 2002, doi: 10.1002/0471434027

[30] D. Codd. *Seam Welded Air-Hardenable Corrosion Resistant Steel Tubing*. KVA, Inc. (April 2005)

[31] S. Kalpakjian and S.R. Schmid *Manufactoring Engineering and Technology.* 4th. Upper Saddle River, New Jersey: Prentice Hall, 2001.

[32] I.G. Wright, G. Tatlock, H. Al-Badairy, et al. *Summary of Prior Work on Joining of Oxide Dispersion-Strengthened Alloys.* Oak Ridge National Laboratory, Dept. of Energy, (May 2009).

[33] Mueller, A.J., et al. "Evaluation of Oxide Dispersion Strengthened (ODS) Molybdenum and Molybdenum–Rhenium Alloys." *International Journal of Refractory Metals and Hard Materials*, vol. 18, no. 4-5, 2000, pp. 205–211., doi:10.1016/s0263-4368(00)00028-7.

[34] Fujii, Tadayuki and Rozak, Gary A. "*Effects of Amounts of Oxygen on TIG-Weldability of Molybdenum"* Sunric Co and H.C. Starck Inc.

[35] Ambroziak, Andrzej. "Friction Welding of Molybdenum to Molybdenum and to Other Metals." *International Journal of Refractory Metals and Hard Materials*, vol. 29, no. 4, 2011, pp. 462–469., doi:10.1016/j.ijrmhm.2011.02.005.

[36] Tabernig, B., and N. Reheis. "Joining of Molybdenum and Its Application." *International Journal of Refractory Metals and Hard Materials*, vol. 28, no. 6, 2010, pp. 728–733., doi:10.1016/j.ijrmhm.2010.06.008.

[37] A. Ambroziak, "Friction welding of molybdenum to molybdenum and to other metals," Inter. J. Refractory Metals & Hard Materials, 29 (2011) 462-469.

[38] R.S. Mishra and Z.Y. Ma, *Materials Science and Engineering* 50 (2005): 1-78.

[39] Nandan, R, et al. "Recent Advances in Friction-Stir Welding - Process, Weldment Structure and Properties." *Progress in Materials Science*, vol. 53, no. 6, 2008, pp. 980–1023., doi:10.1016/j.pmatsci.2008.05.001.

[40] Carpenter, S H, and R H Wittman. "Explosion Welding." *Annual Review of Materials Science*, vol. 5, no. 1, 1975, pp. 177–199., doi:10.1146/annurev.ms.05.080175.001141.

[41] J. McGinley. "Electromagnetic Pulse Technology as a Means of Joining Generation IV Cladding Materials." *Proceeding of the 17th International Conference on Nuclear Engineering* (July 2009)

[42] L.E. Brown, B.K. Kad, G. Smith, et al. *Development of ODS Heat Exchanger Tubing.* Report No. 47572GTH, Dept. of Energy, 2008.

[43] E. Dyadko. *Novel Joining Technique for Oxide Dispersion-Strengthened Iron Aluminide Alloys.* Quarterly Report No. 7. Materials and Electrochemical Research (MER) Corporation, Tucson, Az, 2003.

[44] S. Ukai, T. Kaito, M. Seki, et al. "Oxide Dispersion-Strengthened (ODS) Fuel Pins Fabrication for BOR-60 Irradiation Test." *Journal of Nuclear Science and Technology* 42, no. 1 (January 2005): 109-122.

[45] W.R. Kanne, Jr. *Solid-State Resistance Upset Welding: A Process with Unique Advantages for Advanced Materials.* Report No. WSRC-MS-93-305. Savannah River Site, Dept. of Energy, 1994.

[46] M. Seki, K. Hirako, S. Kono, et al. "Pressurized Resistance Welding Technology Development in 9Cr-ODS Martensitic Steels." *Journal of Nuclear Materials* 329-333 (2004): 1534-1538.

[47] Larry Zirker, and Craig Tyler. *Pressure Resistance Welding of High Temperature Metallic Materials*. United States: N. p., 2010. Web.

[48] N. Jerred, Solid state joining of high temperature metallic materials via pressure resistance welding for advanced nuclear reactor applications, MS Thesis, University of Idaho, 2011.

[49] Jerred, Nathan. "Molybdenum Joining" Instructions on pressure resistance welding. March, 2017. CAES, Idaho Falls, ID.

[50] Pöhl, C., et al. "Metallographic Characterization of the Molybdenum Based Alloy MHC by a Color Etching Technique." *Materials Characterization*, vol. 77, 2013, pp. 63–69., doi:10.1016/j.matchar.2013.01.001.

[51] Huang, K., and R.e. Logé. "A Review of Dynamic Recrystallization Phenomena in Metallic Materials." *Materials & Design*, vol. 111, 2016, pp. 548–574., doi:10.1016/j.matdes.2016.09.012.

[52] Cockeram, B.v. "The Mechanical Properties and Fracture Mechanisms of Wrought Low Carbon Arc Cast (LCAC), Molybdenum–0.5pct Titanium–0.1pct Zirconium (TZM), and Oxide Dispersion Strengthened (ODS) Molybdenum Flat Products." *Materials Science and Engineering: A*, vol. 418, no. 1-2, 2006, pp. 120–136., doi:10.1016/j.msea.2005.11.030.

[53] Cockeram, B.v. "The Role of Stress State on the Fracture Toughness and Toughening Mechanisms of Wrought Molybdenum and Molybdenum Alloys." *Materials Science and Engineering: A*, vol. 528, no. 1, 2010, pp. 288–308., doi:10.1016/j.msea.2010.09.009.

[54] Fan, Jinglian, et al. "Effect of Alloying Elements Ti, Zr on the Properties and Microstructure of Molybdenum." International Journal of Refractory Metals and Hard Materials, Vol. 27, no. 1, 2009, pp. 78–82., dio:10.1016/j.ijrmhm.2008.03.2006

[55] Majumdar, S., et al. "A Study of Hot Deformation Behavior and Microstructure Characterization of Mo–TZM Alloy." Journal of Nuclear Materials, vol. 385, no. 3, 2009, pp. 545–551., doi:10.1016/j.jnucmat.2008.12.049

[56] Kolarikova, M, Kolarik, L, and Vondrous, P. "Welding of Thin Molybdenum Sheets by EBW and GTAW." *23rd DAAAM International Symposium Conference Papers*, DAAAM International, 2012, pp. 1,005–1,008.

[57] Cockeram, B.v. "The Role of Stress State on the Fracture Toughness and Toughening Mechanisms of Wrought Molybdenum and Molybdenum Alloys." *Materials Science and Engineering: A*, vol. 528, no. 1, 2010, pp. 288–308., doi:10.1016/j.msea.2010.09.009.

[58] Mrotzek, T., et al. "Hardening Mechanisms and Recrystallization Behaviour of Several Molybdenum Alloys." *International Journal of Refractory Metals and Hard Materials*, vol. 24, no. 4, 2006, pp. 298–305., doi:10.1016/j.ijrmhm.2005.10.003.

[59] R. Bianco and R. W. Jr Buckman. Evaluation of oxide dispersion strengthened (ODS) molybdenum alloys. In ASM/TMS symposium on high-temperature materials, 1995.

[60] M. Endo, K. Kimura, T. Udagawa, S. Tanabe, and H. Seto. The effects of doping molybdenum wire with rare earth elements. High Temperatures - High Pressures, 21:129–129–137, 1990.

[61] Fujii, Hidetoshi, et al. “Microstructure and Mechanical Properties of Friction Stir Welded Pure Mo Joints.” *Scripta Materialia*, vol. 64, no. 7, 2011, pp. 657–660., doi:10.1016/j.scriptamat.2010.12.014.

[62] Barr, Christopher M., et al. “Anisotropic Radiation-Induced Segregation in 316L Austenitic Stainless Steel with Grain Boundary Character.” *Acta Materialia*, vol. 67, 2014, pp. 145–155., doi:10.1016/j.actamat.2013.11.060

[63] Lide, David R., ed. (1994). "Molybdenum". CRC Handbook of Chemistry and Physics. 4. Chemical Rubber Publishing Company. p. 18.

[64] Phillips, David H. “Solid-State Welding Processes.” *Welding Engineering*, 2015, pp. 95–113., doi:10.1002/9781119191407.ch4.

[65] Zhang GJ, Sun YJ, Niu RM, Sun J, Wei JF, Zhao BH. Microstructure and strengthen mechanism of oxide lanthanum dispersion strengthened mo alloy. Adv Eng Mat 2004;6:943-8.

[66] Hu W, Chen J, Starke Jr EA. Precipitation strengthening of stress-aged Al–xCu alloys. Acta Mater. 2000;48:2239–46

[67] Wang, J., Yuan, W., Mishra, R. S., & Charit, I. (2013). Microstructure and mechanical properties of friction stir welded oxide dispersion strengthened alloy. *J. Nucl. Mater.*, *432*(1), 274-280.

[68] Queyreau, S., Monnet, G., & Devincre, B. (2010). Orowan strengthening and forest hardening superposition examined by dislocation dynamics simulations. *Acta Mater.*, *58*(17), 5586–5595.

[69] Fu, J., Li, G., Mao, X., & Fang, K. (2011). Nanoscale cementite precipitates and comprehensive strengthening mechanism of steel. *Metall. Mater. Trans. A*, *42*(12), 3797-3812.

[70] Rosenberg, J. M., & Piehler, H. R. (1971). Calculation of the Taylor factor and lattice rotations for bcc metals deforming by pencil glide. *Metall. Trans.*, *2*(1), 257-259.

[71] Zener, C., & Hollomon, J. H. (1944). Effect of strain rate upon plastic flow of steel. *J. Appl. Phys.*, *15*(1), 22-32.

[72] Ammouri, A.H., Kridli, G., Ayoub, G., & Hamade, R.F. (2015). Relating grain size to the Zener–Hollomon parameter for twin-roll-cast AZ31B alloy refined by friction stir processing. *J. Mater. Process. Technol.*, *222*, 301-306.

[73] Kirillin, V.a., et al. “Experimental Determinaton of the Enthalpy and Heat Capacity of Molybdenum up to 2337Â°C.” *International Journal of Heat and Mass Transfer*, vol. 5, no. 1-2, 1962, pp. 1–9., doi:10.1016/0017-9310(62)90097-2.

[74] Schuetze, Andrew P., et al. “A Laboratory on the Four-Point Probe Technique.” *American Journal of Physics*, vol. 72, no. 2, 2004, pp. 149–153., doi:10.1119/1.1629085.

[75] Luo, Yi, et al. “Regression Modeling and Process Analysis of Resistance Spot Welding on Galvanized Steel Sheet.” *Materials & Design*, vol. 30, no. 7, 2009, pp. 2547–2555., doi:10.1016/j.matdes.2008.09.031.

Appendix A: Molybdenum Alloys Certification

H.C.Starck

MOLYBDENUM POWDER METALLURGY PRODUCTS

Number PD-7014
Issue 1-04.03.2010

Pure Molybdenum Sheet Premium Grade PS-100-2

Description of Product Rolled molybdenum sheet produced from pressed and sintered powder metallurgy sheet bar.

Chemical Characteristics[1)]
(Mass fraction in % [cg/g]; ppm [µg/g])

The chemical composition of the molybdenum powder used for producing sheet bar shall conform to the following limits:

Molybdenum (By Difference)	min.	99.95	%
Mg	max.	0.001	%
Mn	max.	0.001	%
Ni	max.	0.002	%
Al	max.	0.002	%
Cu	max.	0.002	%
Pb	max.	0.002	%
Ti	max.	0.002	%
Ca	max.	0.003	%
Si	max.	0.003	%
Sn	max.	0.003	%
Cr	max.	0.005	%
C	max.	0.005	%
Fe	max.	0.005	%

Structure Sheet will be supplied in a stress-relieved condition unless otherwise requested.

Mechanical Properties Tensile tests will be conducted at room temperature (65°F – 85°F) using a strain rate of 0.002 to 0.005 in/in/min. through 0.6 % offset and 0.02 to 0.05 in/in/min. to fracture. Tensile properties will be determined on specimens taken transverse to the final rolling direction. Test specimens will be prepared and tested according to ASTM Specification No. E-8, utilizing a gage length of 2 inches.

Figure A.1: Chemical composition certification of pure Mo. *Source H.C. Starck*

H.C.Starck

MOLYBDENUM POWDER METALLURGY PRODUCTS Number PD-7001
Issue 2-2015-09-17

MOLYBDENUM ALLOY P/M - TZM
Powder Metallurgy Sheet 2702

Description of Product This specification covers rolles molybdenum alloy (molybdenum + 0.5 % titanium + 0.1 % zirconium) sheet produced from pressed and sintered powder metallurgy sheet bar.

Chemical Characteristics[1)]
(Mass fraction in % [cg/g]; ppm [µg/g])

The chemical composition of the molybdenum blended powder used for producing sheet bar shall conform to the following limits:

Mo (By Difference)	min.	99.2	%
N (Sintered Material)	max.	0.002	%
O (Sintered Material)	0.025 -	0.040	%
Si	max.	0.005	%
Ni	max.	0.005	%
Fe	max.	0.010	%
C	0.010 -	0.040	%
Zi	0.06 -	0.12	%
Ti	0.40 -	0.55	%

Structure Sheet will be supplied in a stress-relieved condition unless otherwise requested.

Mechanical Properties Tensile properties can be supplied on request when Purchase Order is placed.

Figure A.2: Chemical composition certification of TZM. *Source H.C. Starck*

H.C.Starck

MOLYBDENUM POWDER METALLURGY PRODUCTS

Number PD-7043
Issue 3-2015-09-22

MOLYBDENUM ALLOY ODS Mo-La
Powder Metallurgy Sheet 2602

Description of Product This specification covers rolled sheets of oxide-dispersion strengthened (ODS) molybdenum alloys (molybdenum and La_2O_3) at three levels of lanthana content produced from pressed and sintered powder metallurgy sheet bar.

Chemical Characteristics[1)]
(Mass fraction in % [cg/g]; ppm [µg/g])

The chemical composition of the molybdenum blended powder used for producing sheet bar shall conform to the following limits:

Mo(By Difference)	min.	98.7	%
O	max.	0.250	%
Mg	max.	0.001	%
Mn	max.	0.001	%
Ni	max.	0.005	%
Al	max -	0.002	%
Cu	max -	0.002	%
Pb	max -	0.002	%
Ti	max -	0.002	%
Ca	max -	0.003	%
Si	max -	0.005	%
Sn	max -	0.003	%
Cr	max -	0.010	%
C	max -	0.005	%
Fe	max -	0.010	%
La (Lanthanum)	**level 1:** 0.2 – 0.4%; **level 2:** 0.5 – 0.7%; **level 3:** 1.0 - 1.2%		

Structure Sheet will be supplied in a stress-relieved condition unless otherwise requested.

Mechanical Properties Tensile properties can be supplied on request when Purchase Order is placed.

Figure A.3: Chemical composition certification of Mo-La. *Source H.C. Starck*

Appendix B: Pressure Resistance Welding Schedules

A typical welding schedule for the pressure resistance welder. Some of the values change depending on the max weld current wanted or if preheat or temper stages are included. Here is an example of the weld schedule:

S T A R T O F S C H E D U L E

TRANSFORMER TURNS RATIO 062:1

TURN ON VALVE #1

SQUEEZE 40 CYCLES

TURN ON VALVE #2

WAIT FOR PRESSURE SWITCH INPUT

WAIT 40 CYCLES

SEC. CURR LIMITS: HI= 30,000 LOW= 5,000

PREHEAT 05 CY. 20%I

COOL 02 CYCLES

IMPULSE= 05 HEAT CY. 02 COOL CY.

WELD 03 IMP. 65%I

TEMPER 05 CY. 20%I

PROCESS WELD FAULTS

HOLD 05 CYCLES

TURN OFF VALVE #2

TURN OFF VALVE #1

E N D O F S C H E D U L E

Samples Mo-1 & Mo-3

S T A R T O F S C H E D U L E

TRANSFORMER TURNS RATIO 062:1

TURN ON VALVE #1

SQUEEZE 40 CYCLES

TURN ON VALVE #2

WAIT FOR PRESSURE SWITCH INPUT

WAIT 40 CYCLES

SEC. CURR LIMITS: HI= 30,000 LOW= 5,000

PREHEAT 03 CY. 20%I

COOL 02 CYCLES

IMPULSE= 05 HEAT CY. 02 COOL CY.

WELD 03 IMP. 55%I

TEMPER 03 CY. 20%I

PROCESS WELD FAULTS

HOLD 05 CYCLES

TURN OFF VALVE #2

TURN OFF VALVE #1

E N D O F S C H E D U L E

Samples Mo-2 & Mo-4

S T A R T O F S C H E D U L E

TRANSFORMER TURNS RATIO 062:1

TURN ON VALVE #1

SQUEEZE 40 CYCLES

TURN ON VALVE #2

WAIT FOR PRESSURE SWITCH INPUT

WAIT 40 CYCLES

SEC. CURR LIMITS: HI= 30,000 LOW= 5,000

PREHEAT 03 CY. 20%I

COOL 02 CYCLES

IMPULSE= 03 HEAT CY. 02 COOL CY.

WELD 03 IMP. 55%I

TEMPER 03 CY. 20%I

PROCESS WELD FAULTS

HOLD 05 CYCLES

TURN OFF VALVE #2

TURN OFF VALVE #1

E N D O F S C H E D U L E

Appendix C: Tables of Molybdenum Weld Data

Table C.1: PRW weld data for molybdenum coupons.

Sample	Time (cycles) 1 cycle = 16.67 msec	Current (A)	Voltage (V)	Energy [J] $H = I^2 \cdot R \cdot t$	Total Energy Per weld	Energy per msec
Mo-1	3	15360	2.39	1,835.9	1,835.9	36.7
Mo-2	2	4420	0.64	94.3	2,472.3	7.8
	5	7390	1.3	800.7		
	5	7110	1.28	758.5		
	7	7710	0.91	818.7		
Mo-3	2	4060	0.58	78.5	3,964.3	12.5
	5	10250	1.65	1,409.7		
	5	13040	1.22	1,326.0		
	7	12020	0.82	1,150.1		

Table C.2: PRW weld data for TZM coupons.

Sample	Time (cycles) 1 cycle = 16.67 msec	Current (A)	Voltage (V)	Energy [J] $H = I^2 \cdot R \cdot t$	Total Energy Per weld	Energy per msec
TZM-1	3	15540	2.34	1818.5	1818.5	36.4
TZM-2	2	4500	0.66	99.0	2483.2	7.8
	5	6890	1.39	798.3		
	5	6430	1.44	771.8		
	7	7120	0.98	814.2		
TZM-3	2	3960	0.6	79.2	4,048.5	12.8
	5	9350	1.8	1,402.8		
	5	12160	1.34	1,358.1		
	7	11380	0.91	1,208.4		

Table C.3: PRW weld data for Mo-La coupons.

Sample	Time (cycles) 1 cycle = 16.67 msec	Current (A)	Voltage (V)	Energy [J] $H = I^2 \cdot R \cdot t$	Total Energy Per weld	Energy per msec
Mo-La-1	3	14950	2.1	1,570.0	1,570.0	31.4
Mo-La-2	2	4620	0.53	81.6	2,476.0	7.8
	5	8470	1.14	804.8		
	5	7640	1.22	776.9		
	7	7570	0.92	812.7		
Mo-La-3	2	4340	0.55	79.6	4,026.9	12.7
	5	10990	1.54	1,410.7		
	5	12530	1.28	1,336.8		
	7	11300	0.91	1,199.9		